The fabrication and characterisation of metal oxide thin films for microelectronic and optical applications

Matthew R. Field

B.App.Sci (App.Phys)(Hons)

A thesis written for the fulfilment of the requirements

for the degree Doctor of Philosophy

School of Applied Sciences

College of Science, Engineering and Health

RMIT University

Melbourne, Australia

May, 2011

“It’s a long walk back to Eden, sweetheart, so don’t sweat the small stuff!”

-Carolyn Roberts, “Insomnia” by Stephen King

"Be faithful in small things because it is in them that your strength lies."

-Mother Teresa

Declaration

I certify that except where due acknowledgement has been made, the work is that of the author alone; the work has not been submitted previously, in whole or in part, to qualify for any other academic award; the content of the thesis is the result of work which has been carried out since the official commencement date of the approved research program; any editorial work, paid or unpaid, carried out by a third party is acknowledged; and, ethics procedures and guidelines have been followed.

....

Matthew Field

31 May 2011

Acknowledgements

First of all I would like to thank the people who helped me throughout this long endeavour in completing my PhD and writing this thesis. To my supervisor Prof. Dougal McCulloch who has not only guided me but has also taught me many valuable things in work and in life. Granted, on some occasions I might have come to your views kicking and screaming, but the experience was definitely valuable.

I would also like to thank my other supervisor, even if he fervently denies being it, Dr. James Partridge. Without your influence, I would possibly never have looked into gate dielectrics or gas sensors, and I would certainly be left sitting in the labs scratching my head over *E(J)* curves! I would also like to thank the many people that I have worked with over the years, Dr. Andre Anders, Dr Sunnie Lim and Dr. Jeff Brown for instilling a fascination of electrochromic materials and solar cells into me. It was an absolute pleasure working with you people and I hope to see you all again in Berkeley labs sometime in the near future.

I'd like to next thank the contributions of the RMMF and RMIT staff. Without Phil Francis and Peter Rummel, the RMIT microscopy suite would surely fall into chaos. I would also like to thank Ju Lin Peng, who has helped me in making TEM samples. Next I have many thanks for my co-workers, Dr Desmond Lau, Dr Nemo Biluš Abaffy, Arwen Pagon, Ali Moafi and Ben Kent for keeping me sane while in the lab, and the rest of the RMIT staff for keeping lunchtimes entertaining with the superquiz and fun chatter. Many thanks also go to my dear friends Tasha, Jarrad and Aaron, whom I would never have gotten through my undergraduate degree without! Whether you believe it or not, all of you were all very important to me during my undergrad.

Finally, to all the people out there outside of physics who have supported me through this long and frustrating time. I am REALLY sorry that I keep talking thin film coatings at you and making you zone out! Don't get me wrong, I do see your eyes glaze over from time to time, but sometimes I can't help myself and need to get it fully out of my system! So a big thankyou to my housemates Mark, Clifty, Zack, Ria and Rowan for keeping my life in check outside of work.

The last of the people for me to thank are my brother Nathan and my Mum. Without you guys, I'm not sure where I would be right now let-alone being up at 3am writing thesis chapters. But for what it's all worth, I am happy with where I am and who I am. And for that, I'm always grateful.

~Matt

Authors Publications

[1] **<u>Field MR</u>**, Partridge JG, Du Plessis J, McCulloch DG. Hafnium oxide thin films deposited from a filtered cathodic vacuum arc. *Applied Physics A: Materials Science & Processing*. 2009;**97**(3):627-33.

[2] **<u>Field MR</u>**, McCulloch DG, Lim SNH, Anders A, Keast VJ, Burgess RW. The electronic structure of tungsten oxide thin films prepared by pulsed cathodic arc deposition and plasma-assisted pulsed magnetron sputtering. *Journal of Physics: Condensed Matter*. 2008;**20**(17):175216.

[3] Partridge JG, **<u>Field MR</u>**, Peng JL, Sadek AZ, Kalantar-zadeh K, Plessis JD, et al. Nanostructured SnO_2 films prepared from evaporated Sn and their application as gas sensors. *Nanotechnology*. 2008;**19**(12):125504.

[4] Partridge JG, **<u>Field MR</u>**, Sadek AZ, Kalantar-zadeh K, Du Plessis J, Taylor MB, et al. Fabrication, Structural Characterization and Testing of a Nanostructured Tin Oxide Gas Sensor. *Sensors Journal, IEEE*. 2009;**9**(5):563-8.

[5] **<u>Field MR</u>**, Partridge JG, Mayes EH, Latham K, McCulloch DG. The relationship between microstructure and electrical breakdown in cathodic arc deposited hafnium oxide films. *Journal of Applied Physics*. Submitted for publication 2010.

Conference Presentations

[1] **The synthesis and characterisation of tungsten oxide thin films**

ACMM Conference, 11th -15th February 2008 (Perth, Australia)

M. R. Field, D. G. McCulloch, S.N.H. Lim, A. Anders, V. J. Keast, R. W. Burgess

[2] **Analysis of metal oxide thin films deposited using a filtered cathodic vacuum arc**

ACMM Conference, 11th-15th February 2008 (Perth, Australia)

J. G. Partridge, M. Field, N. Biluš Abaffy, J. Du Plessis and D. G. McCulloch

[3] **Deposition of high quality metal oxide thin films using an FCVA**

Poster at 15th AINSE Conference on Nuclear and Complementary Techniques of Analysis (NCTA), 21st – 23rd November 2007 (Melbourne, Australia)

N. Biluš Abaffy, M. Field, J. G. Partridge, J. Du Plessis and D. G. McCulloch

[4] **A study of the morphology and stoichiometry of nanostructured SnO_2 thin films**

Poster at ICONN 08, January 2008 (Melbourne, Australia).

J. G. Partridge, M. Field, J. Du Plessis, J. Yu and D. G. McCulloch

[5] **Improving aluminum doped zinc oxide films by minimizing negative ion damage**

ICCG 8 - International Conference on Coatings on Glass and Plastics

June 13 - 17, 2010, (Braunschweig, Germany)

André Anders, Jeff Brown, Sunnie Lim, Rueben Mendelsberg, Leonardo Gontijo, Kin Man Yu, and Matthew Field

[6] **Microstructural analysis of zinc oxide films doped with aluminium for solar cell research**

21st Australian Conference on Microscopy & Microanalysis

July 11 - 15, 2010, (Brisbane, Australia)

Matthew Field, André Anders, Jeff Brown and Dougal McCulloch

Abstract

Metal oxide thin films are the subject of considerable research due to their novel optical and electrical properties which make them suitable for use in many applications. These applications include gas sensors, solar cell arrays, anti dazzling rear view mirrors, smart windows, display devices, gate dielectrics, semiconductors and many more. The possibilities for new metal oxide based materials is forever growing with the introduction of novel deposition methods which allow precise control of the deposition parameters and the ability to dope in order to tailor properties. The conditions used for the deposition of these coatings has an influence on the microstructure which in turn plays an important role in determining physical properties, such as the optical transmission and electrical conductivity. In addition, for many metal oxide materials the structure-property relationship is not well understood. The aim of this thesis was two-fold. Firstly, to deposit some metal oxide thin film coatings using several physical vapour deposition techniques and characterise their microstructure and physical properties. Secondly, to make a comparison between films deposited using different techniques to determine how the properties of a film depend on the conditions under which they are formed.

To achieve these aims, tungsten oxide, zinc oxide doped with aluminium (also known as aluminium zinc oxide - AZO) and hafnium oxide coatings were deposited and the microstructure and physical properties were investigated. For tungsten oxide deposition, films were deposited using pulsed magnetron sputtering and pulsed cathodic arc. It was found that films deposited using magnetron sputtering were highly disordered. In contrast, those deposited with cathodic arc were a highly ordered and exhibited a tetragonal phase, usually only observed at high temperatures.

In the case of AZO, films were deposited using pulsed cathodic arc, pulsed magnetron sputtering and high power impulse magnetron sputtering (HIPIMS). The pulsed cathodic arc

films were found to have both good transmittance in the visible region and the best resistivity of all of the samples.

It was found that magnetron and HIPIMS produced films that exhibited non-uniform properties across their surface due to *in situ* oxygen bombardment during deposition. This undesirable effect was eliminated by incorporating a novel magnetic filter into the deposition setup which acted to improve both the crystallinity and the resistivity. This thesis also performed the first comprehensive investigation of hafnium oxide films prepared using a filtered cathodic vacuum arc. Samples deposited at high substrate biases were found to damage readily which made them electrically leaky. Samples deposited at room temperature were found to have a disordered microstructure and had a good electrical breakdown. At elevated temperatures the crystallinity of the samples increased, resulting in a microstructure containing large monoclinic crystals. However, it was also found that the electrical breakdown worsened at elevated temperatures, in agreement with other researchers who also find that hafnium oxide films with disordered microstructure have the best electrical characteristics.

Ab initio calculations of the near edge structure found in x-ray and electron loss edges were found to be a powerful way of distinguishing between the phases of tungsten oxide.

Table of Contents

DECLARATION ..... **II**
ACKNOWLEDGEMENTS ..... **III**
AUTHORS PUBLICATIONS ..... **V**
CONFERENCE PRESENTATIONS ..... **VI**
ABSTRACT ..... **VII**
TABLE OF CONTENTS ..... **IX**
LIST OF FIGURES ..... **XIII**
LIST OF TABLES ..... **XX**

CHAPTER 1 ..... **1**
INTRODUCTION **1**
1.1 BIBLIOGRAPHY 7

CHAPTER 2 ..... **10**
BACKGROUND **10**
2.1 METAL OXIDE DEPOSITION 11
2.1.1 Cathodic arc deposition *11*
2.1.2 Filtered cathodic vacuum arc (FCVA) deposition *12*
2.1.3 Pulsed cathodic arc deposition *15*
2.1.4 Magnetron sputtering *16*
2.1.5 High power impulse magnetron sputtering (HIPIMS) *17*
2.2 EXPERIMENTAL ANALYSIS METHODS 19
2.2.1 Scanning electron microscopy (SEM) *19*
2.2.2 Atomic force microscopy (AFM) *19*
2.2.2 X-ray diffraction (XRD) *19*
2.2.3 X-ray photoelectron spectroscopy (XPS) *20*
2.2.4 Optical transmission *21*
2.2.5 Resistivity and Hall measurements *22*
2.2.6 Breakdown voltage *23*
2.2.7 Transmission electron microscopy (TEM) sample preparation *23*
2.2.8 TEM and selected area electron diffraction (SAED) *25*
2.2.9 Electron energy loss spectroscopy (EELS) *26*
2.2.10 Energy loss near edge structure (ELNES) *28*

2.2.11 X-ray absorption near edge structure (XANES) *28*
2.3 THEORETICAL METHODS 31
2.3.1 Multiple scattering calculations using the FEFF code *31*
2.3.2 Band structure calculations using the WIEN2k code *34*
2.4 BIBLIOGRAPHY 35

CHAPTER 3 .... **37**
THE MICROSTRUCTURE AND ELECTRONIC STRUCTURE OF TUNGSTEN OXIDE THIN FILMS **37**
3.1 INTRODUCTION 38
3.1.2 The crystal structure of WO_3 .... *38*
3.1.3 Growth of thin films of WO_3 .... *41*
3.2 EXPERIMENTAL TECHNIQUES 44
3.2.1 Deposition using pulsed cathodic arc *44*
3.2.2 Deposition using magnetron sputtering *44*
3.2.2 Theoretical methods *45*
3.3 RESULTS AND DISCUSSIONS 46
3.3.1 X-ray photoelectron spectroscopy (XPS) *46*
3.3.2 Cross sectional transmission electron microscopy (TEM) *47*
3.3.4 Electron energy loss spectroscopy (EELS) *51*
3.3.4 Local density of states (LDOS) *52*
3.3.5 Energy-loss near edge structure (ELNES) *52*
3.4 CONCLUSIONS 58
3.5 BIBLIOGRAPHY 59

CHAPTER 4 .... **62**
MICROSTRUCTURAL ANALYSIS OF ZINC OXIDE FILMS DOPED WITH ALUMINIUM FOR SOLAR CELL RESEARCH **62**
4.1 INTRODUCTION/BACKGROUND THEORY 63
4.1.1 Doped zinc oxide in industry *63*
4.1.2 Crystal structure and doping *63*
4.1.3 AZO coatings *65*
4.1.4 Presence of negative ions in magnetron sputtering techniques *68*
4.2. EXPERIMENTAL METHODS 69
4.2.1 Pulsed cathodic arc *69*
4.2.2 Magnetron sputtering *71*
4.2.3 High power impulse magnetron sputtering (HIPIMS) *71*
4.2.4 Negative ion filter in magnetron deposition *71*

4.3. PULSED CATHODIC ARC DEPOSITED FILMS 73
4.3.1 Resistivity and Hall Effect *73*
4.3.2 Optical transmission *74*
4.3.3 Composition and microstructure *75*
4.4 MAGNETRON SPUTTERED FILMS 83
4.4.1 Resistivity and Hall Effect *83*
4.4.2 Optical transmission *84*
4.4.3 Composition and microstructure *85*
4.5 HIPIMS 91
4.5.1 Resistivity and Hall Effect *91*
4.5.2 Optical transmission *93*
4.5.3 Composition and microstructure *94*
4.6 FILTERED HIPIMS 101
4.6.1 Resistivity and Hall Effect *101*
4.6.2 Optical transmission *101*
4.6.3 Composition and microstructure *102*
4.7 COMPARISON OF TECHNIQUES 108
4.7 CONCLUSIONS 111
4.8 BIBLIOGRAPHY 113

CHAPTER 5 116
THE MICROSTRUCTURE AND ELECTRICAL PROPERTIES 116
OF HAFNIUM OXIDE PREPARED USING FILTERED CATHODIC VACUUM ARC 116
5.1 INTRODUCTION 117
5.1.1 Hafnium oxide as a dielectric *117*
5.1.2 Crystal structure of HfO_2 ..... *118*
5.1.3 Hafnium oxide films *120*
5.2 EXPERIMENTAL TECHNIQUES 121
5.3 THE EFFECT OF SUBSTRATE BIAS ON HAFNIUM OXIDE FILMS SYNTHESISED USING FCVA 122
5.3.1 X-ray photoelectron spectroscopy (XPS) *123*
5.3.2 Film topography *124*
5.3.3 Transmission electron microscopy (TEM) *127*
5.3.4 Electron energy loss spectroscopy (EELS) *130*
5.3.5 Electrical breakdown *131*

5.4 THE EFFECT OF SUBSTRATE TEMPERATURE ON HAFNIUM OXIDE FILMS SYNTHESISED USING FCVA 132

5.4.1 X-ray photoelectron spectroscopy (XPS)....... 132

5.4.2 X-ray diffraction (XRD)....... 135

5.4.3 Transmission electron microscopy (TEM)....... 137

5.4.4 X-ray absorption spectroscopy (XAS)....... 140

5.4.5 Electrical breakdown....... 142

5.6 CONCLUSIONS....... 144

5.7 BIBLIOGRAPHY....... 144

CHAPTER 6....... 148

CONCLUSIONS AND FUTURE WORK....... 148

List of Figures

Figure 2-1: Electrochromic multilayer stack. Figure is adapted from a paper by Cui et. al [7], in which multilayer stacks are constructed for electrochromic windows. 3

Figure 2-1: The FCVA deposition system at RMIT University (Melbourne, Australia) used for these experiments in this thesis. Note the double bend filter on the right. The plasma is generated near the cathode and directed through the off-plane double bend magnetic filter to the sample holder and substrate. 12

Figure 2-2: Schematic of the continuous FCVA system (not to scale). 13

Figure 2-3: The pulsed arc system located at Lawrence Berkeley National Labs (Berkeley, USA) 15

Figure 2-4: Schematic of the pulse generation systems used with the pulsed cathodic arc setup [10] 15

Figure 2-5: Schematic of a conventional magnetron sputtering system. Shown in the image are the field lines trapping the secondary electrons to form more ionisation events, increasing the deposition rate 16

Figure 2-6: Schematic of the HIPIMS deposition process. Shown in the schematic are the field lines produced by the magnetrons as well as the region of the extending plasma in which self sputtering occurs. 17

Figure 2-7: Mechanical polishing X-TEM preparation thinning process. This figure has been adapted from Desmond Lau's thesis 2009 [26]. 23

Figure 2-8: Schematic of a TEM. This figure is adapted from Desmond Lau's thesis [26]. The green ray diagram (a) represents the imaging mode of the TEM, and the red ray diagram (b) represents the TEM in diffraction mode. 25

Figure 2-9: The main features of an EELS spectra. At 260 eV the intensity of the spectra has been multiplied by 500 times to show the features of the low intensity core loss edges. The example shown here is the carbon 1s core shell ionization event [26]. 26

Figure 2-10: Core shell interaction which results in a core loss edge on an EELS spectrum. 27

Figure 2-11: The photonic processes involved in x-ray absorption spectroscopy. 29

Figure 2-12: Muffin-tin potential calculated in the self consistent field calculation [36]...........31

Figure 2-13: Multiple scattering with the wavefront scattering between multiple atoms in the material until the core-hole is refilled. 32

Figure 3-1: An individual WO_6 octahedral unit (left) where the green sphere represents the tungsten atom and the red spheres represent the oxygen atoms. When combined these octahedral units can form the monoclinic γ-WO_3 structure (right) with the different amounts of tilt on the highlighted WO_6 octahedral units [15]. 39

Figure 3-2: Tungsten 4f XPS binding energy peaks. Both samples have equivalent peaks with no shift in the binding energy. 46

Figure 3-3: Oxygen 1s XPS binding energy peaks. Both samples have equivalent peaks with no shift in the binding energy. 47

Figure 3-4: Cross-sectional TEM Images of the deposited films. (a) Magnetron sputtered sample (b) Cathodic arc sample. Insert: high resolution image of cathodic arc sample. 49

Figure 3-5: Selected area diffraction patterns of the (a) magnetron sputtered [33] and (b) cathodic arc films shown in figure 3-4. The diffraction pattern in (b) has been indexed to α-WO_3...50

Figure 3-6: Oxygen K-edge EELS spectra for the 2 experimental samples where (a) refers to the film deposited by magnetron sputtering and (b) refers to the cathodic arc deposited film. The main features have been labelled for clarity. 51

Figure 3-7: The local s and p projected density of states for oxygen calculated using FEFF8 for the α and γ phases of WO_3. 52

Figure 3-8: Calculated oxygen K-edge's for the α-WO_3 phase for various numbers of atoms surrounding the absorbing oxygen (left). A graphical representation of the clusters is also shown (right), with blue atoms and pink atoms representing oxygen and tungsten atoms respectively. 54
Figure 3-9: The calculated oxygen K-edge NES for the known phases of WO_3. The main features have been labelled and their energies have been listed in table 3-2. 55
Figure 3-10: Comparison of the oxygen K-edge of calculated using FEFF8 and WIEN2k. Note that the energy scale is relative to the Fermi energy. These are compared to γ-WO_3 obtained using XAS [24]. 56
Figure 3-11: Comparison of the oxygen K-edge for α-WO_3 calculated using FEFF8 and WIEN2k. These calculations are compared to the experimental data from the cathodic arc deposited tungeten oxide film in which diffraction analysis showed that the α-WO_3 was present. 57
Figure 4-1: Representation of the ZnO crystal structures. Figure was adapted from the ZnO review paper written by Ozgur et al [10]. The shaded grey spheres represent the Zn atoms and the black spheres represent the O atoms. 63
Figure 4-2: Deposition setup for the AZO films deposited by pulsed cathodic arc samples. AZO growth cycled between deposition and annealing during the deposition period [17]. 69
Figure 4-3: The HIPIMS setup with the inclusion of the straight magnetic filter. 71
Figure 4-4: Electrical characteristics of the AZO films deposited using the pulsed cathodic arc technique. n is the electron concentration, μ is the mobility and ρ is the resistivity. 72
Figure 4-5: Optical transmittance spectra for the pulsed cathodic arc deposited films of increasing thickness. Thicker films exhibited less optical transmission in the infrared. 73
Figure 4-6: XPS scans of the indicated pulsed cathodic arc films in the vicinity of the Zn2p, O1s and Al2p binding energies. The peak positions are typical of ZnO thin film coatings. 75
Figure 4-7: XRD of the pulsed cathodic arc samples of the samples with thickness (a) 24 nm and (b) 260 nm. 77

Figure 4-8: XAS of the 260 nm cathodic arc deposited sample in the region of the (a) aluminium K-edge (b) oxygen K-edge and (c) the zinc L-edges. Strong octahedral coordination of the films is present as given by the peak located at 1567.4 eV. Also shown in figure 4-8(b) is a FEFF9 calculation of the wurtzite ZnO phase using the lattice parameters from table 4-1. 79

Figure 4-9: TEM image of the pulsed cathodic arc sample. Indicated within the image (a) are the SiO_2 (glass) substrate and the AZO film (dark region). A high resolution image is also shown (b) where the ZnO(002) planes parallel to the surface of the substrate can be seen........81

Figure 4-10: Left hand side shows a molecular representation (zinc is blue, oxygen is red) of the ZnO crystals in the lattice looking down the different zone axes. The right hand side images show the diffraction patterns...82

Figure 4-11: The magnetron sputtering sample. AZO films were simultaneously deposited onto glass microscope slide (top) and 2 glass coverslips (bottom). Hall and resistance measurements were taken at various points on the samples. 84

Figure 4-12: Optical transmittance spectra across the surface of the magnetron sample. POS2 (red) refers to the outside of the substrate and POS4 (black) refers to the inside of the substrate 85

Figure 4-13: Zn2p, O1s and Al2p binding energy spectra for the magnetron sputtered samples, where (a) refers to the point on the inside (POS4) of the sample and (b) refers to the point at the outside (POS2) of the sample...86

Figure 4-14: Variation in aluminium concentration across the surface of the magnetron deposited AZO film. 87

Figure 4-15: XRD spectra of the magnetron sputtered sample at the outside (top) and inside (bottom) of the substrate. These locations refer to positions 2 and 4 from table 4 respectively. 88

Figure 4-16: XAS of the magnetron sputtered films in the region of the (a) aluminium K-edge (b) oxygen K-edge and (c) the zinc L-edges for the regions indicated. Also shown is the XAS of the pulsed cathodic arc sample for comparison. The peaks indicate the presence of octahedrally

coordinated Al bonding, but are largely disordered structures. Also shown in figure 4-16(b) is a FEFF9 calculation of the wurtzite ZnO phase using the lattice parameters from table 4-1........91

Figure 4-17: The deposited HIPIMS samples. The AZO films were deposited onto a glass microscope slide (bottom) and 2 glass coverslips (top). Points of interest are labelled on the image. 93

Figure 4-18: Resistivity of the HIPIMS sample across the surface as measured by 4 point probe. 94

Figure 4-19: Optical transmittance spectra across the surface of the HIPIMS samples. POS1 (red) refers to the outside of the substrate and POS3 (black) refers to the inside of the substrate 95

Figure 4-20: Zn2p, O1s and Al2p binding energy spectra for the HIPIMS samples, where (a) refers to the point on the inside (POS3) of the sample and (b) refers to the point at the outside (POS1) of the sample..97

Figure 4-21: XPS line scan of the Al2p peak across the surface of the HIPIMS sample from position A to B..98

Figure 4-22: Comparison of the HIPIMS XRD. Shown in the figure are the respective grain size and Hall measurements for each of the samples...99

Figure 4-23: XAS of the indicated HIPIMS samples in the region of the (a) aluminium K-edge, (b) oxygen K-edge and (c) zinc L-edges compared to the pulsed cathodic arc sample. Less resolved peaks in the spectra relating to the centre of the HIPIMS samples is indicative of increased disorder in the film. Also shown in figure 4-23(b) is a FEFF9 calculation of the wurtzite ZnO phase using the lattice parameters from table 4-1. 101

Figure 4-24: Optical transmittance spectra comparison between unfiltered HIPIMS (black) and straight filtered HIPIMS (red) 103

Figure 4-25: Zn2p, O1s and Al2p binding energy spectra for the HIPIMS samples with and without the straight line magnetic filter. where (a) refers to the filtered sample and (b) refers to the unfiltered one. 104

Figure 4-26: XPS line scan of the Al2p peak across the surface of the filtered HIPIMS sample from position A to B. 105

Figure 4-27: XRD comparison between the filtered HIPIMS sample and the HIPIMS sample. 106

Figure 4-28: XAS of the indicated HIPIMS samples in the region of the (a) aluminium K-edge, (b) oxygen K-edge and (c) zinc L-edges. Less resolved peaks in the spectra relating to the centre of the HIPIMS samples is indicative of increased disorder in the film. Also shown in figure 4-23(b) is a FEFF9 calculation of the wurtzite ZnO phase using the lattice parameters from table 4-1..108

Figure 4-29: Comparison of the electrical properties for the techniques used to deposit the AZO films. 110

Figure 4-30: Comparison of transmission intensity for AZO films deposited by (a) magnetron sputtering, (b) filtered HIPIMS, (c) HIPIMS and (d) cathodic arc deposition techniques........111

Figure 5-1: Schematic of HfO_2 acting as a gate dielectric in a field effect transistor device....119

Figure 5-2: The three ambient pressure phases of HfO_2 adapted from Zhao et. al [14]. 120

Figure 5-3: XPS spectra of the HfO_2 films with the indicated substrate biases in the region of the hafnium 4f binding energy peaks. 124

Figure 5-4: XPS spectra of the HfO_2 films with the indicated substrate bias's in the region of the oxygen 1s binding energy peak. 125

Figure 5-5: SEM images of the HfO_2 bias series with a (a) floating potential, (b) -100 V bias and a (c) -500 V bias. 127

Figure 5-6: AFM images of the bias series of HfO_2 films deposited using FCVA deposited with a (a) floating potential, (b) -100 V bias and a (c) -500 V bias. 128

Figure 5-7: Bright field cross-sectional TEM images of the (a) sample deposited at floating potential, (b) −100 V bias sample and the (c) −500 V bias sample. Note that the diffraction pattern in (c) contains diffraction spots from the [011] zone axis of the Si substrate. The two

main diffraction rings indicated in (a) occur at d = 2.7 Å and d = 1.6 Å and can be indexed to the (011) and a combination of the (120) and (211) reflections of monoclinic $P2_1/c$ HfO_2. 130
Figure 5-8: EELS spectra of the HfO_2 films deposited at different substrate bias's compared to that of a broadened monoclinic structure as calculated using the FEFF8 *ab initio* code.......... 132
Figure 5-9: E-J characteristics of the HfO_2 film deposited at floating potential. Films deposited with a greater substrate bias sustained film damage and the breakdown characteristics couldn't be determined. 133
Figure 5-10: XPS spectra of the Hafnium 4f peak for the HfO_x films deposited at the temperatures indicated. 134
Figure 5-11: XPS spectra in the region of the oxygen 1s binding energy peak of the hafnium oxide films deposited at the temperatures indicated 135
Figure 5-12: XRD patterns of the hafnium oxide films deposited with the indicated deposition temperatures. The labelled peaks have been indexed either to the monoclinic or tetragonal phases of HfO_2 as shown in table 5-4. 137
Figure 5-13: X-TEM images of the HfO_2 films prepared with substrate temperatures of (a) room temperature, (b) 400 ºC and (c) 800 ºC. The HfO_2 film is the dark region running down the centre of each image, the silicon substrate is on the right hand side and the epoxy bonding agent is on the left hand side... 139
Figure 5-14: SAED patterns of the film areas shown in figure 5-13, deposited with substrate temperatures of (a) room temperature, (b) 400 ºC and (c) 800 ºC. The patterns have been indexed to the monoclinic phase of HfO_2. 140
Figure 5-15: XAS in the vicinity of the oxygen K-edge of the HfO_2 films deposited with the indicated temperatures compared to a monoclinic powder standard. 142
Figure 5-16: Comparison of the oxygen K-edge for the FEFF9 calculations of 3 phases of HfO_2 compared to the 800ºC HfO_2 sample and monoclinic powder standard. The spectra 'FEFF9 – Mix' refers to a 3:2 linear combination of the monoclinic phase and the tetragonal phase. 143
Figure 5-17: E-J characteristics measured from HfO_2 films deposited using a FCVA with the indicated substrate temperatures. 144

List of Tables

Table 3-1: Details of the crystallography of the phases of WO_3 and the method of formation of the bulk crystal. Those marked with 'Powder' in the formation method were a commercially purchased polycrystalline powder of unspecified phase. 40

Table 3-2: The position (eV) of the main features in the experimental and calculated oxygen K-edges. Note that the experimental and calculated values have been shifted so that the first NES peak (A) aligns with previous XAS measurements of γ-WO_3 [24]. 58

Table 4-1: Crystallographic details of the main ZnO crystal structures. 63

Table 4-2: Pulsed arc electrical results. Electrical results were determined from the Hall Effect measurements. 72

Table 4-3: Details for the atomic percentages of the pulsed arc deposited AZO films. 76

Table 4-4: XRD of pulsed arc samples showing the film thickness, Bragg scattering angle, FWHM of the XRD peak and the calculated crystal grain size. 77

Table 4-5: Electrical measurements performed on the samples deposited by magnetron sputtering. Highlighted cells refer to locations on the samples that are analysed later with other techniques. NM refers to points where no measurement was possible. 84

Table 4-6: Details of the XPS experiment on the magnetron sputtered samples 86

Table 4-7: Peak position and grain size analysis of the AZO samples deposited using magnetron sputtering and HIPIMS. 89

Table 4-8: Electrical characteristics for the HIPIMS sample. The positions refer to the points shown in figure 4-17. Highlighted cells refer to locations on the samples that are analysed later with other techniques 93

Table 4-9: Details of the XPS experiment on the static HIPIMS sample. POS3 refers to the inside of the sample, POS1 refers to the outside of the sample 97

Table 4-10: Peak position and grain size analysis of the AZO samples deposited using magnetron sputtering and HIPIMS. 100

Table 4-11: Electrical characteristics for the HIPIMS samples deposited both with and without the inclusion of the straight magnetic filter. 102

Table 4-12: Details of the XPS experiment on the static HIPIMS sample. POS3 refers to the inside of the sample, POS1 refers to the outside of the sample 104

Table 4-13: Peak position and grain size analysis of the AZO samples deposited using magnetron sputtering and HIPIMS. 106

Table 4-14: Comparison of electrical properties for each of the listed deposition methods. Films of similar thickness were chosen so that a fair comparison could be made. 110

Table 4-15: Comparison of microstructural properties of the deposited AZO films. 112

Table 5-1: Lattice parameters of the ambient pressure phases calculated using GGA by Zhao et. al [14] as well as their formation temperature. Also shown is the high pressure phase calculated by Lowther et al. 120

Table 5-2: Atomic percentage of the HfO_2 films with increasing substrate bias during deposition determined using XPS. Each of the deposited films was found to be close to stoichiometric HfO_2. 125

Table 5-3: Calculated atomic percentages within the HfO_2 films rounded to the nearest percent. 135

Table 5-4: Details of the indexing of the XRD spectra shown in figure 2. All peaks could be indexed either to the monoclinic or tetragonal phases of HfO_2 using previously published lattice parameters [14]. Note that multiple phases are shown for peaks ‘4’ and ‘7’ due to ambiguity in the peak positions between the two phases... 138

Table 5-5: The microstructures of the films determined using XRD and the electric field at which the leakage current density exceeded 1 μAcm^{-2}.. 144

Chapter 1

Introduction

Nanotechnology is one of the fastest growing areas in materials science, with billions of dollars spent in the western economies to develop national nanotechnology initiatives and further research into enhanced products that improve our lifestyles. Within the realm of nanotechnology, the metal oxide group of materials plays an important role because of their diverse range of properties and their outstanding performance for many applications. These applications include capacitive devices, gas and bio sensor arrays, modulated refractive index layers in optical coatings, solar cells and energy saving applications. The diversity of metal oxide properties (and applications) arises from their complex atomic and electronic structures. The reason for this complexity is the variety of oxidation states, coordination number, symmetry, density, and stoichiometry giving rise to properties ranging from electrically insulating to conducting and from optically opaque to transparent.

The focus of this thesis was the investigation of three different types of metal oxides, all of which are technologically important. These are tungsten oxide, aluminium doped zinc oxide (also known as aluminium zinc oxide or AZO) and hafnium oxide. Tungsten oxide and AZO are members of a group of metal oxides known as transparent conducting oxides (TCO's). Normally conductive materials (such as metals) are opaque due to their large carrier concentration, and insulating materials (such as glasses) are transparent. TCO's are a unique group of materials that combine the conductivity usually inherent in metals with the transparency of glasses.

Tungsten oxide is a d^0-transition metal oxide which exhibits many interesting optical, electrical structural and defect properties. Interest in this TCO material begun back in 1837 when Wohler observed an intense metal lustre in $LiWO_3$ [1, 2]. Thinking that formation of metal alloys caused this lustre, he named this set of materials 'tungsten bronzes'. Considerable experimental and theoretical work was performed by Mott [3], Sienko [4] and many others from the 1950's on tungsten bronzes because they are unusually conductive for oxidised materials [3-6]. Since then in the mid 1960's, thin film MoO_3 and WO_3 both have been studied to investigate photochromism, an effect which causes thin films show reversible bleaching and discolouration. This led to the discovery of the electrochromic (EC) effect in highly disordered films.

Soon 'thin film sandwiches' were being constructed, whereby a multilayer film stack is synthesised and has been shown to exhibit a reversible change in colouration. Figure 2-1 shows an example of WO_3 used in a multilayer stack for electrochromic windows [7]. The EC effect was originally demonstrated using semi solid state devices were used with a liquid electrolyte, but a much more practical solution is to use a multilayer stack film to construct a full solid state device. An example of this structure is M-SiO-WO_3-TCO, which has been modified to include other transition metal oxides, and has since been studied extensively. Although studied for some time, there is still considerable interest in investigating the structure-property relationships in tungsten oxides.

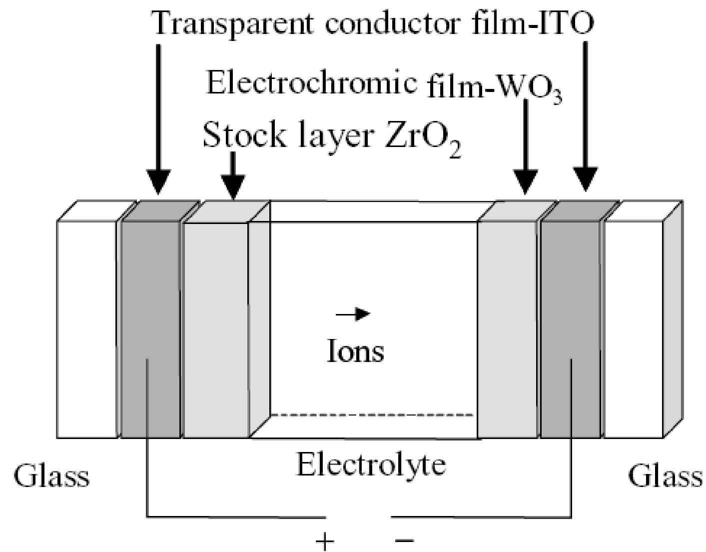

Figure 2-1: Electrochromic multilayer stack. Figure is adapted from a paper by Cui et. al [7], in which multilayer stacks are constructed for electrochromic windows.

Another TCO of importance is doped zinc oxide. In particular aluminium doped zinc oxide (or AZO for short) is currently of interest as a competitor for indium doped tin oxide (ITO). Currently ITO is in widespread use for opto-electronic applications such as flat panel displays and thin-film solar cells because it has high transmittance and low resistivity. However, because of the limited reserves of indium, the manufacturing costs have recently risen by a factor of ten [8] and the search for an efficient ITO substitute has attracted attention from many researchers [9-16]. AZO films are a promising choice as a replacement to ITO because of the abundance of the constituents. However, researchers have yet to find a cost effective way of readily synthesising AZO films with optical and electrical properties comparable to ITO.

Hafnium oxide is a promising candidate as a high-k gate oxide material in microelectronic components. It has a large band-gap (5-6 eV) and readily forms device grade interfaces with silicon, making it a potential replacement for SiO_2. High-k dielectrics have been thought to be a suitable replacement for SiO_2 because they combine a high gate capacitance and low leakage which can be maintained for thicker films. This has not only attracted the attention of many

research groups [17-21], but is also being studied by the Intel Corporation for use as a complementary metal oxide semiconductor in transistors [22, 23]. It remains a challenge to indentify the most effective method of synthesising HfO_2 films with high dielectric constant and low leakage current.

It is clear that tungsten oxide, AZO and hafnium oxide are technologically important materials. However, for these materials to fulfil their potential, precise control over their synthesis is needed. Since most applications require thin films, methods for synthesis are required which allow the deposition of high quality films with precise thicknesses. In addition, depending on the deposition method used, different microstructure can result leading to vastly different electrical and optical properties. It has been shown, for example, that depending on deposition method ZnO films can be grown to be spherically shaped, lenticular or columnar [13, 24, 25]. Since electrical and optical properties of materials are dependant on the microstructure, in order to fully optimise a material for use in industry, their structure must be understood on an atomic level. Therefore, methods which are capable of studying structure at high spatial resolution are critical. For this reason, this thesis employs electron microscopy, diffraction and spectroscopy techniques which are capable of accurately investigating the atomic level, structure and bonding.

This thesis synthesises thin films with a process known as physical vapour deposition (PVD) in which a coating is deposited from a plasma of its constituent elements. Several different PVD methods are available which differ in the way they produce the plasma. For example, sputtering methods produce a plasma by bombarding a target with inert gas ions (usually Ar), whereas in a filtered cathodic vacuum arc (FCVA) the plasma is generated by applying a high current to a conducting cathode. These plasmas differ considerably in their nature and this can lead to considerable differences in the microstructure of the deposited films. For example, in conventional sputtering, films are formed mainly by low energy neutrals while in the cathodic arc, deposition occurs from energetic ions. It is therefore important that the relationship

between synthesis method and the resulting microstructure and properties of a particular type of film be investigated. By properly understanding the strengths and weaknesses of the deposition techniques, it is possible to extend this knowledge to other fields and enhance the properties of other thin films.

The specific aims of this thesis are:

- to study tungsten oxide thin films deposited by two very different deposition techniques – pulsed magnetron sputtering and pulsed cathodic arc so that the relationship between deposition conditions and resulting microstructure can be determined.

- to investigate AZO coatings prepared using pulsed cathodic arc, pulsed magnetron sputtering and high power impulse magnetron sputtering (HIPIMS) in order to determine the optimum conditions under which films can be prepared with high optical transparency and good electrical performance.

- to undertake a thorough investigation of hafnium oxide coatings prepared using a filtered cathodic vacuum arc. An important aspect of the study was to find a link between the type of structure of the deposited film and its breakdown voltage so that the electrical properties can be optimised for future use as a gate dielectric in microprocessor applications.

This thesis is divided into several chapters. Chapter 2 outlines the background theory, describing both the deposition methods used to synthesise the thin film coatings and the techniques used to study them. Chapters 3, 4 and 5 present the main results of the investigation of the three metal oxide coatings outlined in the aims above. Chapter 6 provides a summary on the work presented in this thesis as well as some future work to be explored.

The major outcomes of this thesis include:

- Tungsten oxide films deposited using pulsed cathodic arc and pulsed magnetron sputtering exhibit very different microstructures. Films deposited using pulsed cathodic arc were ordered and exhibited a phase which is usually only observed at high temperatures, while pulsed magnetron sputtering produced films that were highly disordered.

- A comparison of AZO films prepared using several physical vapour deposition techniques found that films deposited using pulsed cathodic arc displayed the best electrical properties.

- Non-uniformity in magnetron sputtered AZO coatings, which had previously been thought to be due to *in situ* oxygen ion damage during film growth, was confirmed by using a novel magnetic filter to remove these ions during deposition. The magnetic filter was also found to increase the deposition rate in HIPIMS, potentially overcoming the major limitation of this technique which is a low deposition rate.

- Hafnium oxide films deposited at room temperature using an FCVA display a disordered microstructure and exhibit good breakdown characteristics. Those deposited at elevated temperatures have improved crystallinity, however, the breakdown characteristics are compromised, supporting the proposition that disordered hafnium oxide films exhibit the best electrical breakdown properties.

- Throughout this thesis, *ab initio* calculations were found to be extremely useful for simulating near-edge structure of metal oxides and help identify changes in local bonding and microstructure.

1.1 Bibliography

1. Raubenheimer, O., *Friedrich wöhler and the centenary of synthesis.* Journal of the American Pharmaceutical Association, 1928. **17**(10): p. 973-980.
2. Deb, S.K., *Opportunities and challenges in science and technology of WO_3 for electrochromic and related applications.* Solar Energy Materials and Solar Cells, 2008. **92**(2): p. 245-258.
3. Mott, N.F., *The degenerate electron gas in tungsten bronzes and in highly doped silicon.* Philosophical Magazine, 1977. **35**(1): p. 111 - 128.
4. Sienko, M.J. and S.M. Morehouse, *Electrical and Magnetic Properties of Potassium Tungsten Bronze and Rubidium Tungsten Bronze.* Inorganic Chemistry, 1963. **2**(3): p. 485-489.
5. Straumanis, M.E. and S.S. Hsu, *The Lithium Tungsten Bronzes.* Journal of the American Chemical Society, 1950. **72**(9): p. 4027-4030.
6. Weller, P.F., B.E. Taylor, and R.L. Mohler, *Crystal preparation of doped sodium tungsten bronze.* Materials Research Bulletin, 1970. **5**(6): p. 465-476.
7. Cui, H.N., M.F. Costa, V. Teixeira, I. Porqueras, and E. Bertran, *Electrochromic coatings for smart windows.* Surface Science Proceedings of the 7th International Conference on Nanometer-Scale Science and Technology and the 21st European Conference on Surface Science, 2003. **532-535**: p. 1127-1131.
8. Minami, T., *Present status of transparent conducting oxide thin-film development for Indium-Tin-Oxide (ITO) substitutes.* Thin Solid Films, 2008. **516**(17): p. 5822-5828.
9. Anders, A., S.H.N. Lim, K.M. Yu, J. Andersson, J. Rosén, M. McFarland, and J. Brown, *High quality ZnO:Al transparent conducting oxide films synthesized by pulsed filtered cathodic arc deposition.* Thin Solid Films, 2010. **518**(12): p. 3313-3319.
10. Dasgupta, N.P., S. Neubert, W. Lee, O. Trejo, J.-R. Lee, and F.B. Prinz, *Atomic Layer Deposition of Al-doped ZnO Films: Effect of Grain Orientation on Conductivity.* Chemistry of Materials, 2010. **22**(16): p. 4769-4775.
11. Deng, Z., C. Huang, J. Huang, M. Wang, H. He, H. Wang, and Y. Cao, *Effects of Al content on the properties of ZnO:Al films prepared by Al₂O₃ and ZnO co-sputtering.* Journal of Materials Science: Materials in Electronics, 2010. **21**(10): p. 1030-1035.
12. Fang, G. and et al., *Magnetron sputtered AZO thin films on commercial ITO glass for application of a very low resistance transparent electrode.* Journal of Physics D: Applied Physics, 2002. **35**(23): p. 3096.
13. Lim, D.G., D.H. Kim, J.K. Kim, O. Kwon, K.J. Yang, K.I. Park, B.S. Kim, S.W. Lee, M.W. Park, and D.J. Kwak, *Improved electrical properties of ZnO:Al transparent conducting oxide films using a substrate bias.* Superlattices and Microstructures, 2006. **39**(1-4): p. 107-114.
14. Saarenpää, H., T. Niemi, A. Tukiainen, H. Lemmetyinen, and N. Tkachenko, *Aluminum doped zinc oxide films grown by atomic layer deposition for organic photovoltaic devices.* Solar Energy Materials and Solar Cells, 2010. **94**(8): p. 1379-1383.
15. Tsujino, J., N. Homma, T. Sugawara, I. Shimono, and Y. Abe, *Preparation of Al-doped ZnO thin films by RF thermal plasma evaporation.* Thin Solid Films, 2002. **407**(1-2): p. 86-91.
16. Xu, J., H. Wang, L. Yang, M. Jiang, S. Wei, and T. Zhang, *Low temperature growth of highly crystallized ZnO:Al films by ultrasonic spray pyrolysis from acetylacetone salt.* Materials Science and Engineering: B, 2010. **167**(3): p. 182-186.
17. Afanas'ev, V.V., A. Stesmans, and W. Tsai, *Determination of interface energy band diagram between (100)Si and mixed Al--Hf oxides using internal electron photoemission.* Applied Physics Letters, 2003. **82**(2): p. 245-247.

18. Nguyen, N.V., A.V. Davydov, D. Chandler-Horowitz, and M.M. Frank, *Sub-bandgap defect states in polycrystalline hafnium oxide and their suppression by admixture of silicon.* Applied Physics Letters, 2005. **87**(19): p. 192903-3.
19. Preisler, E.J., S. Guha, M. Copel, N.A. Bojarczuk, M.C. Reuter, and E. Gusev, *Interfacial oxide formation from intrinsic oxygen in W--HfO_2 gated silicon field-effect transistors.* Applied Physics Letters, 2004. **85**(25): p. 6230-6232.
20. Yan, Z.J., R. Xu, Y.Y. Wang, S. Chen, Y.L. Fan, and Z.M. Jiang, *Thin HfO_2 films grown on Si(100) by atomic oxygen assisted molecular beam epitaxy.* Applied Physics Letters, 2004. **85**(1): p. 85-87.
21. Yu, H.Y., M.F. Li, B.J. Cho, C.C. Yeo, M.S. Joo, D.L. Kwong, J.S. Pan, C.H. Ang, J.Z. Zheng, and S. Ramanathan, *Energy gap and band alignment for $(HfO_2)_x(Al_2O_3)_{1-x}$ on (100) Si.* Applied Physics Letters, 2002. **81**(2): p. 376-378.
22. Chau, R., J. Brask, S. Datta, G. Dewey, M. Doczy, B. Doyle, J. Kavalieros, B. Jin, M. Metz, A. Majumdar, and M. Radosavljevic, *Application of high-κ gate dielectrics and metal gate electrodes to enable silicon and non-silicon logic nanotechnology.* Microelectronic Engineering, 2005. **80**: p. 1-6.
23. Chau, R., S. Datta, M. Doczy, J. Kavalieros, and M. Metz, *Gate Dielectric Scaling for High-Performance CMOS: from SiO_2 to High-κ*, in *Extended Abstracts of International Workshop on Gate Insulator (IWGI)*. November 2003, pp. 124-126: Tokyo, Japan.
24. Lu, J.G., Z.Z. Ye, Y.J. Zeng, L.P. Zhu, L. Wang, J. Yuan, B.H. Zhao, and Q.L. Liang, *Structural, optical, and electrical properties of (Zn,Al)O films over a wide range of compositions.* Journal of Applied Physics, 2006. **100**(7): p. 073714-11.
25. Schuler, T. and M.A. Aegerter, *Optical, electrical and structural properties of sol gel ZnO:Al coatings.* Thin Solid Films, 1999. **351**(1-2): p. 125-131.

Chapter 2

Background

This chapter describes the techniques used to deposit the metal oxide films and explains why they were selected. Following this, the experimental methods used to characterise the thin films are presented. Finally, the ab initio codes which was used to predict the fine structure on absorption edges measured using electron energy loss and x-ray absorption spectroscopy are described. This calculated fine structure was found to be particularly useful for helping to identify phases in the several of the metal oxides of interest in this thesis.

2.1 Metal oxide deposition

For the work outlined in this thesis, metal oxide thin films were deposited using a variety of techniques. In the following sections, details of these deposition techniques are presented.

2.1.1 Cathodic arc deposition

In this deposition technique, a conducting cathode is kept under vacuum and is connected to a high current (20-200 A), low voltage power (~20 V) supply. After being initiated by striking the cathode with an earthed trigger, a plasma stream is formed. This plasma stream expands and is directed away from the cathode towards the substrate material to form a thin film. The mechanisms for this plasma deposition process are still hotly debated [1-4], but one theory suggests that the high current forms localised intense electric fields and explosive field emission of electrons [5]. This field emission causes local heating in the cathode, and in turn thermally emitted electrons are also released. The constant emission of electrons in this way forms a positive feedback loop, and thermal runaway occurs forming microscopic non-stationary regions known as 'cathode spots'. These microscopic cathode spots have extremely high current density, power density and plasma density. Over time the plasma spots increase in size, which in turn reduces the current density and the voltage at the spot will drop. The rapid heating of the material in this localised region also reduces the conductivity, making it less favourable for the spot to remain stationary. This extinguishes the plasma spot at its current location and a new spot will form with the same current density in a new location, giving rise to a near continuous plasma emission. The plasma expanding from the cathode contains charged ions (of kinetic energy approximately 18-150 eV), and due to the explosive nature of the process the plasma stream also contains macroparticles and neutral atoms. Macroparticles are undesirable since they can degrade film quality.

2.1.2 Filtered cathodic vacuum arc (FCVA) deposition

For the removal of macroparticles, the FCVA was developed by Akensov et al in 1978 [6]. In this design, a 90º toroidal magnetic filter was used to direct the plasma stream from the cathode to the substrate. When using a magnetic field in this manner, the plasma stream follows the filter around the 90º bend because it is highly charged. Any macroparticles and neutral atoms are unaffected by the field, thus will continue in their original trajectory and are filtered out. Further improvements to the magnetic filter have since been made. The FCVA located at RMIT University (used in this study, shown in figure 2-1) uses an off-plane double bend magnetic filter, first developed by Shi et al [1], to more effectively remove macroparticles.

Figure 2-2 shows a schematic of the FCVA at RMIT University. The cathode is water cooled to prevent heating damage to nearby components, and is rotated during deposition to further randomise the location at which the cathode spots appear so that even wear of the cathode surface is achieved. The plasma produced at the cathode is directed through an off plane double bend magnetic filter towards the sample holder holding the substrate. The sample holder is connected to a DC power supply so that a controllable bias can be supplied to the substrate to increase the deposition energy of the plasma. The deposition system was pumped by a turbo-molecular pump backed by a scroll pump.

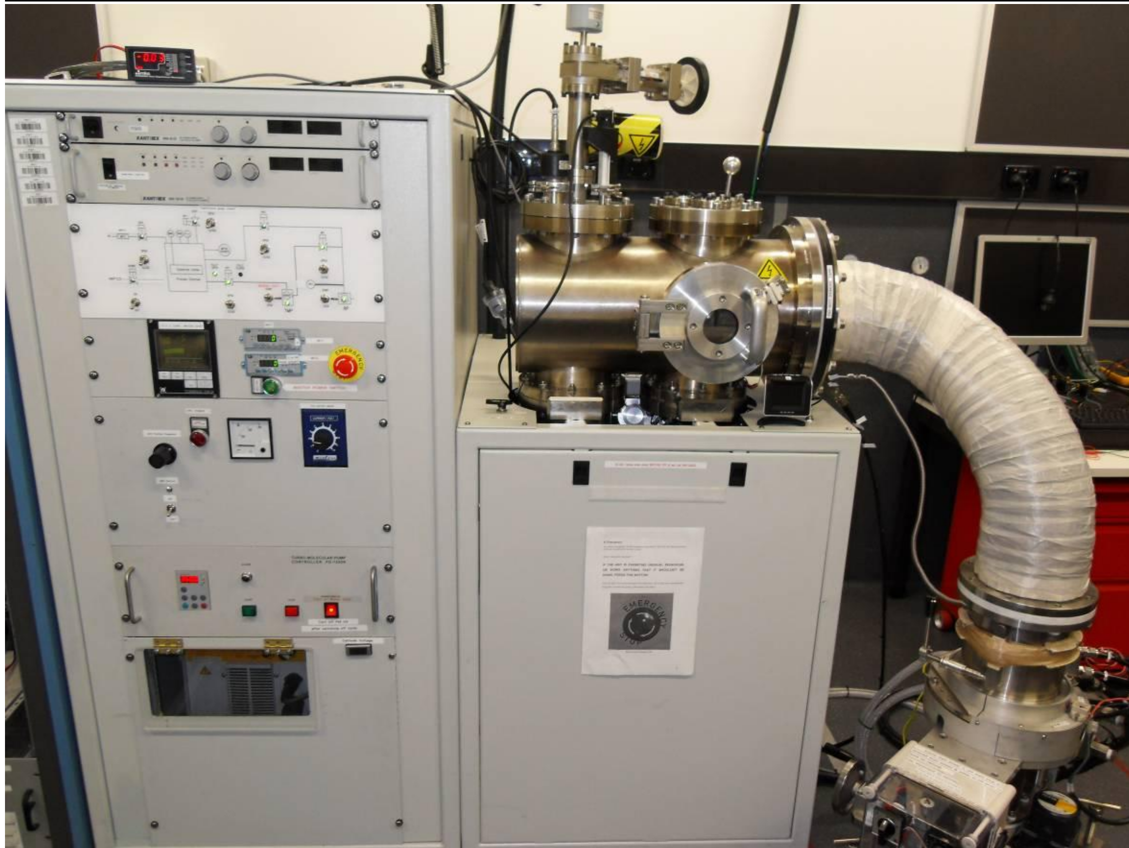

Figure 2-1: The FCVA deposition system at RMIT University (Melbourne, Australia) used for these experiments in this thesis. Note the double bend filter on the right. The plasma is generated near the cathode and directed through the off-plane double bend magnetic filter to the sample holder and substrate.

For the energetic deposition of metal oxides in this work, the films were grown in the presence of background gases. During the plasma production process, a mixture of argon and oxygen gas was bled into the chamber. The oxygen gas is present to react with the metal film as it grows, and the argon gas is present to encourage plasma stability. Due to the nature of cathodic arc deposition, a conductive cathode is required, which can be "poisoned" when oxygen is present due to the build up of an insulating layer on the surface of the cathode. To help combat this, the argon and oxygen gases were bled into the chamber at two different locations. The oxygen gas was bled into the deposition chamber near to the substrate and the argon was bled into the chamber near to the cathode so that it provides stability to the plasma, as well as providing

upwards pressure in the bottom half of the chamber, reducing the amount of oxygen gas reacting with the cathode.

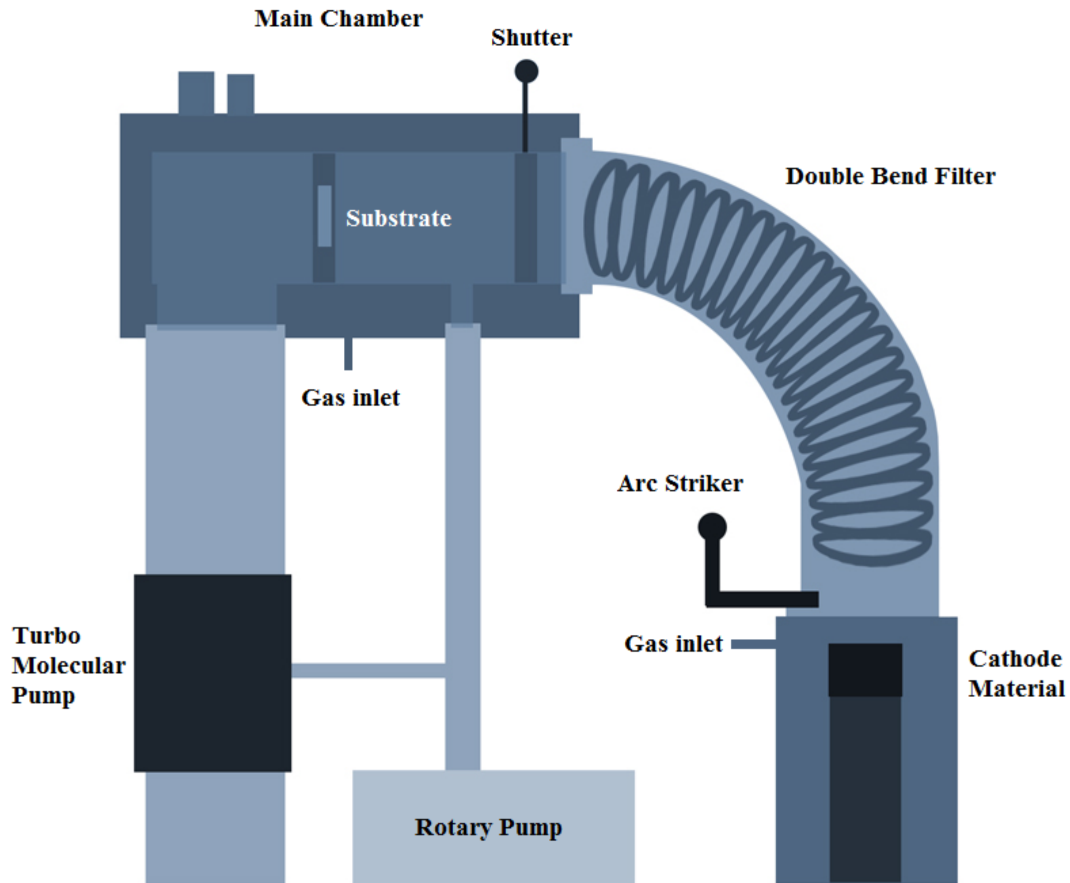

Figure 2-2: Schematic of the continuous FCVA system (not to scale).

If the substrate is electrically grounded during film deposition, then the ions within the plasma will deposit onto the substrate with their original ion energy. It is possible to modify the energy of the depositing ions by placing an electrical bias onto the substrate to either accelerate the ions (with a negative bias) or decelerate them (positive bias) [7, 8]. The equation that describes the ion energy during deposition is:

$$E_i = e(V_p - V_b) + E_o ,$$

Equation 2-1: Energy of ions in a plasma during film deposition

where E_i is the energy of the ions reaching the substrate, q is the charge state of the ions, V_p is the plasma potential, V_b is the substrate potential and E_o is the original energy of the plasma. It has been shown [8, 9] that by modifying the substrate bias (and hence the ion energy), it is possible to change not only the microstructure of the film, but its physical properties such as hardness, density and optical properties. Also possible in FCVA deposition is the growth of films with increased substrate temperatures. This was performed using a specimen stage and controller. Generally, increasing the substrate temperature increases the surface mobility of the deposited atoms, giving them enough energy to find lower energy states and therefore more ordered films result.

2.1.3 Pulsed cathodic arc deposition

In addition to conventional cathodic arc deposition a pulsed cathodic arc was used to deposit films (see figure 2-3). In a pulsed cathodic arc system much higher deposition rates are achieved by controlling the current to the cathode with a pulse generator. Doing so allows for a much higher power density and the system will cool in between pulses. As shown schematically in figure 2-4 the substrate, macroparticle filter and plasma source are connected to a master pulse generator. This controls the entire system so that the high voltage pulses within each of the components will only be applied during the short deposition periods.

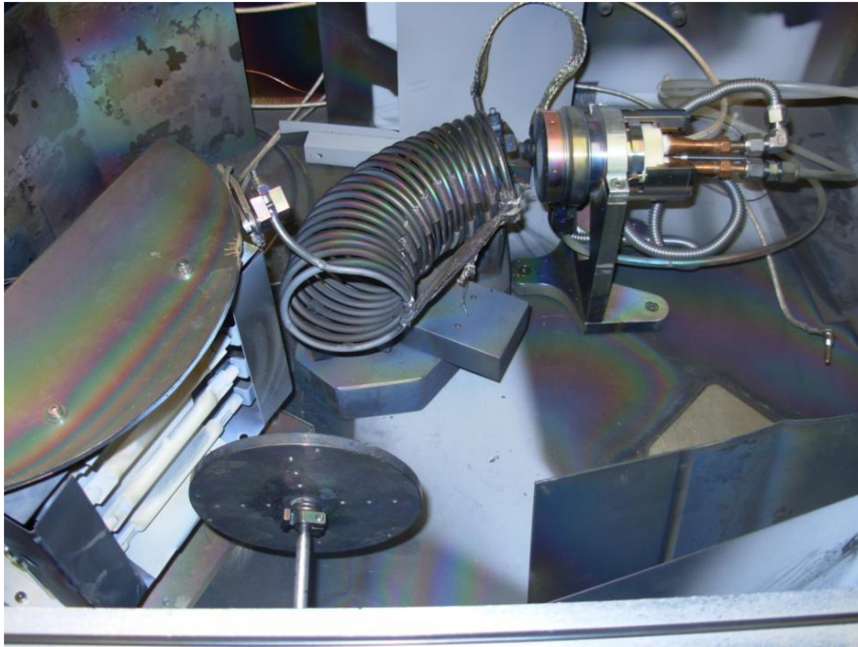

Figure 2-3: The pulsed arc system located at Lawrence Berkeley National Labs (Berkeley, USA)

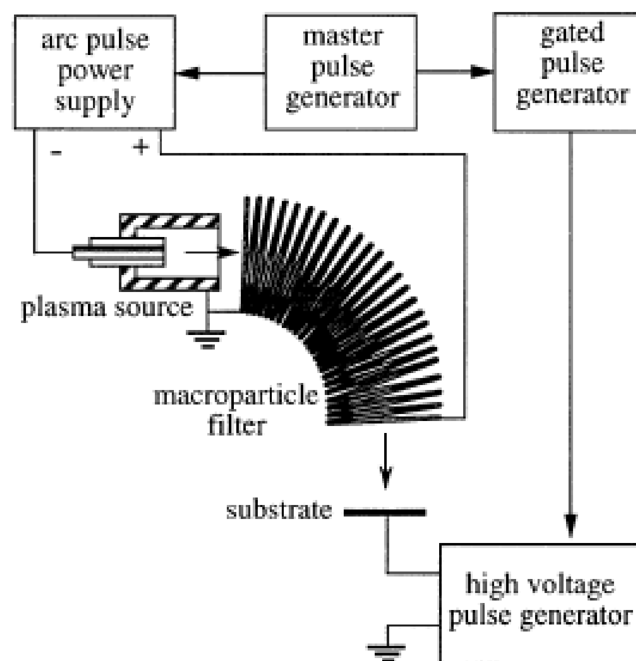

Figure 2-4: Schematic of the pulse generation systems used with the pulsed cathodic arc setup [10].

For the pulsed cathodic arc experiments, a 90º single bend macroparticle filter was used to remove the macroparticles and low energy neutrals, as well as direct the plasma towards the

substrate. The substrate was mounted onto the sample holder which rotates during the deposition to promote even coverage.

2.1.4 Magnetron sputtering

Magnetron sputtering is a highly regarded thin film deposition technique whose origins go back to the introduction of the planar magnetron by J. S Chapin in 1974 [11, 12]. It is used by many research groups for the development of advanced coatings and is also in widespread use in industry for large scale coating of high quality films. In a conventional sputtering process, inert gas ions (such as argon) are accelerated towards a negatively biased target material. This target contains at least one of the constituents to be deposited onto the substrate. When the target is sputtered, the material to be deposited and secondarily electrons are ejected and form a thin film on the substrate placed nearby within the vacuum. It is also possible to deposit compounds such as metal oxides by introducing another gas into the chamber. This process is often referred to as reactive sputtering. A schematic of the magnetron sputtering process is shown in figure 2-5.

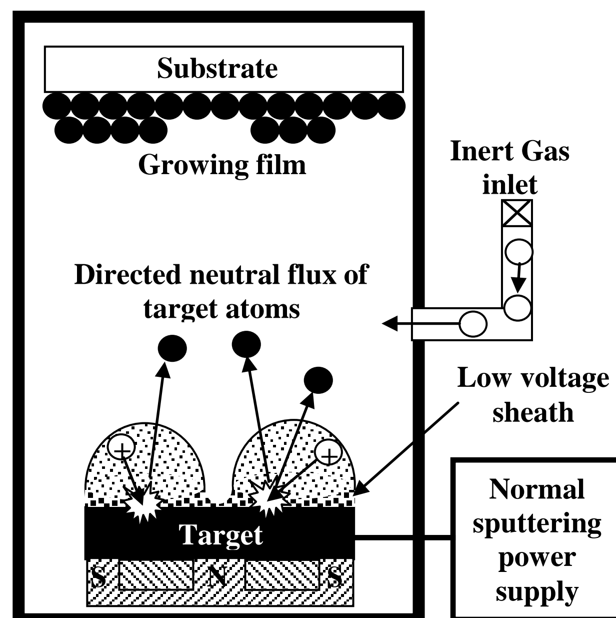

Figure 2-5: Schematic of a conventional magnetron sputtering system. Shown in the image are the field lines trapping the secondary electrons to form more ionisation events, increasing the deposition rate.

In magnetron sputtering the target is mounted upon a series of negatively biased magnetrons which are used to attract the positive ions [11]. Inclusion of the ring magnets traps the secondary electrons within the magnetic field allowing for more ionisation events to occur, further increasing the deposition rate of the target material.

2.1.5 High power impulse magnetron sputtering (HIPIMS)

HIPIMS is a technique based on magnetron sputtering that was first utilised by Kouznetsov in 1999 [13]. Unlike magnetron sputtering, HIPIMS, as the name suggests, uses extremely high power density pulses, achieving a greater ionisation of the sputtered material. Very high plasma densities exceeding 10^{18} m^{-3} [13-15] have been reported for some materials such as titanium and copper. The HIPIMS plasma appears to be less confined by the magnetic field of the magnetron and is believed to be sustained by intense secondary electron emission from the target surface. The concentration of target ions is high enough to allow "self sputtering" (figure 2-6).

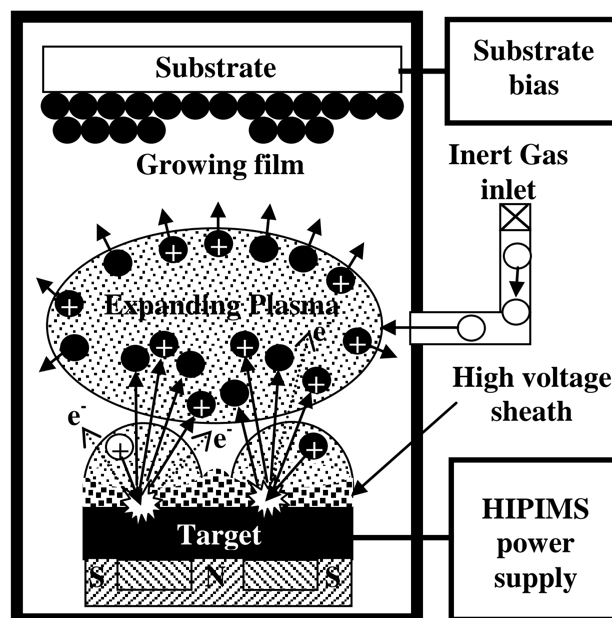

Figure 2-6: Schematic of the HIPIMS deposition process. Shown in the schematic are the field lines produced by the magnetrons as well as the region of the extending plasma in which self sputtering occurs.

A universal problem in HIPIMS, for both non reactive and reactive processes, is a low deposition rate. A recent report has shown that ions can be more efficiently directed towards the substrate in the so called "unbalanced" magnetron which uses a magnetic field with open lines of force that connect the substrate to the target [16, 17]

2.2 Experimental Analysis Methods

2.2.1 Scanning electron microscopy (SEM)

SEM images were obtained using a FEI Nova NanoSEM field emission SEM in high vacuum mode with a spot size of 3.5 nm and an accelerating voltage of 20kV. Carbon strapping was run from the surface of the samples to the stub (earth) to minimise any possible charging effects on the sample surface during image acquisition.

2.2.2 Atomic force microscopy (AFM)

AFM is a technique which can be used to provide very high resolution surface profiles of a sample. It can be used to determine the RMS roughness of a surface and give topographic information. AFM was performed using a Veeco Dimension 3100 AFM operated in tapping mode over an area of 500μm x 500μm to determine the RMS roughness and defect density of the samples.

2.2.2 X-ray diffraction (XRD)

XRD is a technique which takes advantage of Bragg diffraction, in which x-rays of a known wavelength are used to probe a sample. XRD studies were carried out on a Bruker D8 ADVANCE wide-angle diffractometer, using a graphite-monochromated Cu Kα source of wavelength λ= 1.5406 Å. Data was collected with a scan range of 2θ= 10–90°, a step size of 0.02° and a count rate of 2s per step.

XRD spectra can be used to estimate of the average grain size of crystallites within a sample. The Scherrer formula is given by:

$$D = \frac{K\lambda}{\beta \cos \theta_B}$$

Equation 2-2: Scherrer equation to determine average grain size

where D is the grain size, K is the shape factor, λ is the wavelength of the x-rays being used, β is the FWHM of the peaks (radians) and θ_B is the Bragg angle (radians). The shaping factor is usually approximated to 0.9 for particles of unknown geometry [18-20]. Sherrer's equation assumes that the stress-related and instrument-related broadening is negligible in comparison to particle size effects.

2.2.3 X-ray photoelectron spectroscopy (XPS)

In XPS, the sample is probed using an x-ray beam and the resulting photo-emitted electrons usually from the top 1-10 nm of the sample are analysed. The energies measured from the electrons correspond to the energy levels between the electronic orbitals of the atoms, and are thus indicative of not only the elements present within the sample, but also the bonding state of those elements. Using this technique depth profiles can be performed by sputtering the sample using an ion beam to study the properties of the sample as a function of depth. It is also possible to study any variations in chemistry across the surface of the sample.

The XPS work in this thesis was performed using two different instruments. The first part of this work (chapter 3) was performed using a VG Microlab 310F with a dual Al/Mg anode unmonochromated x-ray source operated at a power of 300 W and 15 kV excitation voltage. The sample was tilted such that the electron analyzer normal to the sample surface collected the escaping electrons. The analyzed area was determined by the electrostatic lens and slits of the analyzer and in this case was approximately a rectangular area of 5 x 1 mm^2. The second part of

this work (chapters 4 and 5) were performed using a Thermo Scientific K-Alpha Spectrometer with an Al anode x-ray source. The spot size for measurements was ~400μm and a flood gun was utilised to remove the possibility of sample charging during analysis. Depth profiles were performed to remove surface contaminants with a 500eV Ar ion beam with a low sputter current so as to not damage the sample during analysis.

In addition to collecting spectra in the region of the oxygen 1s, carbon 1s and metal bonding peaks, broad survey spectra were also collected to check for the possibility of impurities within the films. Samples were argon ion sputter cleaned before measurements were performed to remove any surface contaminants. Since cleaning may alter the bonding of the sample, care must be taken when analysing bond information. Gaussian peaks were fitted to these binding energy spectra using the Thermo Avantage software, the peak area was calculated, normalised and sensitivity factors of the corresponding peaks were applied to determine the composition.

2.2.4 Optical transmission

Optical transmission spectra were performed on the AZO films to determine their suitability as a transparent conducting oxide (TCO). Transmittance measurements were performed using a Perkin-Elmer Lambda 19 and 950 by spectrophotometry in the wavelength range of 200-2500 nm. The sample must be deposited onto a transparent substrate so that the transmittance of the film can be determined. In a spectrophotometry experiment, a light source is shone onto a monochromator, a device with a diffraction grating used to select a particular wavelength. This monochomated light then passes through the sample and then has its intensity measured using a light sensitive detector. By cycling the monochromator through a variety of wavelengths, the transparency of the films can be determined as a function of wavelength.

2.2.5 Resistivity and Hall measurements

The resistivity (ρ) of a thin film coating is a measure of how strongly it opposes the flow of electrons. In this thesis, TCO's coatings are studied, in which low resistivities are desirable. Routine measurements of the resistance (R, measured using a 4 point probe) and the thickness (t, using step height analysis with a Dektak IIA profilometer) were carried out with each sample. The resistivity of a coating is given by:

$$\rho = R \times t$$

Equation 2-3: The resistivity of a thin film coating

Hall measurements were performed in order to determine the, the carrier concentration (n_e) and the charge mobility (μ) of the samples. Hall effect measurements were performed in the Van der Pauw geometry using an Ecopia HMS3000 system. With this apparatus the resistivity was also determined using the same method outlined above.

In the Hall effect, an electric current travelling in the x direction is subjected to a magnetic field perpendicular to it (z direction). This causes the flow of electrons to drift in the y direction. As the electrons drift, an electric field is generated, exerting a force in the –y direction [21]. At equilibrium (no charge drift) the Hall field is given by:

$$E_H = \frac{j_x B}{n_e e} = R_H j_x B$$

Equation 2-4: The Hall field at equilibrium.

where j_x is the current in the x direction, B is the magnetic field in the z direction, n is the carrier concentration and R_H is the Hall coefficient. Using R_H, the mobility (μ) of the charge carriers can be determined using:

$$\rho = \frac{1}{n_e e \mu}$$

Equation 2-5: Mobility of the charge carriers as a function of the resistivity

2.2.6 Breakdown voltage

The breakdown characteristics of a dielectric thin film are related to the potential at which current flows through it. A requirement for a dielectric film is to able to hold charge without leakage currents due to crystal grain boundaries and quantum tunneling [22-25]. The higher the breakdown field of a metal oxide semiconductor device, the better the performance as a transistor. The electrical breakdown characteristics of the films were measured using lithographically defined NiCr contact pads on the surface of the films, a probing station and a programmable semiconductor parameter. The *E(J)* (leakage) characteristics were obtained using a programmable voltage ramping source and a PC-interfaced digital multimeter. Film thickness measurements (required to calculate the electric-field from applied voltage) were performed using a surface profiler.

2.2.7 Transmission electron microscopy (TEM) sample preparation

Cross sectional TEM (X-TEM) samples were prepared by first mechanical polishing with a tripod polisher and then further thinning with argon ion beams. X-TEM samples allow for the study of films as a function of depth, allowing the microstructure and electronic structure of the films to be thoroughly explored.

The first step for mechanically thinning the samples involves cleaving 3mm x 1mm strips from the samples and preparing strips of blank silicon in the same manner. The pieces are then affixed together using epoxy glue as shown in figure 2-7a. This sandwich structure is affixed to a polished silicon flat on a quartz stub (figure 2-7b) and is then mechanically polished on increasingly fine diamond paper (30µm →9µm→3µm→1µm) until the sample is less than 1µm in thickness (figure 2-7c). An oval shaped copper grid with a section cut out of it is then affixed

to the sample using epoxy glue. The X-TEM sample is then cut out of the structure using a razor blade (figure 2-7d) and lifted from the structure by soaking it in acetone.

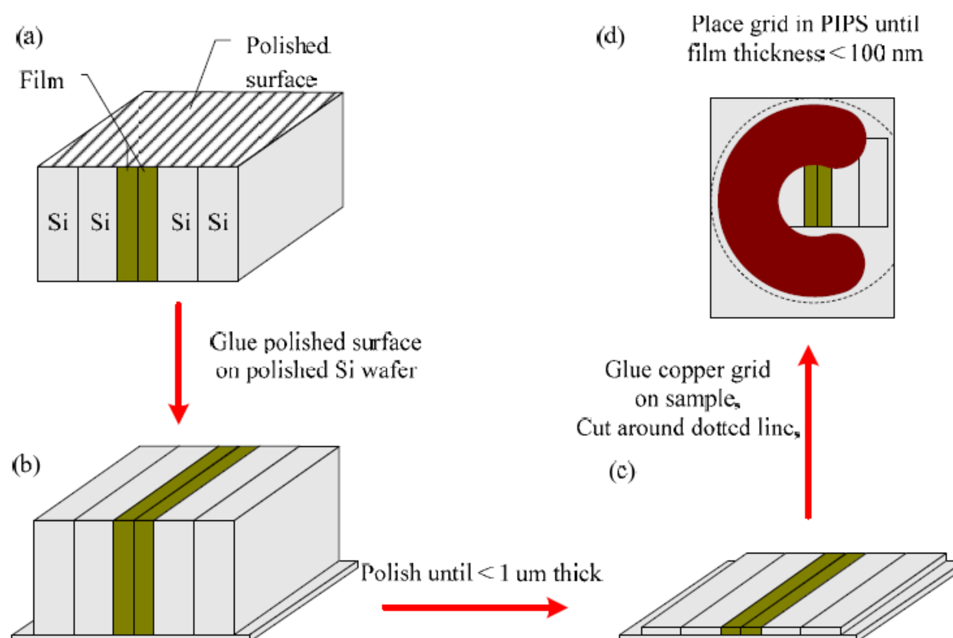

Figure 2-7: Mechanical polishing X-TEM preparation thinning process. This figure has been adapted from Desmond Lau's thesis 2009 [26].

For ion beam thinning of the sample the copper grid with sample attached is placed into the precision ion polishing system (PIPS, Gatan Model 691) where the sample is ion beam thinned until a region surrounding the thin film is less than 100nm in thickness (electron transparent).

X- TEM samples were also prepared using a JEOL ion slicer. Samples were prepared by first epoxy gluing a protective capping material (eg. a microscope coverslip or silicon) on top of the sample of interest. This was then polished down in cross-section to approximately 100 µm in thickness and cut into 2.8 mm x 1 mm pieces. After mechanical polishing, the sample was placed into the ion slicer. An ion gun is positioned above the specimen and a thin masking belt is used to protect the centre region by acting as a sacrificial shield. During milling the sample rocks back and forth parallel to the masking belt to provide even thinning. There are two ion beam milling steps, the first step was a basic thinning of the sample to make a thin channel

down the centre. The second step involves setting the ion gun to thin the region of interest at a selected angle until a hole appears in the specimen.

2.2.8 TEM and selected area electron diffraction (SAED)

TEM is one of the major analytical techniques employed in this thesis to determine the microstructure of the metal oxide thin films. Analysis was performed on either a JEOL 2010 TEM or a JEOL2100F TEM, both fitted with a Gatan imaging filter (GIF) spectrometers. A GIF not only allows the collection of electron energy loss spectroscopy spectra but can also be used to collect energy filtered TEM images [27, 28].

Figure 2-8 shows a basic schematic of the TEM system. Included are ray diagrams to show how the electrons pass through the TEM to provide high resolution images (Figure 2-8a) and diffraction (Figure 2-8b). Electrons are generated from a LaB_6 filament, accelerated to 200kV and then pass through a series of magnetic filters (depicted as ovals in figure 2-8). Images are formed when the flux of electrons are focussed onto the specimen using the condenser lens system, following this the objective lens focuses the image onto the 1st image plane and is thus focussed onto the phosphor screen using the projector lens system. For diffraction, the condenser lens system is used to project a parallel beam through the specimen. In diffraction mode, the projector lens system focuses on the back focal plane of the objective lens, producing a diffraction pattern instead of an image on the viewing screen. Diffraction patterns give a reciprocal space representation of the crystal planes within a film, where the spots appear perpendicular to the planes. Using the distance from the primary beam to a diffraction spot, the d-spacing can be calculated using Bragg's law [29]. In a disordered sample the crystal planes are in many directions, thus the diffraction pattern appears as ring patterns where the d spacings and can be deduced in a similar way.

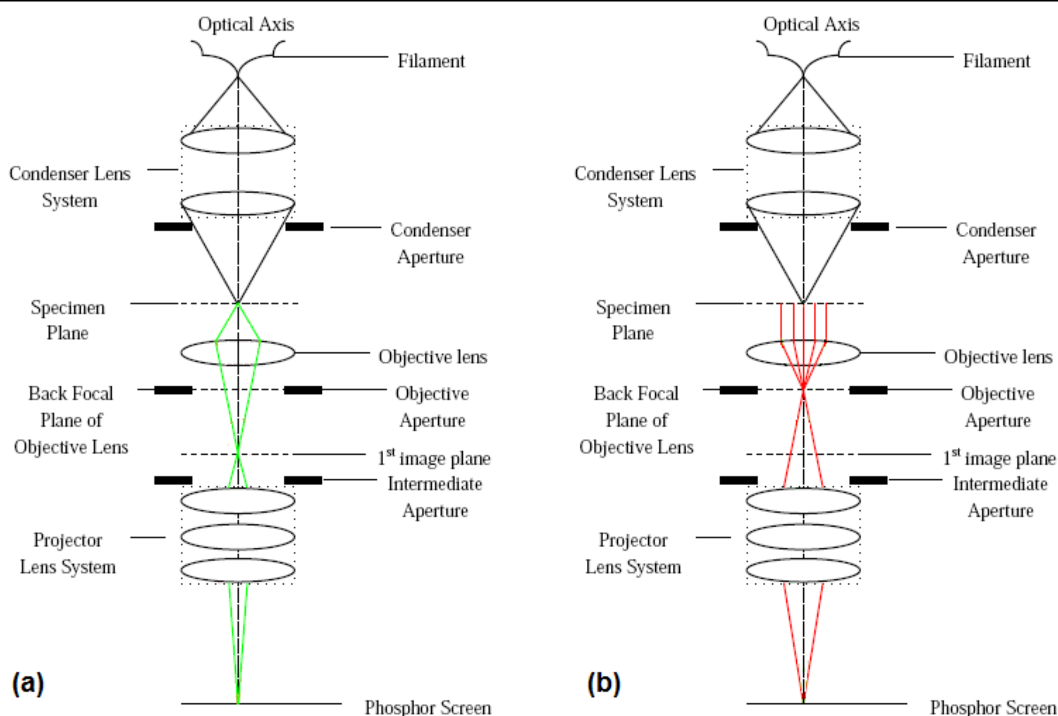

Figure 2-8: Schematic of a TEM. This figure is adapted from Desmond Lau's thesis [26]. The green ray diagram (a) represents the imaging mode of the TEM, and the red ray diagram (b) represents the TEM in diffraction mode.

2.2.9 Electron energy loss spectroscopy (EELS)

EELS is the process in which the energy lost by the electrons in their passage through the specimen is measured using a spectrometer (in the form of a GIF in this thesis). After passing through the specimen the electrons pass through an entrance aperture (in which the radius can be altered) and are then directed onto a magnetic prism by a set of quadrupole and sextapole alignment lenses. Electrons with different energies (velocities) will have a different magnetic force applied to them as they travel through the GIF spectrometer, resulting in them traveling with different trajectories through the magnetic field. High energy electrons that have not lost any energy (zero loss) will be attenuated less, while electrons which have lost a lot of energy due to interactions with the sample will be attenuated more by the magnetic field. The result is a distribution of electron energies projected onto the CCD to form an electron energy loss spectrum.

Figure 2-9 shows the main features of an EELS spectrum. Located at 0 eV is the zero loss peak. This region represents the electrons which have passed through the sample (or missed it entirely) without incurring energy loss. Theoretically this peak would appear as a Dirac-Delta function, but it gains a finite width due to the spread of energies being emitted from the TEM electron gun as well as the resolving power of the spectrometer itself.

Between 0-50 eV is the low loss region, which is dominated by plasmon peaks. This region represents the electrons which pass through the sample and lose a small amount of energy due to plasmon vibrations in the sample.

At higher energies are the core loss ionisation edges. The onset of these edges occur at the energy required to knock out a core electron from a particular atom After the removal of the background, the intensity under these edges can be used to determine the concentration of elements in a sample [27].

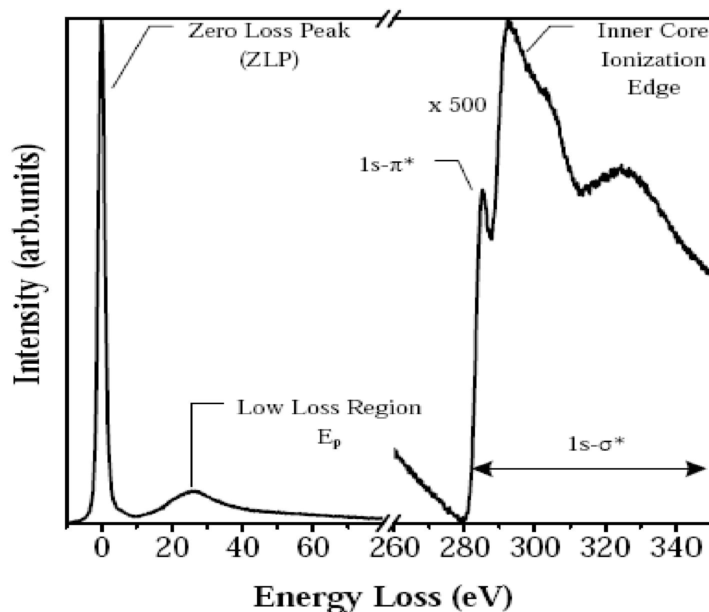

Figure 2-9: The main features of an EELS spectra. At 260 eV the intensity of the spectra has been multiplied by 500 times to show the features of the low intensity core loss edges. The example shown here is the carbon 1s core shell ionization event [26].

2.2.10 Energy loss near edge structure (ELNES)

The core shell event occurs when an incident electron removes an electron from the core shell of an atom and excites it to an unoccupied energy level. The incident electron is inelastically scattered from the atom and the energy of the interaction can be measured using a spectrometer. A schematic of a core shell interaction is shown in figure 2-10. Superimposed on each EELS core loss edge is a fine structure which arises because the final state wave function of the excited electron is modified by chemical bonding. Due to this, the ELNES of a material is representative of the unoccupied density of states and thus contains a large amount of information, including coordination, valence and types of bonding present. In figure 2-9 ELNES on the carbon k-edge can be seen.

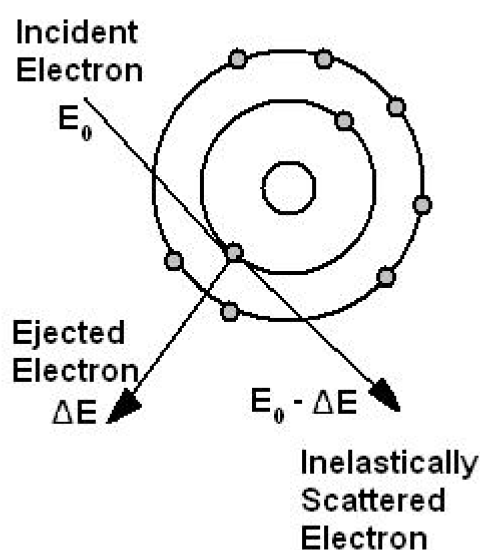

Figure 2-10: Core shell interaction which results in a core loss edge on an EELS spectrum.

2.2.11 X-ray absorption near edge structure (XANES)

X-ray absorption spectroscopy (XAS) is a technique using synchrotron radiation in which the near edge structure (NES) of a core-hole edge is probed with x-rays, revealing a fine structure known as XANES. The technique itself is analogous to the EELS technique in that the local bonding arrangements of a sample can be investigated. But unlike EELS, bulk samples can be

used in the synchrotron, which therefore has the advantage of minimal sample preparation. A disadvantage of XANES is that there is a relatively poor spatial resolution due to the large x-ray beam used (typically ~1 mm). However, XANES has a much better energy resolution than can be achieved in EELS.

In XAS experiments, an x-ray beam is shone onto the sample to excite photoelectrons from the inner shells (core electrons) from atoms in the sample (figure 2-11a). In order for the electron to leave the atom, it must be given sufficient energy by the incident x-rays to be promoted to an unoccupied state above the Fermi energy. Therefore, x-ray absorption spectra, like ELNES, provides information on the unoccupied DOS of the sample. Several different detectors are used to measure the intensity as a function of x-ray energy. After the core shell electron (n) is removed from the atom, a transition will occur where an outer shell electron (n') will fill in the newly created core hole. In dropping down an energy level, the electron releases energy in the form of a photon (figure 2-11b) or Auger electron (figure 2-11c). Photons are measured using a fluorescence detector (known as the fluorescence yield, FY) and the Auger electrons are measured using a hemispherical detector (known as the Auger electron yield, AEY). The other method for obtaining spectra is by monitoring the total electron yield (TEY, also known as the drain), in which the back of the sample is connected to ground through an ammeter and the total number of secondary electrons generated are measured (figure 2-11d).

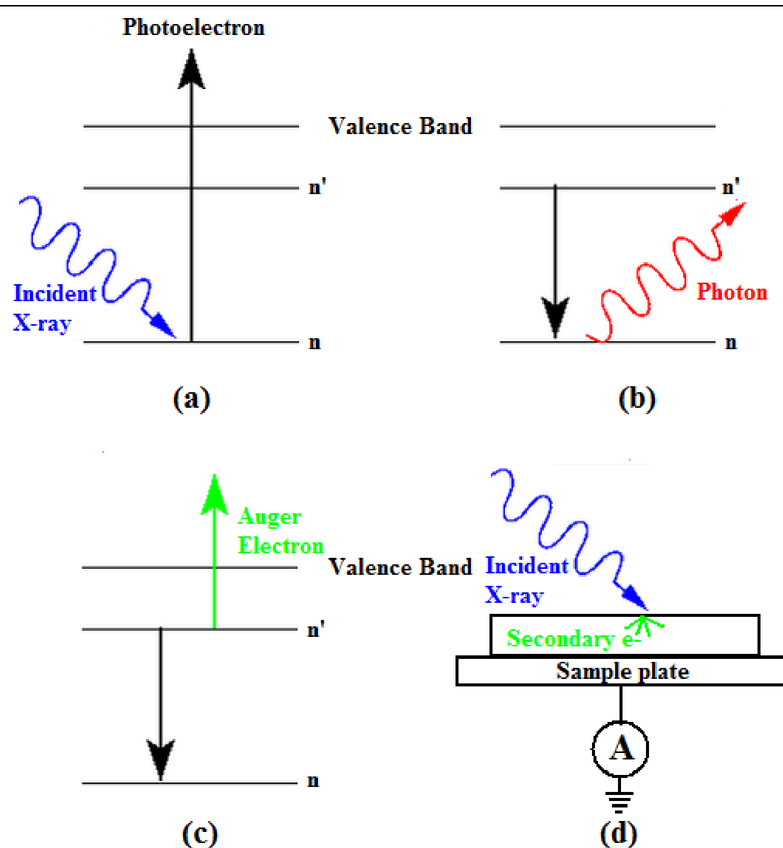

Figure 2-11: The photonic processes involved in x-ray absorption spectroscopy.

The beamline used for this analysis was the soft x-ray beamline at the Australian Synchrotron. A horizontally polarized beam incident at 45° to the substrate normal was used to simultaneously study the FY, TEY and AEY in the vicinity of the oxygen K-edge (525 eV to 560 eV), zinc L-edge (1015 eV-1070 eV) and the aluminium K-edge (1560 eV-1590 eV). For each edge a step size of 0.1 eV was used, a pass energy of 60 eV was used for the oxygen K-edge, and a pass energy of 80 eV was used for the aluminium K-edge and zinc L-edges. The energy of the x-rays was controlled using a monochromator and an elliptically polarised undulator (a variation of the Apple II undulator from Danfysik) in conjunction with a series of mirrors was used to maximise the intensity of the beam at the selected energy. The intensity of the incident beam (I_0) is measured on a gold grid located within the beamline before the analysis chamber. I_0 is used to normalise the data to remove any anomalies due to the cycling of the undulator and the decrease in beam intensity over time.

In the case of oxygen K-edge measurements, it is necessary to take into account that I_0 has features of an oxygen K-edge on it due to the beam interacting with oxygen in beamline components before the sample. To remove this from the data, the beam is shone onto a photodiode within the analysis chamber and the measured intensity is used to normalise the oxygen K-edge spectra taken from each sample using:

$$Spectrum_{Normalised} = \frac{I_{0\,photodiode}}{Signal_{photodiode}} \times \frac{Signal_{(FY,TEYorAEY)}}{I_0}$$

Equation 2-6: Method to normalise the oxygen K-edge to remove variations in signal from the undulator and absorption due to oxygen contaminants on beamline components.

2.3 Theoretical methods

Interpretation of near edge structure is not normally straight forward and accurate theoretical modelling is essential [30]. To assist in the interpretation of core loss edges from ELNES (2.2.10) and XANES (2.2.11) *ab initio* codes were employed. Given that the near edge structure is dependent on the local bonding environment, it is possible to use these codes to simulate the near edge structure for a variety of possible phases. These calculations can then be compared to the experimentally determined near edge structure (using EELS or XAS). Two different codes for calculating near edge structure were employed known as FEFF and WIEN2k.

2.3.1 Multiple scattering calculations using the FEFF code

FEFF is a real space multiple scattering code which is used to simulate the near edge structure of clusters representing the metal oxide thin films. The benefit of using a real space code is that it can be used for periodic and non-periodic materials alike. Real space codes were once thought to be inaccurate compared to their band structure counterparts, but this is often not the

case [31] with improvements of the codes and the inclusion of self consistent field potential calculations giving which compare well to experimental data [32-35].

The FEFF code uses a muffin tin potential scheme, in which the initial potential of the crystal is a set of circularly symmetric atomic potentials located at each atom position (figure 2-14). Regions I_1 and I_2 refer to the areas surrounding the atoms in which the net potential V(r) is constructed using the coulomb potentials $V_c^i(r_i)$ and exchange potentials $V_{X\alpha}^i(r_i)$. The net potential within these regions is given by:

$$V(r) = \sum_i V_c^i(r_i) + V_{X\alpha}^i(r_i)$$

Equation 2-7: The net potential within the muffin tin regions in the FEFF calculations

which is expressed as a series of spherical harmonics, and by taking only the first spherically symmetric term (l = m = 0) the potential assumes a 'muffin tin' form. Region II, the 'inner potential', is taken to be a constant averaged value. The potential in region III is averaged with respect to the centre of the crystal [36].

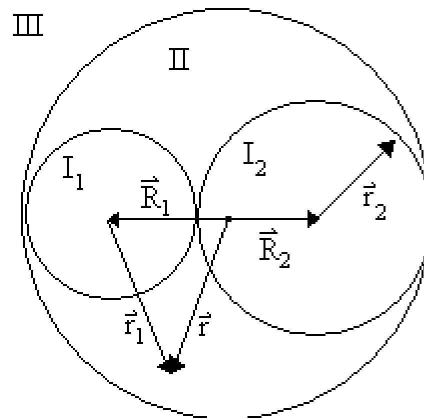

Figure 2-12: Muffin-tin potential calculated in the self consistent field calculation [36].

After the potential of the system has been calculated, the multiple scattering part of the code follows. ELNES and XANES are formally given by Fermi's golden rule. The probability of core electron moving from an initial state (i) into a final state (f) is given by:

$$\mu_a(E) \propto \sum_f^{E_f>E_F} \left| \langle f|\hat{\varepsilon}\cdot r|i\rangle \right|^2 \delta(E-E_f)$$

Equation 2-8: Fermi's golden rule, describing the probability of core-level electron transition.

where $\hat{\varepsilon}\cdot r$ is the dipole operator for the incident electromagnetic wave interacting with the material and the sum is over all energies above the Fermi energy (E_f). When the atom absorbs the incident electron or x-ray and the core hole is formed, the ejected photoelectron propagates outwardly and scatters from surrounding atoms until the core hole is refilled [33]. Figure 2-13 shows a representation of the photoelectron wavefront scattering from multiple atoms within a material. Each of these paths must be considered as these multiple scattering events add towards the final near edge structure on the EELS and XAS core loss edges.

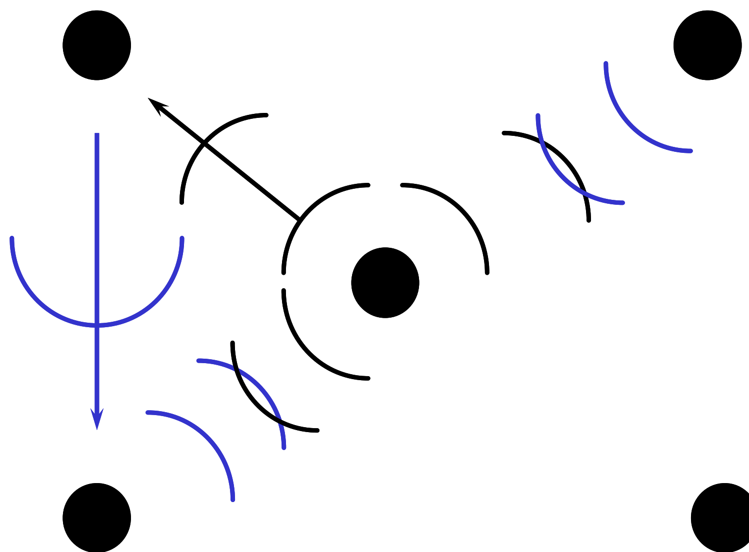

Figure 2-13: Multiple scattering with the wavefront scattering between multiple atoms in the material until the core-hole is refilled.

The input structure files for the FEFF code were generated using the atoms code [37]. Into this program it is possible to insert the space group, the lattice parameters, the electron shell to be studied, the size of the atomic cluster as well as the crystallographic coordinates of each of the atoms in the unit cell. The FEFF code often calculated the Fermi energy incorrectly. The

correct Fermi energy was found by examining the DOS and determining the energy of the gap between occupied and unoccupied states. Calculations were run repeatedly with increasing number of shells of atoms until increases in cluster size no longer resulted in differences in near edge structure. Lorentzian broadening to account for experimental and lifetime broadening in the ELNES and XANES was included in the calculations by adding an imaginary "optical" potential using the EXCHANGE card [32]. An important consideration when calculating the NES of a structure is the core-hole effect, which may affect the potentials within the muffin tin radius. FEFF uses a self consistent fully screened core-hole, which acts in shifting the spectra to lower energies while increasing the intensity of the main peak [32].

In this thesis, two versions of the FEFF code were used to calculate the near edge spectra. FEFF8.2 (which will be referred to as FEFF8 for the remainder of this thesis) was used in chapters 3 and 5. FEFF9, the latest version of the code, was used in chapter 4.

2.3.2 Band structure calculations using the WIEN2k code

Band structure calculations are performed in reciprocal space and are based on density functional theory in which the electronic structure of many body systems is calculated [38, 39]. From this it is possible to calculate many ground state properties, such as optical constants, density of states, low loss spectra and high loss spectra. The band structure calculations in this thesis were performed using the WIEN2k code which uses parameters provided in an input file to calculate many properties of a crystal. Band structure calculations have the benefit of being able to calculate many physical properties, however the main drawback for using this technique is that the properties are calculated for the ground state [40]. Despite this, WIEN2k has been shown [40-43] to give good results in the simulation of XANES and ELNES spectra. For the WIEN2k calculations in this thesis, the electron wavefunctions and eigenvalues were calculated by the full-potential (linearised) augmented plane-wave ((L)APW) + local orbitals (lo) method. Exchange and correlation were treated using the generalized gradient approximation (GGA).

2.4 Bibliography

1. Shi, X., B.K. Tay, H.S. Tan, E. Liu, J. Shi, L.K. Cheah, and X. Jin, *Transport of vacuum arc plasma through an off-plane double bend filtering duct.* Thin Solid Films, 1999. **345**(1): p. 1-6.
2. Tay, B.K., G.F. You, S.P. Lau, and X. Shi, *Plasma flow simulation in an off-plane double bend magnetic filter.* Surface and Coatings Technology, 2000. **133-134**: p. 593-597.
3. Brown, I.G. and X. Godechot, *Vacuum arc ion charge-state distributions.* Plasma Science, IEEE Transactions on, 1991. **19**(5): p. 713-717.
4. Bilek, M.M.M., *The effect of magnetic field configuration on plasma beam profiles in curved magnetic filters.* Journal of Applied Physics, 1999. **85**(9): p. 6385-6391.
5. Anders, A., *Physics of arcing, and implications to sputter deposition.* Thin Solid Films, 2006. **502**(1-2): p. 22-28.
6. Aksenov, I.I., V.A. Belous, V.G. Padalka, and V.M. Khoroshikh, *Transport of plasma streams in a curvilinear plasma-optics system.* Soviet Journal of Plasma Physics, 1978. **4**: p. 425-428.
7. Anders, A., *Cathodic Arcs: From Fractal Spots to Energetic Condensation*, ed. L.B.N. Laboratory. 2003: Springer.
8. Xu, S., B.K. Tay, H.S. Tan, L. Zhong, Y.Q. Tu, S.R.P. Silva, and W.I. Milne, *Properties of carbon ion deposited tetrahedral amorphous carbon films as a function of ion energy.* Journal of Applied Physics, 1996. **79**(9): p. 7234-7240.
9. Lau, D.W.M., D.G. McCulloch, M.B. Taylor, J.G. Partridge, D.R. McKenzie, N.A. Marks, E.H.T. Teo, and B.K. Tay, *Abrupt Stress Induced Transformation in Amorphous Carbon Films with a Highly Conductive Transition Phase.* Physical Review Letters, 2008. **100**(17): p. 176101.
10. Anders, A., S.H.N. Lim, K.M. Yu, J. Andersson, J. Rosén, M. McFarland, and J. Brown, *High quality ZnO:Al transparent conducting oxide films synthesized by pulsed filtered cathodic arc deposition.* Thin Solid Films, 2010. **518**(12): p. 3313-3319.
11. Bräuer, G., B. Szyszka, M. Vergöhl, and R. Bandorf, *Magnetron sputtering - Milestones of 30 years.* Vacuum, 2010. **84**(12): p. 1354-1359.
12. Chapin, J.S., *'Sputtering process and apparatus', US patent #4,166,018.*, in *Vacuum Technology*. (1974).
13. Kouznetsov, V., K. Macák, J.M. Schneider, U. Helmersson, and I. Petrov, *A novel pulsed magnetron sputter technique utilizing very high target power densities.* Surface and Coatings Technology, 1999. **122**(2-3): p. 290-293.
14. Ehiasarian, A.P., R. New, W.D. Münz, L. Hultman, U. Helmersson, and V. Kouznetsov, *Influence of high power densities on the composition of pulsed magnetron plasmas.* Vacuum, 2002. **65**(2): p. 147-154.
15. Gudmundsson, J.T., J. Alami, and U. Helmersson, *Evolution of the electron energy distribution and plasma parameters in a pulsed magnetron discharge.* Applied Physics Letters, 2001. **78**(22): p. 3427-3429.
16. Lin, J., J.J. Moore, W.D. Sproul, B. Mishra, and Z. Wu, *Modulated pulse power sputtered chromium coatings.* Thin Solid Films, 2009. **518**(5): p. 1566-1570.
17. VlCek, J., P. KudlaCek, K. Burcalova, and J. Musil, *High-power pulsed sputtering using a magnetron with enhanced plasma confinement.* Journal of Vacuum Science & Technology A: Vacuum, Surfaces, and Films, 2007. **25**(1): p. 42-47.
18. Modreanu, M., J. Sancho-Parramon, D. O'Connell, J. Justice, O. Durand, and B. Servet, *Solid phase crystallisation of HfO2 thin films.* Materials Science and Engineering B, 2005. **118**(1-3): p. 127-131.
19. Gullapalli, S.K., R.S. Vemuri, and C.V. Ramana, *Structural transformation induced changes in the optical properties of nanocrystalline tungsten oxide thin films.* Applied Physics Letters, 2010. **96**(17): p. 171903-171903-3.

20. Birks, L.S. and H. Friedman, *Particle Size Determination from X-Ray Line Broadening.* Journal of Applied Physics, 1946. **17**(8): p. 687-692.
21. Hall, E.H., *On a New Action of the Magnet on Electric Currents.* American Journal of Mathematics, 1879. **2**(3): p. 287-292.
22. Forsgren, K., A. Harsta, J. Aarik, A. Aidla, J. Westlinder, and J. Olsson, *Deposition of HfO_2 Thin Films in HfI_4-Based Processes.* Journal of The Electrochemical Society, 2002. **149**(10): p. F139-F144.
23. Rangarajan, V., H. Bhandari, and T.M. Klein, *Comparison of hafnium silicate thin films on silicon (1 0 0) deposited using thermal and plasma enhanced metal organic chemical vapor deposition.* Thin Solid Films, 2002. **419**(1-2): p. 1-4.
24. Moon Sig, J., C. Byung Jin, Y. Chia Ching, D. Siu Hung Chan, W. Sung Jin, S. Mathew, L. Kanta Bera, N. Balasubramanian, and K. Dim-Lee, *Formation of hafnium-aluminum-oxide gate dielectric using single cocktail liquid source in MOCVD process.* Electron Devices, IEEE Transactions on, 2003. **50**(10): p. 2088-2094.
25. Choi, C.H., S.J. Rhee, T.S. Jeon, N. Lu, J.H. Sim, R. Clark, M. Niwa, and D.L. Kwong. *Thermally stable CVD HfO_xN_y advanced gate dielectrics with poly-Si gate electrode*. in *Electron Devices Meeting, 2002. IEDM '02. Digest. International*. 2002.
26. Lau, D., *Characterisation of Novel Carbonaceous Materials Synthesised Using Plasmas*. 2009, RMIT University: Melbourne.
27. Egerton, R.F., *Electron Energy-Loss Spectroscopy in the Electron Microscope*. 2 ed. 1996, New York
London: Plenum Press. 227-243.
28. Brydson, R., *Electron Energy Loss Spectroscopy*. Microscopy Handbooks. 2001: BIOS Scientific Publishers Limited.
29. Pieranski, P., *Colloidal crystals.* Contemporary Physics, 1983. **24**(1): p. 25 - 73.
30. Keast, V.J., A.J. Scott, R. Brydson, D.B. Williams, and J. Bruley, *Electron energy-loss near-edge structure - a tool for the investigation of electronic structure on the nanometre scale.* Journal of Microscopy, 2001. **203**(2): p. 135-175.
31. Rehr, J.J. and R.C. Albers, *Theoretical approaches to x-ray absorption fine structure.* Reviews of Modern Physics, 2000. **72**(3): p. 621.
32. Moreno, M.S., K. Jorissen, and J.J. Rehr, *Practical aspects of electron energy-loss spectroscopy (EELS) calculations using FEFF8.* Micron, 2007. **38**(1): p. 1-11.
33. Ravel, B., *A practical introduction to multiple scattering theory.* Journal of Alloys and Compounds, 2005. **401**(1-2): p. 118-126.
34. Hallmeier, K.H., I. Uhlig, and R. Szargan, *Sulphur L2,3 and L1 XANES investigations of pyrite and marcasite.* Journal of Electron Spectroscopy and Related Phenomena, 2002. **122**(1): p. 91-96.
35. Ankudinov, A.L., J.J. Rehr, J.J. Low, and S.R. Bare, *Theoretical Interpretation of XAFS and XANES in Pt Clusters.* Topics in Catalysis, 2002. **18**(1): p. 3-7.
36. Stohr, J., *NEXAFS Spectroscopy*. Springer Series in Surface Sciences. Vol. 25. 1992.
37. Ravel, B., *Webatoms*. 2003, http://cars9.uchicago.edu/cgi-bin/atoms/atoms.cgi.
38. Hohenberg, P. and W. Kohn, *Inhomogeneous Electron Gas.* Physical Review, 1964. **136**(3B): p. B864.
39. Kohn, W. and L.J. Sham, *Self-Consistent Equations Including Exchange and Correlation Effects.* Physical Review, 1965. **140**(4A): p. A1133.
40. Hebert, C., *Practical aspects of running the WIEN2k code for electron spectroscopy.* Micron, 2007. **38**(1): p. 12-28.
41. Holec, D., P.M.F.J. Costa, P.D. Cherns, and C.J. Humphreys, *A theoretical study of ELNES spectra of AlxGa1-xN using Wien2k and Telnes programs.* Computational Materials Science, 2008. **44**(1): p. 91-96.
42. Soldatov, A., G. Yalovega, G. Smolentsev, A. Kravtsova, D. Lamoen, C. Balasubramanian, A. Marcelli, G. Cinque, and S. Bellucci, *ALN nanoparticles XANES analysis: Local atomic and electronic structure.* Nuclear Instruments and Methods in Physics Research Section A: Accelerators, Spectrometers, Detectors and Associated Equipment, 2007. **575**(1-2): p. 85-87.

43. Kunisu, M., F. Oba, H. Ikeno, I. Tanaka, and T. Yamamoto, *Local environment of Mn dopant in ZnO by near-edge x-ray absorption fine structure analysis.* Applied Physics Letters, 2005. **86**(12): p. 121902-3.

Chapter 3

The microstructure and electronic structure of tungsten oxide thin films

In this chapter, the microstructure of tungsten oxide (WO_3) thin films prepared using pulsed magnetron sputtering and pulsed cathodic arc deposition is investigated. As discussed in chapter 2, the differences between these two techniques are significant. Cathodic arc deposited films are formed from energetic and charged ions while sputtered films are deposited primarily from low energy neutrals. Transmission electron microscopy (TEM) and electron energy-loss spectroscopy (EELS) are used to characterize the films. The oxygen K-edge measured with EELS provides a convenient way of distinguishing between the various phases of WO_3. In addition to experimental measurements, this chapter employs theoretical calculations to calculate the near edge structure (NES) which is present on each oxygen k-edge for different phases or WO_3. These calculated edges are used to help identify the particular phase of WO_3 present in the samples.

3.1 Introduction

As discussed in chapter 1, transparent conductive oxides (TCO's) are of growing interest to the scientific community for the purposes of solar cell research and energy saving applications [1]. Electrochromic (EC) coatings have the ability to reversibly change their optical properties by applying a small on/off voltage. These properties have led to many applications including anti dazzling rear view mirrors and various display devices [2, 3]. Of specific interest for tungsten oxide is the production of 'smart windows' [4]. Using the electrochromic effect it is possible to manufacture a window with reversible colouration change simply by applying a small voltage. This is important in energy saving applications, in that large office buildings can be fitted with these windows and be heated or cooled by controlling the amount of IR radiation allowed into the building.

3.1.1 Tungsten oxide as a TCO

Of all the transition metal oxide materials studied thus far, WO_3 is one of the most extensively studied [5-7]. In addition to EC applications, WO_3 has also been investigated for use in gas sensing [8], biosensors [9], superconductors [10], imaging recording [11] and optical storage [12]. Many of these applications require the preparation of high quality thin films. Therefore, it is important to investigate how different deposition techniques give rise to different film microstructure. Before considering previous work on tungsten oxide thin films, in the next section, the type of structures that tungsten oxide forms in the bulk is discussed.

3.1.2 The crystal structure of WO_3

Bulk crystalline WO_3 is known to have a perovskite type structure which at atmospheric pressure undergoes several phase changes depending on temperature [13, 14]. However, all of the tungsten oxide phases are made up of a basic structure comprised of many WO_6 octahedral units. The details of the structure including the W-O distance and the tilting of the octahedral

units determines the symmetry of the material. Figure 3-1 shows an example of an individual WO_6 octahedral unit and several joined units forming the monoclinic γ-WO_3 phase.

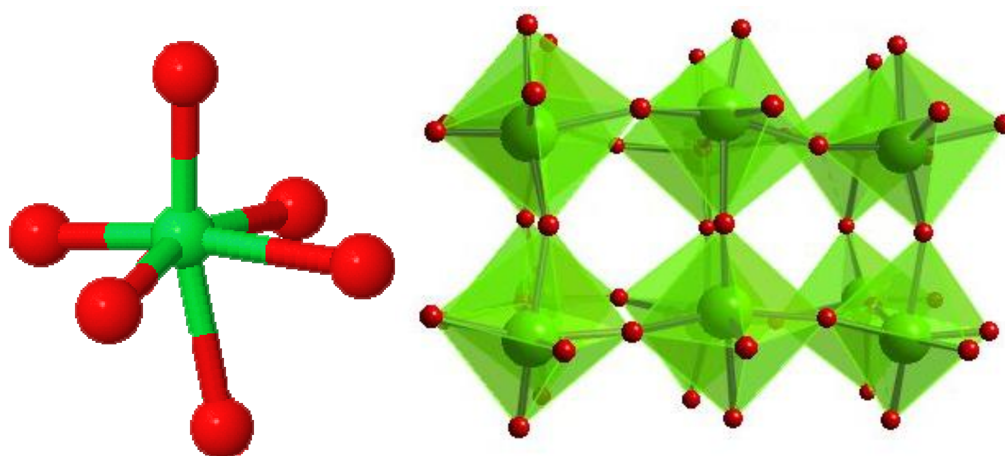

Figure 3-1: An individual WO_6 octahedral unit (left) where the green sphere represents the tungsten atom and the red spheres represent the oxygen atoms. When combined these octahedral units can form the monoclinic γ-WO_3 structure (right) with the different amounts of tilt on the highlighted WO_6 octahedral units [15].

Many different phases of WO_3 have been reported. A summary of these are shown in table 3-1, including details of the space groups and lattice parameters found in the individual studies for each phase. The relevant references are shown in the table.

Salje et. al [16] have reported a low temperature monoclinic (ε) phase. These samples were prepared by first heating a commercial WO_3 powder to 800ºC for two days and then rapidly heating the sample to 1480ºC for two hours. The sample was then allowed to cool to room temperature over a period of 2 days before experimental work was undertaken. The samples were ground and cooled down to 5 K by placing them into a rectangular can and cooling it with a He-flow cryostat while neutron powder diffraction data was taken. Structure refinement calculations were performed to determine the lattice parameters and the fractional atomic coordinates for the heating and cooling between 5 K and 250 K.

Table 3-1: Details of the crystallography of the phases of WO_3 and the method of formation of the bulk crystal. Those marked with 'Powder' in the formation method were a commercially purchased polycrystalline powder of unspecified phase.

Structure	Symmetry	Space Group	Lattice Parameters	Formation method
–	Tetragonal	P4/ncc	a= 5.2885 Å c= 7.8626 Å	Powder → 1373 ºC [17]
α–WO_3	Tetragonal	P4/nmm	a=5.3031 Å c=3.9348 Å	Powder → 740 ºC [14, 17]
β-WO_3	Orthorhombic	Pmnb	a=7.341 Å b=7.570 Å c=7.754 Å	Powder → 480 ºC [14, 18]
γ-WO_3	Monoclinic	$P2_1/n$	a=7.30084 Å b=7.53889 Å c=7.68962 Å α=γ=90° β= 90.892°	Room temp [14, 19]
δ-WO_3	Triclinic	$P\bar{1}$	a=7.31278 Å b=7.52540 Å c=7.68954 Å α=88.847° β=90.912° γ=90.940°	Powder → 1200 ºC →800 ºC →room temp →LN2 cooled → room temp [14, 16, 19]
ε-WO_3	Monoclinic	Pc	a=5.27710 Å b=5.15541 Å c=7.66297 Å β=91.97592°	Powder →800 ºC →1480 ºC →room temp → -50 ºC [14, 16]

Aird *et*. al [13] and Woodward *et*. al [19] report a mixing of phases at room temperature. Both have reported evidence of a triclinic phase (δ) and another monoclinic phase (γ). In these works, Aird et al synthesised WO_3 by recrystallising WO_3 powder to small single crystals by annealing it within a furnace at temperatures up to 1723 K before cooling it back to room temperature. Aird then went on to perform reduction experiments on the newly formed powder samples and compared x-ray diffraction data and the sheet superconductivity between the

reduced sample and the fully stoichiometric WO_3. In the study performed by Woodward et al [19], neutron powder diffraction was performed on WO_3 samples that had first been heated to 1200ºC in air, and then cooled in stages to room temperature. It was found that the samples contained mixed phases of both triclinic (δ) and monoclinic phases (γ). The sample was then cooled in liquid nitrogen and then allowed to heat back up to room temperature. Repeating the same neutron diffraction experiment yielded only single phase triclinic WO_3. Using this neutron data, Rietveld structure refinement calculations were performed to determine the lattice parameters and the oxygen/tungsten positional parameters of the triclinic structure.

At elevated temperatures of 480ºC and 770ºC γ-WO_3 transforms into orthorhombic (β) and then to tetragonal (α) phases respectively. The β-WO_3 was studied by Salje et al [18] in which γ-WO_3 crystals were placed onto nickel wire and heat treated to form orthorhombic crystals of space group Pnmb. The lattice parameters a,b and c as well as the atomic positions of the 2 unique tungsten atoms and 8 unique oxygen atoms were determined using x-ray analysis.

The α-WO_3 phase was studied and refined by Locherer in 1999 [17] using *ab initio* calculations. In this work the superconductive nature of WO_3 was studied, as well as the existence of further tetragonal phases when the sample is heated beyond 1100 K. At this high temperature, a new tetragonal phase (shown in table 3-1 with space group P4/ncc) was found with slightly different lattice parameters, as well as slight shifting in the WO_6 octahedra about the [001] direction.

3.1.3 Growth of thin films of WO_3

WO_3 films have been deposited using several methods including sputtering [5, 6], evaporation [20, 21], pulsed laser deposition [22] and filtered cathodic arc deposition [23]. In general, the microstructure and performance of the films depends on the method, deposition temperature and other process conditions, with both amorphous and polycrystalline materials reported [24].

In the work by Cui et al [5], a dc magnetron sputterer was used to deposit the WO_3 films grown specifically for the purpose of smart windows. It was found that the films were initially amorphous, however the microstructure changed and monoclinic crystals formed following annealing to 500ºC. Given the importance of this research for smart windows, it would have been very important for this study to perform electron microscopy and diffraction on the films to get a stronger understanding of the microstructure being deposited. It has been accepted that highly disordered films perform better as EC devices [25], so it would also have been interesting for the authors to have published transmittance and electrical measurements on the 500ºC film to see how great a change in these properties a crystalline film has over an amorphous film.

Gillet et al [20] and Shigesato et al [21] used a simple thermal evaporator for deposition. Gillet deposited the WO_3 films onto an alumina substrate and found that the as-deposited films were highly disordered and showed broad rings in the reflection high energy electron diffraction (RHEED) patterns. Annealing these films resulted in the crystals aligning and an observable single crystal diffraction which was indexed to a <001> oriented monoclinic structure. TEM and electron diffraction data is presented in this paper clearly showing the difference in microstructures between the two films. Shigesato used Raman Spectroscopy to study WO_3 films evaporated onto glass substrates. It was found that the as-deposited films were amorphous, but crystallinity of the films increased when annealed between 40ºC and 145ºC. Although both of these thermal evaporation studies of WO_3 look at many aspects of the films, neither of them probe the electronic structure of the films. This could have been performed easily with x-ray photoelectron spectroscopy (XPS), EELS or x-ray absorption spectroscopy (XAS). This not only would have allowed for confirmation that the deposited films were stoichiometric, but it would have given in depth knowledge on the bonding configurations between the tungsten and oxygen atoms.

Pulsed laser deposition (PLD) has been used for the deposition of WO_3 films by Rougier et al [22]. PLD is an interesting technique, because in using a high powered laser to ablate a tungsten target. A highly energetic plasma plume forms, similar to that found in a cathodic arc. In the work by Rougier [22], the WO_3 films were deposited onto SnO_2:F substrates, and it was found that the crystallinity of the films was highly dependent on the oxygen partial pressure and the temperature. All of the films deposited at room temperature were found to be amorphous, but those deposited at 400ºC with a partial pressure of 10^{-2} mbar were found to contain monoclinic crystals. Higher partial pressures (10^{-1} mbar), regardless of the deposition temperature always resulted in an amorphous structure. The x-ray diffraction results in this paper suggest that a new third phase (thought to be a cubic phase) appears when the substrate is heated to 400ºC but a detailed phase analysis was not undertaken. It is noted that for a better knowledge of the structure that TEM measurements were to be pursued. This in combination with EELS and *ab initio* techniques would certainly provide the necessary structural information so that this third phase could be characterised.

It is clear that the microstructure of WO_3 films is highly dependent on the deposition method. In this chapter, the microstructure of WO_3 films prepared using pulsed magnetron sputtering [26, 27] and pulsed cathodic arc are compared [28-30]. These techniques were selected because film growth occurs from differing regimes; one which utilises a high energy plasma compared to one which deposits via low energy neutrals. The change in incident energy of the depositing particles is known to have an important influence on the microstructure of the films [31, 32]. Both techniques were performed at room temperature with approximately the same base and oxygen partial pressures.

In my honours project [33], I performed some preliminary spectroscopy and TEM measurements on pulsed magnetron and pulsed cathodic arc tungsten oxide films. These results showed a disordered structure in the magnetron sample and that the films were close to stoichiometric. The work presented in this chapter was all performed after the completion of

my honours project and includes much more detailed measurements including high resolution TEM imaging, diffraction patterns as well as the use of the *ab initio* calculations to help interpret the NES observed on the absorption edges measured using EELS.

3.2 Experimental Techniques

3.2.1 Deposition using pulsed cathodic arc

Details of the cathodic arc deposition system are provided in chapter 2, For the WO_3 depositions, the chamber was pumped down to a base pressure of about 7 x 10^{-6} Torr (9 x 10^{-4} Pa) and backfilled with O_2 at a flow rate of 10 sccm to a pressure of about 6.6 mTorr (0.88 Pa). The pulsed arc source [34], equipped with a tungsten rod cathode and a 90° open-coil macroparticle filter, was fed from a switched capacitor bank (0.3 F) charged to 270 V, resulting in an arc current of about 180 A, limited by a 1.5 Ω resistor in series. The arc repetition rate was 3 pulses per second each with a duration of 3 ms. After 7600 pulses, a film thickness of 200 nm was obtained, with the holder placed about 90 mm from the filter exit. Throughout the deposition process, the sample holder was pulsed-biased to -200 V with pulse cycle of 10 μs on (-200 V) and 90 μs off (ground).

3.2.2 Deposition using magnetron sputtering

The magnetron sputtering was performed in the system outlined in chapter 2. The chamber was initially pumped down to a base pressure of about 1.3x10^{-6} Torr (1.7 x 10^{-4} Pa) using a cryogenic pump with a pumping speed of 1500 l/s. The pumping speed was reduced using an adjustable gate valve to obtain a relatively high total pressure of 42 mTorr (5.6 Pa) with Ar and O_2 gas flows of 50 and 40 sccm, respectively. The gas was introduced into a gas plasma source of the constricted plasma source type [35] operated with a Pinnacle Plus power supply at 1500 W (pulsed-DC, 100 kHz, 1 μs reverse time). It was noted that the total pressure was reduced to about 36 mTorr (4.8 Pa) during deposition, which is due to the consumption of oxygen by the

growing film. A 76 mm diameter W target with a sputter power of 1200 W was used. The substrate was placed 90 mm away from the sputtering gun and the plasma source. Total deposition time was 10 mins.

3.2.2 Theoretical methods

Using the structures outlined in table 3-1, *ab initio* simulations were performed to calculate the oxygen K-edge using both multiple scattering and band structure calculations.

The multiple scattering calculations were performed using the FEFF8 code (outlined in section 2.6). Cluster sizes of up to approximately 150 atoms as found to be sufficient to obtain convergence. A core-hole following the final state rule was used because it was found to provide a better approximation of the NES. A muffin-tin overlap of 15% was employed and the Hedin–Lundqvist exchange potential was used as it is recommended for solids [36]. Each of the WO_3 structures listed in table 3-1 has multiple unique oxygen positions in the unit cell. Therefore, the NES of each unique oxygen atom was modelled separately and then combined to provide an average. Unbroadened spectra were used to compare the features on the calculated WO_3 phases. Lorentzian broadening of 1.3 eV was included into the calculation by adding the imaginary optical potential (as detailed in section 2.3.1) in order to compare with the experimental ELNES and XANES spectra.

For the WIEN2k calculations, the parameter determining the size of the basis set, $R_{MT}K_{MAX}$, was set to 7. The muffin tin radii were chosen as large as possible but without overlapping spheres. The number of k-points in the irreducible Brillouin zone (BZ) was 90 for α-WO_3 and 54 for γ-WO_3. Convergence tests showed that this number of k-points were adequate. A core-hole was not included in the results presented here, as it only changed the relative intensity of peaks by a small amount, but with a considerable increase in computational time. The oxygen K-edge was calculated using the XSPEC subroutine within WIEN2k. Spectra were calculated

for all inequivalent positions in the unit cell and an appropriate average taken. Differences between the different atomic sites were very small. Lorentzian broadening of 1.3 eV was included to account for the experimental energy resolution.

3.3 Results and Discussions

3.3.1 X-ray photoelectron spectroscopy (XPS)

Figure 3-2 shows XPS spectra in the region of the tungsten 4f7 and 4f5 binding energy peaks for the films with the indicated deposition method. Figure 3-3 shows the corresponding spectra for the oxygen 1s binding energy peaks. It can be seen that over the relatively large area of analysis the spectra for the pulsed cathodic arc and the pulsed magnetron sputtered samples are near identical, indicating that both films have similar bonding. This is not unexpected since all tungsten oxide samples are comprised of WO6 octahedral units with only slight distortions between phases. It is important to remember the possibility that the sputter cleaning used to remove contaminants also could damage the sample, altering the bonding at the surface.

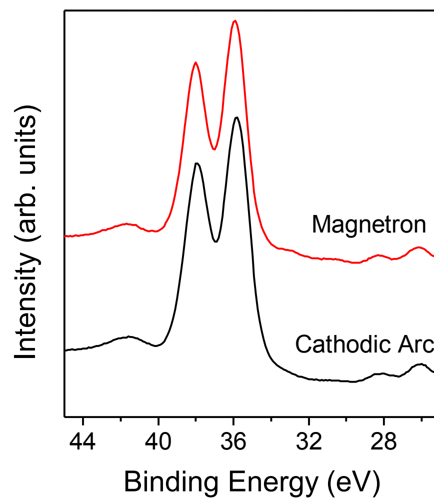

Figure 3-2: Tungsten 4f XPS binding energy peaks. Both samples have equivalent peaks with no shift in the binding energy.

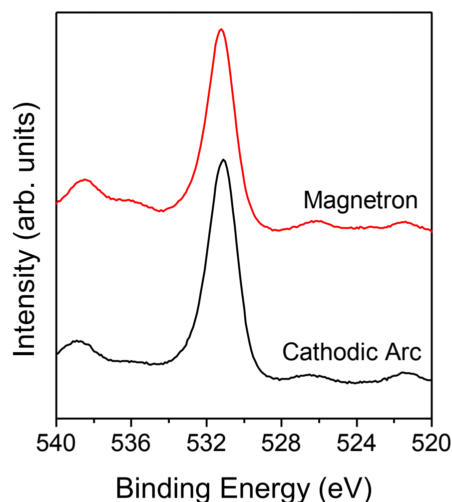

Figure 3-3: Oxygen 1s XPS binding energy peaks. Both samples have equivalent peaks with no shift in the binding energy.

With sensitivity factors applied, the normalised areas of the spectra are compared to acquire the relative oxygen/tungsten atom ratio within the film area. The stoichiometry of the sputtered and cathodic arc deposited films was determined to be $WO_{2.87}$ and $WO_{2.73}$, respectively. These films were found to be close to stoichiometric, with a slightly reduced oxygen concentration, probably due to preferential sputtering of oxygen during the sputter clean.

3.3.2 Cross sectional transmission electron microscopy (TEM)

Cross-sectional TEM images are shown in figures 3-4a and 3-4b for the pulsed magnetron and pulsed arc samples respectively. The figures show the glass substrate on the left hand side of the TEM micrographs, the sample running down the centre of the micrographs and sample bonding glue used for the TEM sample preparation on the right hand side. The pulsed magnetron sample (shown in figure 3-4a) appeared to be highly disordered and crystallites were not able to be found within the film. This was confirmed by the selected area diffraction image of the area shown in figure 3-5a in previous work [33, 37] . The rings around the centre spot of the primary beam indicate that the sample is highly disordered, and it was not possible to index

this diffraction pattern. Amorphous WO_3 has been seen previously in thin film form deposited both with magnetron sputtering [37] and other deposition techniques [6, 21].

The pulsed cathodic arc sample is shown in figure 3-4b. The TEM image shows small crystallites within the sample and the film itself appeared darker than the pulsed magnetron sample. The inset of this figure shows a high resolution TEM image of one of these crystallites, which reveals a highly ordered crystal lattice. Figure 3-5b shows the selected area diffraction pattern of this area and it can be clearly seen that this area exhibits a highly ordered crystalline structure. The pattern has been indexed to the α-WO_3 phase. This is an interesting result given that previous investigations of WO_3 films prepared using physical deposition methods have exhibited a γ–WO_3 structure [20, 22, 24]. The energetic plasma associated with cathodic arc deposition clearly had an impact on the microstructure on the resulting WO_3 producing the high temperature α-phase with improved crystallinity.

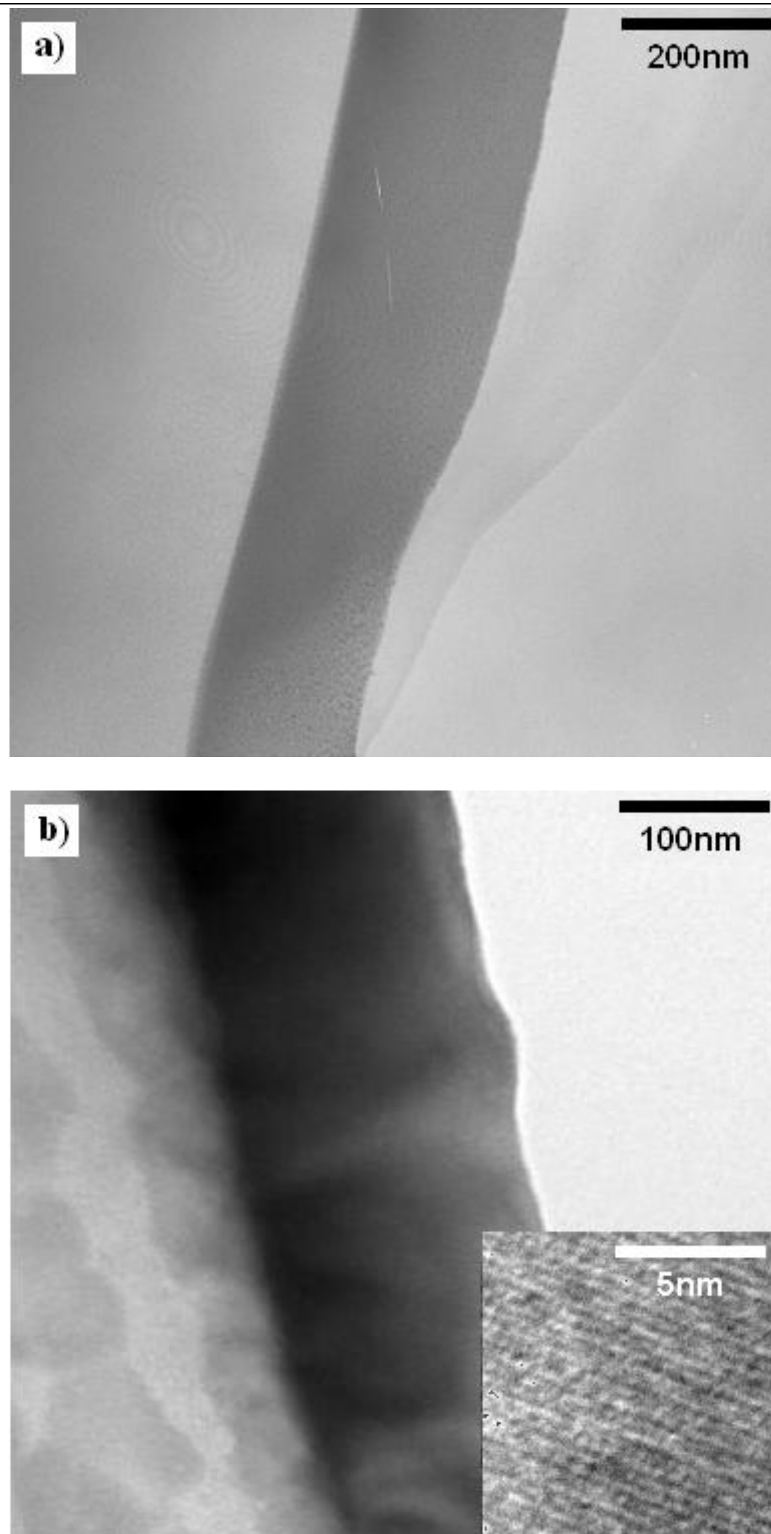

Figure 3-4: Cross-sectional TEM Images of the deposited films. (a) Magnetron sputtered sample (b) Cathodic arc sample. Insert: high resolution image of cathodic arc sample.

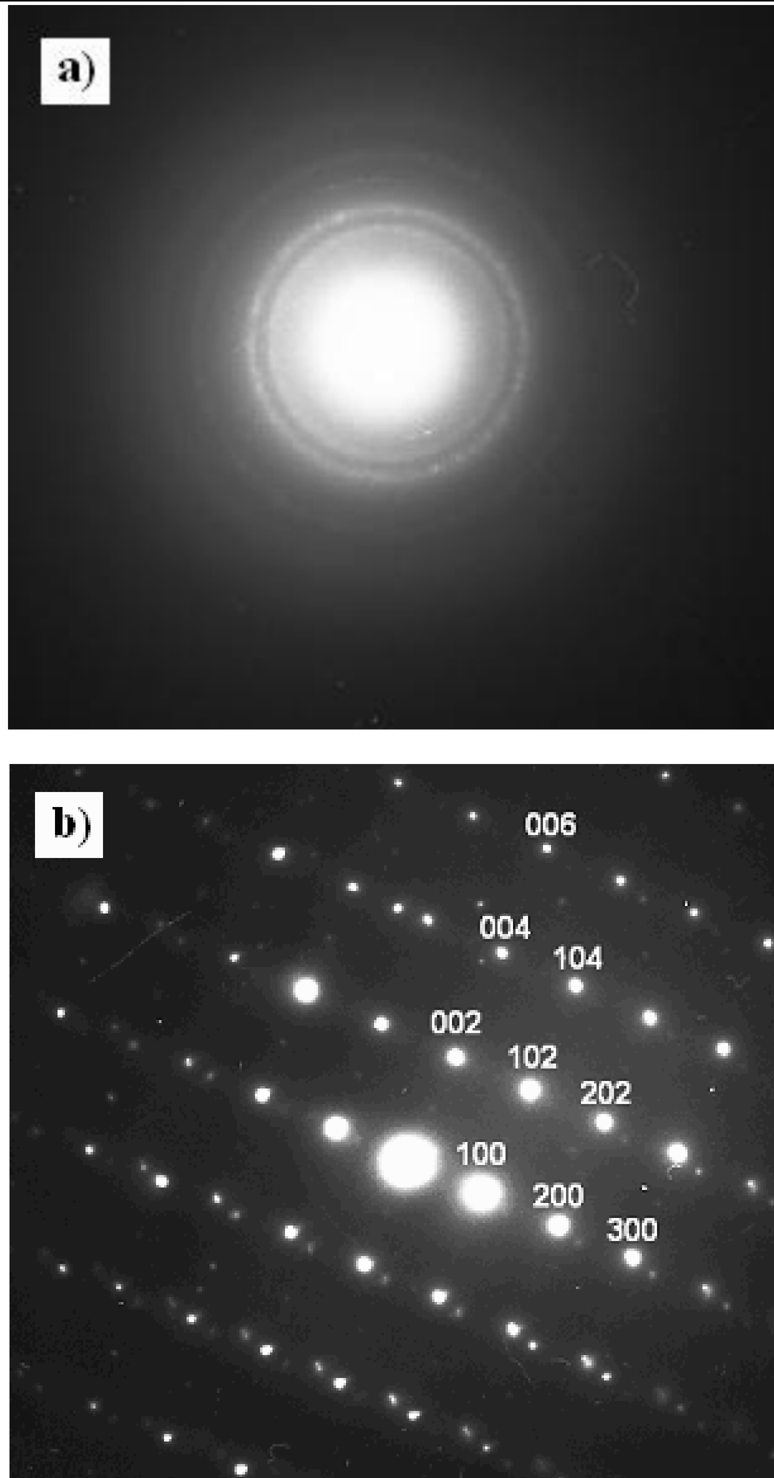

Figure 3-5: Selected area diffraction patterns of the (a) magnetron sputtered [33] and (b) cathodic arc films shown in figure 3-4. The diffraction pattern in (b) has been indexed to α-WO_3.

3.3.4 Electron energy loss spectroscopy (EELS)

Figure 3-6 shows the oxygen K-edge measured using EELS from the pulsed magnetron and pulsed cathodic arc deposited coatings. The main features have been labelled A-H for clarity. Due to experimental error in the offset associated with EELS data, the spectra have been aligned such that peak 'A' has been fixed to 530.7 eV, the value measured by Purans et al [24] in the work performed previously using XAS of a magnetron sputtered γ-WO_3 film.

The features in the EELS spectrum of the pulsed magnetron sample are broad, probably the result of a high level of disorder within the film. In contrast, the fine structure of the pulsed cathodic arc sample is more distinct and has well defined features. It also includes an additional peak located at 551.7 eV (labelled "G" in Figure 3-7) which has an intensity dependent on the angle between W-O-W atoms [24]. The large peak intensity observed here indicates that there is a near linear atomic chain, an indication of orthogonal axes and further evidence that the tetragonal α-WO_3 phase is present.

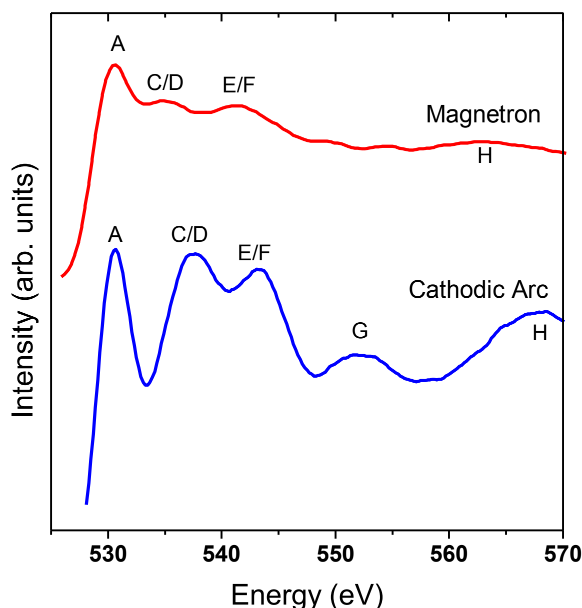

Figure 3-6: Oxygen K-edge EELS spectra for the 2 experimental samples where (a) refers to the film deposited by magnetron sputtering and (b) refers to the cathodic arc deposited film. The main features have been labelled for clarity.

3.3.4 Local density of states (LDOS)

The oxygen local s and p projected density of states (DOS) calculated using FEFF8 for the α and γ phases are shown in figure 3-7. Differences in the DOS are clearly seen between these phases, particularly in the pDOS above the Fermi energy which is expected to be reflected in the NES of the corresponding oxygen K-edge.

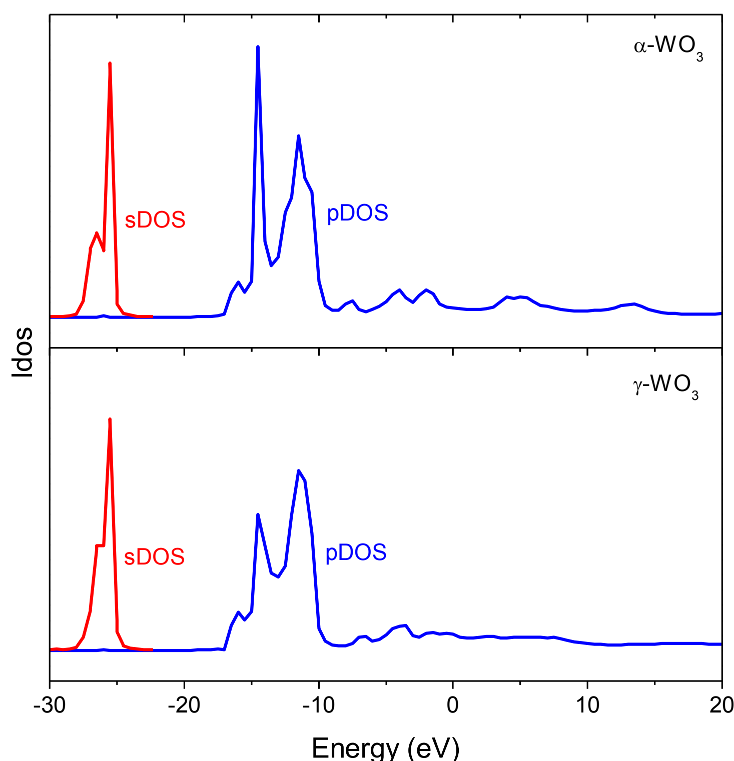

Figure 3-7: The local s and p projected density of states for oxygen calculated using FEFF8 for the α and γ phases of WO_3.

3.3.5 Energy-loss near edge structure (ELNES)

The real space approach employed in FEFF8 allows the variation in the near edge structure as a function of cluster size around the absorbing atom to be explored. Using this information the relative intensities of the features in the near edge structure were studied to gain an understanding of the physical structure of the films. Figure 3-8 shows the variation of NES (left) on the oxygen K-edge calculated using FEFF8 as the cluster size (right) is increased for the α-WO_3 phase. The basic edge shape is formed for a small cluster consisting of an oxygen

atom bonded to its two adjacent tungsten atoms. The dominant first peak (A) appears when the absorbing oxygen atom is surrounded by its eight nearest oxygen atoms, four from each adjoining octahedral unit. The next significant change in the oxygen K-edges occurs for a cluster size of twelve atoms, when the two adjoining octahedral units are completed and peaks C/D and E/F form.

In a study by Purans [24] the electronic origin of these peaks has been deduced. Peaks A and B arise from empty oxygen 2p states which are dependent on the occupancy of the conduction band and the degree of covalency of the atom. The more covalent the bonding in the material, the more intense these peaks will be. Peaks C and D arise from the hybridisation of the 5d tungsten electrons and the 2p oxygen electrons and is strongly influenced by the distortion in the WO_6 octahedra. The intensity of these peaks is a measure of the symmetry of these octahedra. Peaks E and F are attributed to the tungsten 6sp to oxygen 2p hybridisation in a similar manner to peaks C and D. The intensity of peak G is dependent on the W-O-W angle, in which higher intensities arise from near linear chains of atoms. This peak is not visible in amorphous (highly disordered) materials. Peak H is attributed to single scattering processes with the nearest neighbour oxygen atoms. This can be seen in figure 3-8, in which this peak appears for cluster sizes of 10 atoms when the nearest neighbour oxygen atoms are added to the cluster.

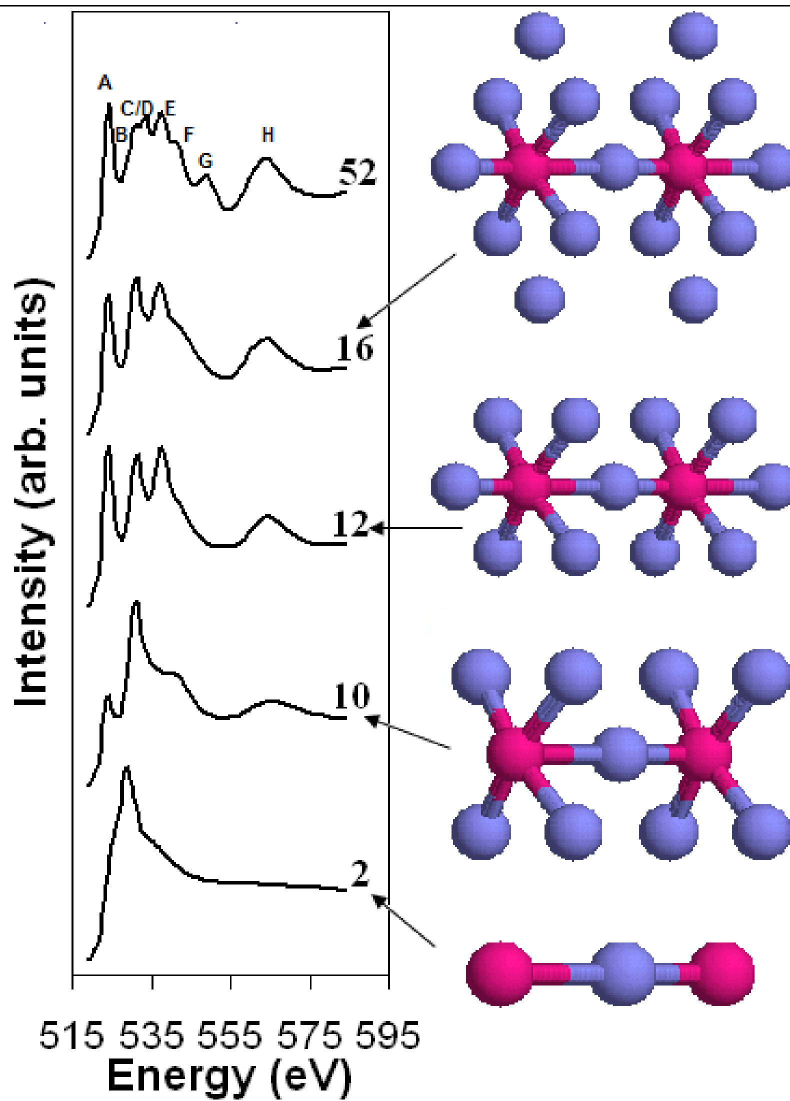

Figure 3-8: Calculated oxygen K-edge's for the α-WO_3 phase for various numbers of atoms surrounding the absorbing oxygen (left). A graphical representation of the clusters is also shown (right), with blue atoms and pink atoms representing oxygen and tungsten atoms respectively.

Figure 3-9 shows a comparison of the oxygen K-edges for the various phases of WO_3 calculated using FEFF8 with 0.5 eV of broadening added to the calculation. In order to compare with experiment, peak A has been aligned to 530.7 eV as measured previously for γ-WO_3 [24]. Clearly, each phase has a unique NES reflecting their different atomic arrangement.

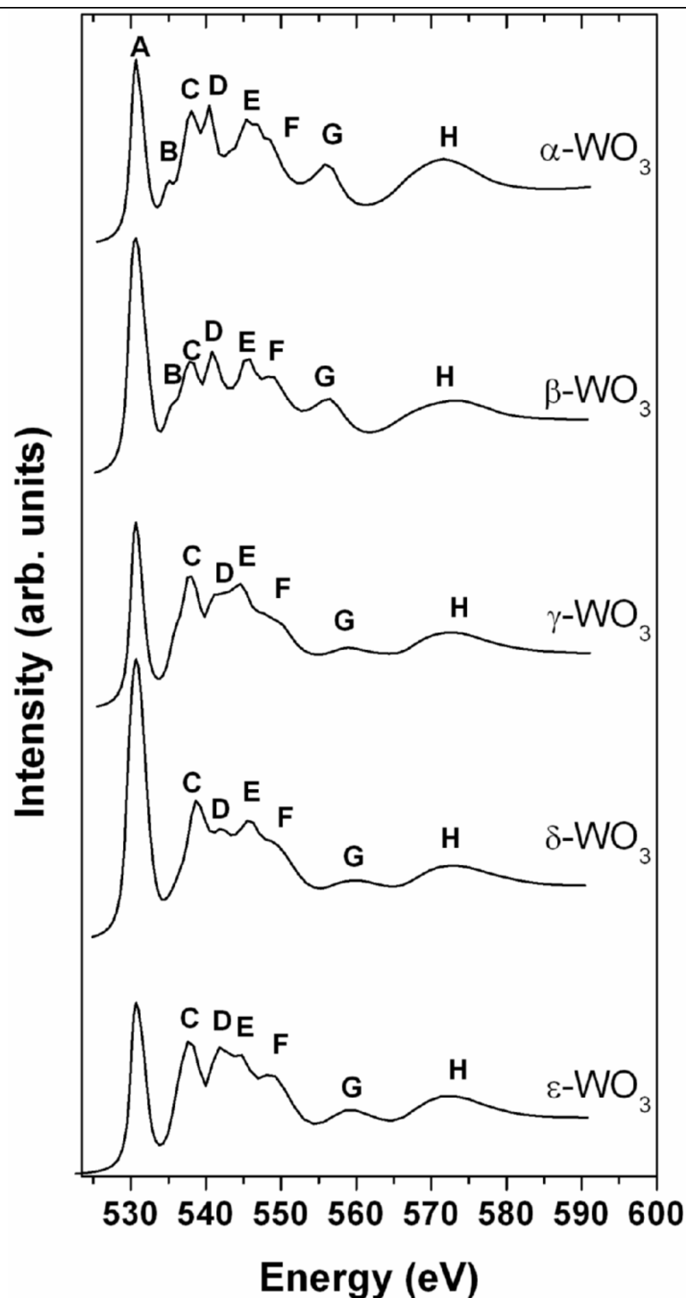

Figure 3-9: The calculated oxygen K-edge NES for the known phases of WO_3. The main features have been labelled and their energies have been listed in table 3-2.

Calculations of the oxygen K-edges were also performed using the WIEN2k code [38] on the tetragonal α-WO_3 phase and the monoclinic γ-WO_3 phase. Figure 3-10 compares the oxygen K-edge of γ-WO_3 calculated using FEFF8 and that obtained using WIEN2k. Also shown is the oxygen K-edge obtained using XAS for a sputtered WO_3 film which was identified as being γ-WO_3 [24]. Overall, the results are similar with the main features reproduced using both

methods. The FEFF8 calculation does include doublet at approximately 540 eV which is not reproduced in WIEN2k calculation.

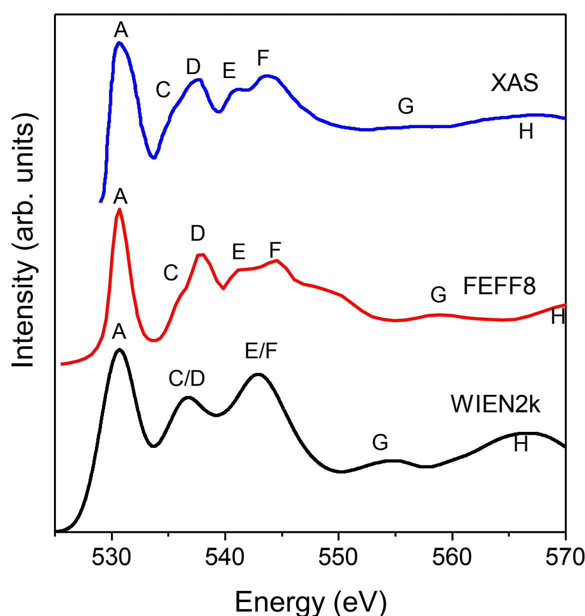

Figure 3-10: Comparison of the oxygen K-edge of calculated using FEFF8 and WIEN2k. Note that the energy scale is relative to the Fermi energy. These are compared to γ-WO_3 obtained using XAS [24].

Figure 3-11 compares the EELS spectrum from the cathodic arc deposited sample with that calculated using FEFF8 and WIEN2k for α-WO_3 (reproduced from Figure 3-6). There is good agreement between theory and experiment. As with the case of γ-WO_3, WIEN2k does not reproduce the relative intensities of peaks C/D and E/F, while the peak positions of peaks B to H calculated using FEFF8 are higher than that observed experimentally by approximately 3-4 eV. This discrepancy may be the result of errors in the calculation of the atomic potential in the FEFF8 code, the accuracy of which is critical for reproducing the position of features close to the threshold [39]. This is confirmed by the full-potential calculations of WIEN2k, which overall correctly predicts the energy for the main features. The good match between the calculations of a-WO3 and the film prepared by cathodic arc is in agreement with the diffraction analysis which showed that α-WO_3 was present.

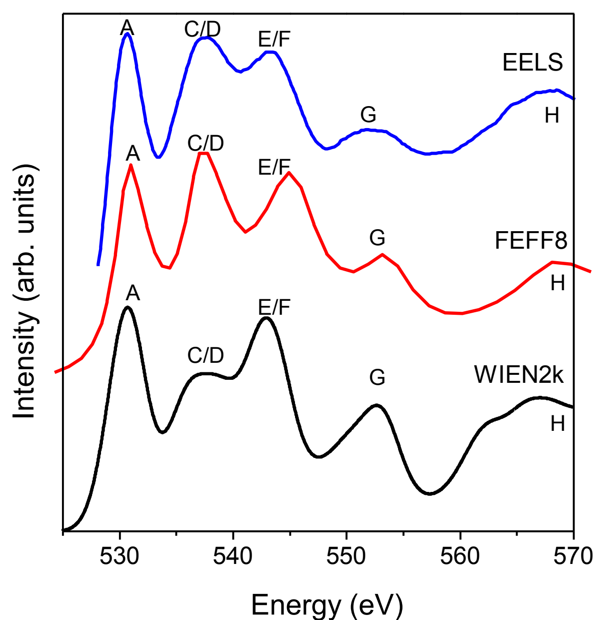

Figure 3-11: Comparison of the oxygen K-edge for α-WO_3 calculated using FEFF8 and WIEN2k. These calculations are compared to the experimental data from the cathodic arc deposited tungeten oxide film in which diffraction analysis showed that the α-WO_3 was present.

Table 3-2 shows the peak positions for the WO_3 samples. Each spectrum has been shifted so that they align with the XAS worked performed by Purans [24]. Listed within the table are the two experimental samples from this work (magnetron and pulsed arc), the γ-WO_3 sample analysed by Purans et al [24], the 5 phases calculated using FEFF8 and the two phases calculated by WIEN2k. Where possible peak overlap is observed, a single value is placed between the two peaks. The calculations show a shift of up to 4 eV in peak positions is expected depending on the phase, despite the fact that they all have a similar microstructure. These results show that ELNES and XANES can be used as a sensitive measure of which WO_3 phase is present in a sample.

Table 3-2: The position (eV) of the main features in the experimental and calculated oxygen K-edges. Note that the experimental and calculated values have been shifted so that the first NES peak (A) aligns with previous XAS measurements of γ-WO_3 [24].

<table>
<tr><th>Sample/Phase</th><th>A</th><th>B</th><th>C</th><th>D</th><th>E</th><th>F</th><th>G</th><th>H</th></tr>
<tr><td>Magnetron Sputtered</td><td>530.7</td><td>-</td><td colspan="2">535.5</td><td colspan="2">541.8</td><td>-</td><td>563.4</td></tr>
<tr><td>Cathodic Arc</td><td>530.7</td><td>-</td><td colspan="2">537.5</td><td colspan="2">543.1</td><td>551.7</td><td>568.3</td></tr>
<tr><td>γ - WO_3 [24]</td><td>530.7</td><td>531.7</td><td>535.4</td><td>537.6</td><td>541.1</td><td>543.8</td><td>556.1</td><td>567.2</td></tr>
<tr><td>α - FEFF8</td><td>530.7</td><td>535</td><td>537.9</td><td>540.3</td><td>545.3</td><td>548.2</td><td>555.8</td><td>571.3</td></tr>
<tr><td>β - FEFF8</td><td>530.7</td><td>535.9</td><td>538.1</td><td>540.9</td><td>545.6</td><td>548.7</td><td>556.2</td><td>573.2</td></tr>
<tr><td>γ - FEFF8</td><td>530.7</td><td>535.8</td><td>537.6</td><td>541</td><td>544.3</td><td>549.9</td><td>558.7</td><td>572.3</td></tr>
<tr><td>δ - FEFF8</td><td>530.7</td><td>-</td><td>538.6</td><td>542</td><td>545.7</td><td>548.4</td><td>559.6</td><td>572.8</td></tr>
<tr><td>ε - FEFF8</td><td>530.7</td><td>-</td><td>537.5</td><td>541.7</td><td>544.3</td><td>548.6</td><td>558.8</td><td>572.2</td></tr>
<tr><td>α - WIEN2k</td><td>530.7</td><td>-</td><td colspan="2">537.7</td><td colspan="2">543</td><td>552.7</td><td>567.8</td></tr>
<tr><td>γ - WIEN2k</td><td>530.7</td><td>-</td><td colspan="2">536.8</td><td colspan="2">542.9</td><td>554.8</td><td>566.7</td></tr>
</table>

3.4 Conclusions

The structure of tungsten oxide thin films was found to depend on the fabrication method. The pulsed cathodic arc deposition produced a WO_3 film with a well-ordered tetragonal structure. This phase usually forms at approximately 740 ºC in the bulk, however, the energetic flux associated with the pulsed cathodic arc has made it possible to access this phase in thin film form. In contrast to this, magnetron sputtering produced a highly disordered film which, due to the limited energy resolution of EELS, was difficult to assign to a particular phase. It was also shown that the FEFF8 code is able to distinguish subtle differences in the oxygen K-edge for various phases of WO_3. The calculated oxygen K-edge using both FEFF8 and WIEN2k for the γ-WO_3 phase was found to match well with previous published experiment XAS results. There was also a good match between the calculated oxygen K-edge for the α-WO_3 phase and that found using EELS for the cathodic deposited film.

3.5 Bibliography

1. Azens and Granqvist, *Electrochromic smart windows: energy efficiency and device aspects.* Journal of Solid State Electrochemistry, 2003. **7**(2): p. 64-68.
2. Su, L., J. Fang, Z. Xiao, and Z. Lu, *An all-solid-state electrochromic display device of prussian blue and WO3 particulate film with a PMMA gel electrolyte.* Thin Solid Films, 1997. **306**(1): p. 133-136.
3. Delichère, P., P. Falaras, and A. Hugot-Le Goff, *WO3 anodic films in organic medium for electrochromic display devices.* Solar Energy Materials, 1989. **19**(3-5): p. 323-333.
4. Cui, H.N., M.F. Costa, V. Teixeira, I. Porqueras, and E. Bertran, *Electrochromic coatings for smart windows.* Surface Science
Proceedings of the 7th International Conference on Nanometer-Scale Science and Technology and the 21st European Conference on Surface Science, 2003. **532-535**: p. 1127-1131.
5. Cui, H.N., M.F. Costa, V. Teixeira, I. Porqueras, and E. Bertran, *Electrochromic coatings for smart windows.* Surface Science Proceedings of the 7th International Conference on Nanometer-Scale Science and Technology and the 21st European Conference on Surface Science, 2003. **532-535**: p. 1127-1131.
6. Akl, A.A., H. Kamal, and K. Abdel-Hady, *Characterization of tungsten oxide films of different crystallinity prepared by RF sputtering.* Physica B: Condensed Matter, 2003. **325**: p. 65-75.
7. Granquist, C.G., *Handbook of Inorganic Electrochromic Materials*. 1995, Amsterdam: Elsevier.
8. Labidi, A., C. Jacolin, M. Bendahan, A. Abdelghani, J. Guérin, K. Aguir, and M. Maaref, *Impedance spectroscopy on WO_3 gas sensor.* Sensors and Actuators B: Chemical, 2005. **106**(2): p. 713-718.
9. Deng, Z., Y. Gong, Y. Luo, and Y. Tian, *WO_3 nanostructures facilitate electron transfer of enzyme: Application to detection of H_2O_2 with high selectivity.* Biosensors and Bioelectronics, 2009. **24**(8): p. 2465-2469.
10. Yong, F., Z. Lian, D. Shejun, W. Jinrong, Z. Pingxiang, S. Lei, and Z. Yuheng, *Superconductivity in quenched YBCO---WO_3 system.* Physica C: Superconductivity, 1994. **235-240**(Part 1): p. 405-406.
11. Yuan, H., D.E. Laughlin, X. Zhu, and B. Lu, *Ru + oxide interlayer for perpendicular magnetic recording media.* Journal of Applied Physics, 2008. **103**(7): p. 07F513.
12. Bussjager, R., J.M. Osman, E. Voss, and J. Chaiken. *Tungsten oxide based media for optical data storage and switching applications*. in *Aerospace Conference, 1999. Proceedings. 1999 IEEE*. 1999.
13. Aird, A., M.C. Domeneghetti, F. Mazzi, V. Tazzoli, and E.K.H. Salje, *Sheet superconductivity in : crystal structure of the tetragonal matrix.* Journal of Physics: Condensed Matter, 1998. **10**(33): p. L569-L574.
14. Salje, E. and K. Viswanathan, *Physical properties and phase transitions in WO_3.* Acta Crystallographica Section A, 1975. **31**: p. 360-363.
15. WebElements, *Compounds of Tungsten.* http://www.webelements.com/webelements/compounds/text/W/O3W1-1314358.html.
16. Salje, E.K.H., S. Rehmann, F. Pobell, D. Morris, K.S. Knight, T. Herrmannsdorfer, and M.T. Dove, *Crystal structure and paramagnetic behaviour of ε-WO_{3-x}.* Journal of Physics: Condensed Matter, 1997. **9**(31): p. 6563-6577.
17. Locherer, K.R., I.P. Swainson, and E.K.H. Salje, *Transition to a new tetragonal phase of WO_3: crystal structure and distortion parameters.* Journal of Physics: Condensed Matter, 1999. **11**(21): p. 4143-4156.
18. Salje, E., *The orthorhombic phase of WO_3.* Acta Crystallographica Section B, 1977. **33**: p. 574-577.
19. Woodward, P.M., A.W. Sleight, and T. Vogt, *Structure refinement of triclinic tungsten trioxide.* Journal of Physics and Chemistry of Solids, 1995. **56**(10): p. 1305-1315.

20. Gillet, M., A. Al-Mohammad, and C. Lemire, *Microstructural analysis of WO_3 thin films on alumina substrates.* Thin Solid Films, 2002. **410**(1-2): p. 194-199.
21. Shigesato, Y., A. Murayama, T. Kamimori, and K. Matsuhiro, *Characterization of evaporated amorphous WO_3 films by Raman and FTIR spectroscopies.* Applied Surface Science, 1988. **33-34**: p. 804-811.
22. Rougier, A., F. Portemer, A. Quede, and M. El Marssi, *Characterization of pulsed laser deposited WO_3 thin films for electrochromic devices.* Applied Surface Science, 1999. **153**(1): p. 1-9.
23. Tay, B.K., Z.W. Zhao, and D.H.C. Chua, *Review of metal oxide films deposited by filtered cathodic vacuum arc technique.* Materials Science and Engineering: R: Reports, 2006. **52**(1-3): p. 1-48.
24. Purans, J., A. Kuzmin, P. Parent, and C. Laffon, *X-ray absorption study of the electronic structure of tungsten and molybdenum oxides on the O K-edge.* Electrochimica Acta, 2001. **46**(13-14): p. 1973-1976.
25. Deb, S.K., *Opportunities and challenges in science and technology of WO_3 for electrochromic and related applications.* Solar Energy Materials and Solar Cells, 2008. **92**(2): p. 245-258.
26. Mattox, D.M., *Handbook of physical vapour deposition (PVD) processing*. 1998: Noyes Publications.
27. Mráz, S. and J.M. Schneider, *Energy distribution of O- ions during reactive magnetron sputtering.* Applied Physics Letters, 2006. **89**(5): p. 051502
28. Anders, A., *Ion charge state distributions of vacuum arc plasmas: The origin of species.* Physical Review E, 1997. **55**(1): p. 969.
29. Anders, A. and G.Y. Yushkov, *Ion flux from vacuum arc cathode spots in the absence and presence of a magnetic field.* Journal of Applied Physics, 2002. **91**(8): p. 4824-4832.
30. Oks, E.M., E.M. Oks, A. Anders, I.G. Brown, M.R.A.D.M.R. Dickinson, and R.A.A.M.R.A. MacGill, *Ion charge state distributions in high current vacuum arc plasmas in a magnetic field.* Plasma Science, IEEE Transactions on, 1996. **24**(3): p. 1174-1183.
31. Bilek, M.M.M., M.M.M. Bilek, R.N. Tarrant, D.R. McKenzie, S.H.N.A.L.S.H.N. Lim, and D.G.A.M.D.G. McCulloch, *Control of stress and microstructure in cathodic arc deposited films.* Plasma Science, IEEE Transactions on, 2003. **31**(5): p. 939-944.
32. Brown, I.G., *Cathodic arc deposition of films.* Annual Review of Materials Science, 1998. **28**(1): p. 243-269.
33. Field, M., *The Characterisation of Tungsten Oxide Thin Films.* RMIT University, Melbourne, 2006. **Honours Thesis**.
34. MacGill, R.A., M.R. Dickinson, A. Anders, O.R. Monteiro, and I.G. Brown. *Streaming metal plasma generation by vacuum arc plasma guns*. in *Proceedings of the 7th international conference on ion sources*. 1998. Shirahama, Wakayama (Japan): AIP.
35. Anders, A. and G.Y. Yushkov, *Low-energy linear oxygen plasma source.* Review of Scientific Instruments, 2007. **78**(4): p. 043304-7.
36. Moreno, M.S., K. Jorissen, and J.J. Rehr, *Practical aspects of electron energy-loss spectroscopy (EELS) calculations using FEFF8.* Micron, 2007. **38**(1): p. 1-11.
37. Marszalek, K., *Magnetron-sputtered WO_3 films for electrochromic devices.* Thin Solid Films, 1989. **175**: p. 227-233.
38. Hebert, C., *Practical aspects of running the WIEN2k code for electron spectroscopy.* Micron, 2007. **38**(1): p. 12-28.
39. Modrow, H., S. Bucher, J.J. Rehr, and A.L. Ankudinov, *Calculation and interpretation of K-shell x-ray absorption near-edge structure of transition metal oxides.* Physical Review B, 2003. **67**(3): p. 035123.

Chapter 4

Microstructural analysis of zinc oxide films doped with aluminium for solar cell research

In this chapter, the structure and properties of aluminium zinc oxide (AZO) films are investigated. Films are deposited using high power impulse magnetron sputtering (HIPIMS), pulsed cathodic arc and magnetron sputtering. So that a direct comparison can be made between these techniques, deposition parameters such as partial pressures and substrate temperature were kept similar. Optical transmittance measurements were performed films as well as 4 point probe and Hall measurements in order to obtain the electrical properties such as the electron concentration, mobility and the resistivity. The microstructure, stoichiometry and electronic structure of the films was determined using x-ray diffraction (XRD), x-ray photoelectron spectroscopy (XPS), transmission electron microscopy (TEM), electron diffraction and x-ray absorption spectroscopy (XAS).

4.1 Introduction/Background theory

4.1.1 Doped zinc oxide in industry

As discussed in chapter 1, ZnO is a material of much interest to the scientific community due to its low cost, ease of synthesis and the desirable properties that can be attained when the material is doped. Aluminium doped zinc oxide (ZnO:Al or AZO) and gallium doped zinc oxide (ZnO:Ga or GZO) are two materials that are a possible replacement for tin doped indium oxide (In_2O_3:Sn or ITO) [1], which due to limited reserves of indium, alternate materials need to be found. ITO is currently the most widely used transparent conductive oxide due to its combination of optical transparency and electrical conductivity. When used in the form of a thin film, ITO has many uses, such as liquid crystal displays, touch panels, light emitting diodes, solar cells and anti-static coatings.

4.1.2 Crystal structure and doping

Zinc oxide (ZnO) is a material which has been studied for many decades [2-8] and thus the crystal structure and the lattice parameters of this material are well known. ZnO can appear as one of 3 phases, wurtzite (hexagonal) [6], zinc-blende (cubic) [9] or rocksalt (cubic with a NaCl-like structure) [6]. The wurtzite phase is most thermodynamically stable at ambient conditions [10] and is the phase which is most commonly observed. The zinc-blende phase can be grown by depositing ZnO onto a substrate which has a cubic structure [10]. The rocksalt phase can be grown when depositing the ZnO film at high pressures [10]. Figure 4-1 (adapted from the ZnO review paper by Ozgur et al [10]) shows a ball and stick representation of the three ZnO crystal phases. Table 4-1 shows the space groups for each of the structures as well as their lattice parameters. These were determined using transmission electron microscopy (TEM) [9], x-ray diffraction (XRD) [6,9] and reflection high energy electron diffraction (RHEED) [9]. In the work presented in this thesis, ZnO-like films were deposited onto amorphous substrates in low pressure environments, so that the wurtzite phase is expected.

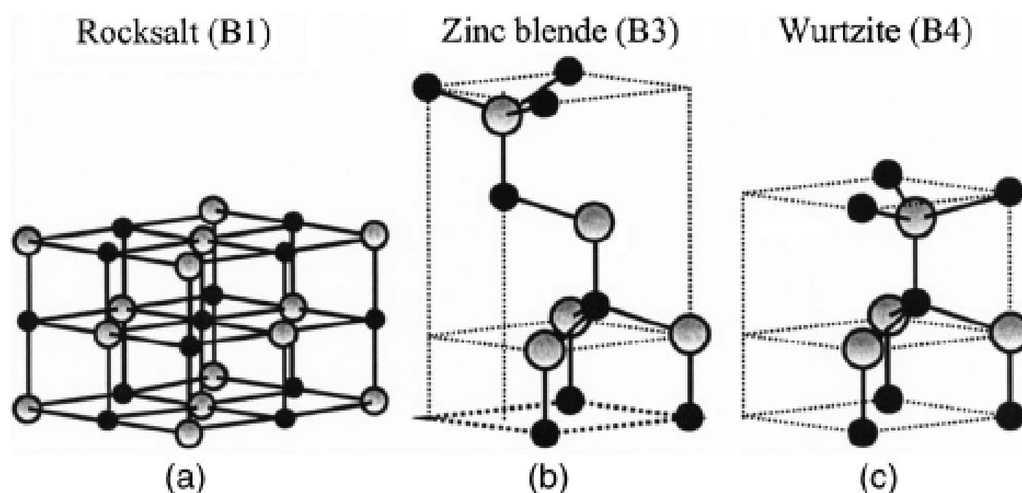

Figure 4-1: Representation of the ZnO crystal structures. Figure was adapted from the ZnO review paper written by Ozgur et al [10]. The shaded grey spheres represent the Zn atoms and the black spheres represent the O atoms.

Table 4-1: Crystallographic details of the main ZnO crystal structures.

Phase	Spacegroup	Lattice Parameters	Comments
Rocksalt	Fm3m	a=4.271	Determined using XRD [6]
Zinc blend	$F\bar{4}3m$	a=4.463	Measured with RHEED, XRD and TEM [9]
Wurtzite	$P6_3mc$	a=3.2496 c=5.2042	Determined using XRD [6]

Wurtzite ZnO is a naturally occurring n-type semiconductor due to the oxygen vacancies and zinc interstitials that are inherent in its sub-stoichiometric structure. It has been found that p-type doping of ZnO is very difficult. Doping using group I elements (lithium, sodium or potassium) is inhibited by the dopants forming interstitial sites instead of substituting with zinc sites, and thus acting as donors [11]. Group V elements (nitrogen, phosphorus and arsenic) could be used in place of the oxygen sites, but have been shown not to work as well as p-dopants as doping with group I elements [12].

In contrast to this, n-type doping has been found to be both simple and effective. Group-III elements such as aluminium, gallium and indium can be used as n-type dopants as

substitutional elements for the zinc sites [13-15]. Group-VII elements such as chlorine or iodine can be used for n-type doping as a substitute for the oxygen position [4, 16]. Of the many possible n-type dopants available, using aluminium as a dopant in ZnO is a good choice. It has not only shown promising opto-electrical properties [13, 17-21], but also is cost effective for extraction and manufacturing, non-toxic and can be exploited as a natural impurity in zinc metal.

4.1.3 AZO coatings

Growth of AZO films has been performed by many research groups to attain reproducible TCO's with the potential to replace ITO [7, 22, 23]. AZO coatings often have a polycrystalline microstructure with a preferred c-axis crystallographic orientation with respect to the substrate. For example, Lim et al [18] performed XRD on AZO films prepared using DC magnetron sputtering and found only the wurtzite (002) peak (c-axis alignment) perpendicular to the substrate was present. However, the author didn't specify the phase of the ZnO. Also in this study, the electrical and optical properties were determined using 4-point probe and optical transmittance respectively. It was found that the films had a good optical transmittance of approximately 91.5%, but had a resistivity of 4.3×10^{-4} Ω.cm, an order of magnitude greater than that of ITO films.

Lu et al [20] deposited a variety of films also using dc reactive magnetron sputtering with increasing aluminium content within the target material. It was found that aluminium concentrations greater than 10% affected the microstructures of the films greatly. Up to 10% Al concentration the only significant XRD peak was the wurtzite(002) located at $2\theta=34^{\circ}$, indicating that strong preferred orientation is present in which the c-axis is aligned perpendicular to the substrate. As the concentration of aluminium is increased above 10%, the microstructure of the films change. At 15% and 20% aluminium concentrations the XRD shows additional wurtzite(100) and wurtzite(101) peaks respectively. For Al concentrations >30% the

ZnO(002) peak disappears almost entirely and a Al-metal(113) peak located at approximately $2\theta=44^{\circ}$ appears, indicating a two phase system. In this work, electrical characterisation was also carried out, in which it was found that the minimum resistivity of the AZO films occurs when an aluminium concentration of 4% is present. For concentrations either side of this, an increase in the resistivity was observed.

In a paper by Lin et al [19], heavily Al doped (>10%) AZO films were deposited by simultaneous dc and rf magnetron sputtering. The effect of substrate temperature increase from room temperature up to 200ºC was investigated. It was found using XRD that the ZnO crystals growing in the <001>, <102> and <103> directions perpendicular to the substrate were present in the film. No appreciable shifting in the wurtzite(002) XRD peak was observed, which indicates an absence of stress generated from the inclusion of Al dopants into the ZnO lattice. This suggests that the majority of the Al content was located outside of the ZnO (002) crystallites and was instead forming other Zn-Al phases. This crystallinity was also confirmed using selected area diffraction in the TEM.

In a paper by Schuler and Aegerter [21] AZO films were deposited using the sol gel dip coating process where the film thickness was controlled by depositing multiple AZO layers on top one another. The effect of the number of layers on the microstructure, resistivity and optical transmittance was studied. Measurements of the resistivity were performed and found to be in the order of 5×10^{-3} Ω.cm, optical measurements yielded approximately 80% transmittance in the visible region of the spectrum. TEM imaging was also performed on the samples with differing number of AZO layers and yielded interesting results. For the films deposited by this method, columnar growth did not occur with the single layer samples, but instead the films grew as spherical particles 15-25 nm in diameter spread across the substrate. Increase in the number of layers increased the particle size until eventually at 5-10 layers columnar growth was present. Thick single layer coatings deposited using this method also appeared as particles, with

elongation of the particles in the <001> direction occurring with multilayer films with thick layers. This paper shows that the thickness of the film has a dramatic effect on the microstructure of the films, with spherical particles and columnar particles both observed and shown to yield different physical properties.

Xu et al [24] deposited AZO films at low temperatures by spray pyrolysis. Interestingly the films had a strong preferred orientation with the <101> direction perpendicular to the substrate and formed lenticular shaped wurtzite crystals. This is quite unlike most papers (see above) in which growth usually occurs with the c-axis perpendicular to the substrate. It was found that for the lowest sheet resistance, an atomic percentage of 4% aluminium was required. This is the same as what Lu et al [20] found. However in this work, even though the transmission measurements in the visible region were acceptable (~80% at 550 nm), the resistivities were quite high. Using a doping concentration of 4% aluminium and post annealing of 550ºC, the best achievable resistivity was 1×10^{-2} Ω.cm. In contrast to this, the films grown by magnetron sputtering by Lu et al had much better resistivities (10^{-4} Ω.cm), high transmittance (~90%) and had much stronger preferred orientation with the wurtzite c-axis perpendicular to the substrate and increased crystal size and quality [20].

4.1.4 Presence of negative ions in magnetron sputtering techniques

During reactive deposition using magnetron sputtering and HIPIMS, there is a flux of O^- ions which are generated at the magnetrons and directed towards the deposited film during deposition along the magnetic field lines. In an experiment by Mráz and Schneider [25] the energy distribution functions within the chamber during magnetron deposition was determined using a mass energy analyser and several ion populations were discovered. There was a low energy ion population which was attributed to dissociative electron attachment of oxygen, in which the newly formed O^- is accelerated towards the substrate by a small fraction of the magnetron potential. The high energy species are formed from oxygen being sputtered from the target material as O^- and being accelerated towards the substrate and reaching it with an energy

given by the target potential. The medium energy species were found to have energy half that of the target potential and high energy species. This population was attributed to O_2^- ions being accelerated from the target material at full potential, and then dissociating to O^- and O with the energy divided evenly between the species. Hence the O^- is detected as having half of the energy of the target potential. The energy distribution function was also measured for the possibility of O+ ions within the beam. It was found that this species was present in the beam, but only as a low energy population with a small intensity. Due to this, it was suggested that this species does not play a key role in the structure evolution of metal oxide thin films.

This oxygen ion damage effect has been seen in doped zinc oxide films. Minami et al [7] deposited zinc oxide films doped with Sc and Y using magnetron sputtering. The resistivity, Hall mobility and carrier concentration of the films was analysed across the surface of the sample and it was found that these properties were non-uniform. Across the substrate surface over the magnetron racetrack there were inferior electrical properties such as high resistivity, low mobility and low carrier concentration.

The work presented in this chapter uses the same pulsed cathodic arc setup employed by Anders et al [17]. The substrates were heated to 200 ºC during deposition (as it was found to result in the best resistivity by Anders [17]) and a Zn/Al cathode with 4 at% Al was used. A more rigorous study of the microstructure is performed by employing XRD, XPS and XAS at the Australian Synchrotron to directly probe the microstructure electronic structure. It has been shown that different microstructures can be achieved depending on the deposition technique, with spherically shaped particles [21], lenticular shaped particles [24] and columnar growth with c-axis perpendicular to the substrate [18, 20, 21] all being reported. The results presented in this chapter is a comparison of AZO films prepared using the pulsed arc deposition system to two other techniques: magnetron sputtering and HIPIMS. By using the same cathode material for all three deposition methods, a direct comparison between the techniques is presented. Also presented in this chapter is an investigation of the effect of oxygen ion damage to the films

during the deposition of magnetron sputtered and HIPIMS samples. In particular a novel magnetic filter is used in an attempt to remove O^- ion damage.

4.2. Experimental Methods

In this work, four different deposition techniques are used to grow AZO films. Pulsed cathodic arc deposition grows coatings using a filtered plasma of high energy ions (section 2.1.3), conventional magnetron sputtering using low energy neutrals (section 2.1.4) and HIPIMS uses an unfiltered plasma of high energy ions (section 2.1.5). Like the work performed on tungsten oxide (section 3.1.3), the change in incident energy of the depositing particles is known to have an important influence on the microstructure of the films [26, 27] which may lead to enhanced optical or electrical performance. A negative ion filter is introduced into the HIPIMS system (section 4.2.3) to create a novel deposition technique which may prevent the oxygen ion damage outlined in section 4.1.4. All of the films were deposited onto both glass microscope slides and microscope coverslips. A pen mark (<1 mm^2 in area) was placed into the corner of the substrate before deposition, and was later wiped off so that step height analysis using a profilometer could be performed on the samples to determine the film thickness. Details of the experimental parameters used in each of these methods are presented below.

4.2.1 Pulsed cathodic arc

Pulsed cathodic arc was used to deposit films with a variety of thicknesses by varying the total number of pulses to the cathode. The cathode target used was zinc doped with 4% aluminium. The zinc-aluminum plasma stream passed a 90°-bent open filter to remove most of the macroparticles. Pure oxygen gas was injected into the chamber using a mass flow controller (MKS Instruments) and was monitored by a differentially pumped quadrupole mass spectrometer (model RGA100 by SRS). Arc pulses of 1 ms duration and amplitude of 780 A were delivered with a repetition rate of usually 3 to 4 pulses per second by a pulse-forming

network [28]. The arc current was measured using a 0.01 V/A Pearson coil and recorded on a digital oscilloscope (Tektronix). The substrates were mounted to a rotating sample holder and were heated to a temperature of 200ºC using a 4-lamp radiative heater (see figure 4-2). The temperature of the substrate was monitored using an infrared Raytek® temperature sensor through a quartz window. A systematic error of approximately 50 ºC was found due to reflection from the substrates of radiation from the heater, and this value has been corrected accordingly. With the heater element to the side of where the deposition is taking place, it was found that during a single deposition run the samples undergo a cycle of deposition (at 200ºC) and *in situ* annealing (~250ºC). This configuration is shown in figure 4-2.

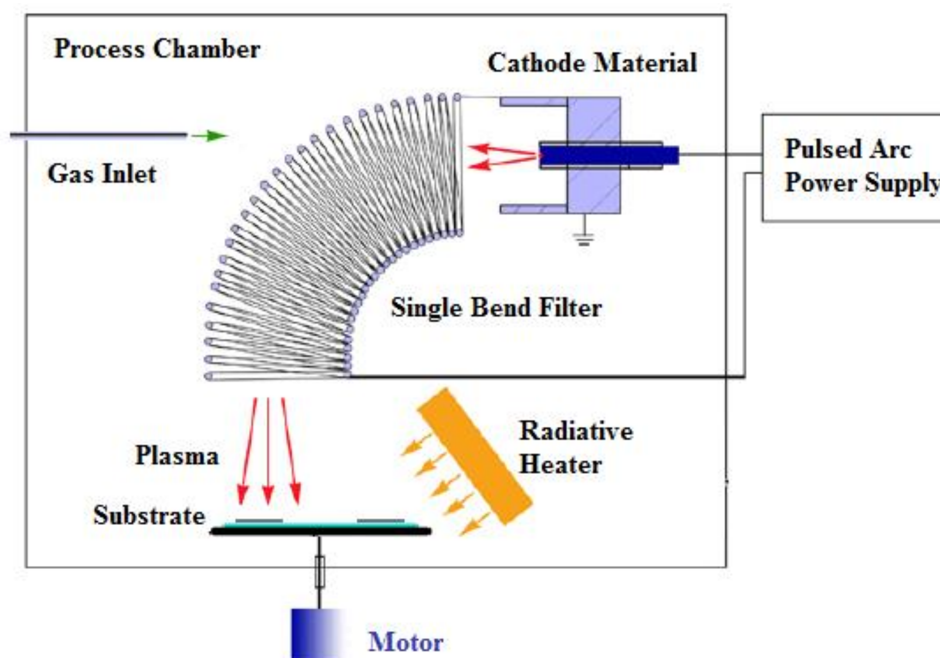

Figure 4-2: Deposition setup for the AZO films deposited by pulsed cathodic arc samples. AZO growth cycled between deposition and annealing during the deposition period [17].

4.2.2 Magnetron sputtering

In the pulsed magnetron sputtering deposition, a 51 mm zinc doped with 4% aluminium sputtering target was used. The target was 76 mm from the substrate and was pre-cleaned by depositing onto a shutter for 1 minute before each deposition. The substrate and samples were

heated to ~200 ºC using a 4 lamp radiative heater during deposition. The magnetron was a 50 mm close-to-balanced magnetron with modified connectors to allow for a high peak current of up to 500 A. The power supply was run in pulsed DC with 100 kHz pulse rate, 736 ns off time (+ve pulse) per cycle with an operating power of 75 W. The oxygen gas flow was adjusted to 60 sccm Ar, 36% O_2 (total pressure 7.5 mTorr) during the run to maintain a near constant operating voltage of 311-315 V.

4.2.3 High power impulse magnetron sputtering (HIPIMS)

For the HIPIMS samples, the same 4% aluminium doped zinc target was used as with the magnetron setup. Current pulses were supplied by an upgraded SPIK 2000A pulser, with a charging voltage up to 1000 V and pulse length of typically 400 µs. The total pressure within the chamber for all experiments was typically 1 Pa (7 mTorr). The magnetron was a 5 cm close-to-balanced magnetron that was placed 210 mm from the substrate. The substrate and samples were heated to ~200ºC using a 4-lamp radiative heater as this temperature was found to provide the best films for this setup [17].

4.2.4 Negative ion filter in magnetron deposition

To combat the effect of film degradation due to the geometry of the magnetron racetrack a simple straight line magnetic filter was introduced into the HIPIMS setup between the magnetron and the substrate. The filter setup is shown in figure 4-3. This acts to change the trajectory of the negative ions in the beam to force them away from the substrate and the AZO film being deposited. It will also act to focus the positive ions (for example our aluminium and zinc ions) towards the substrate, increasing the deposition rate. To test the effect of the ion filter on HIPIMS deposition, two samples were prepared. The first sample was prepared using the same setup as in section 4.2.3, but with the inclusion of the straight magnetic filter. A sufficient number of pulses to achieve a thickness of approximately 200 nm was chosen. The second sample was prepared in the exact same way, with the same number of pulses, but without the inclusion of the filter.

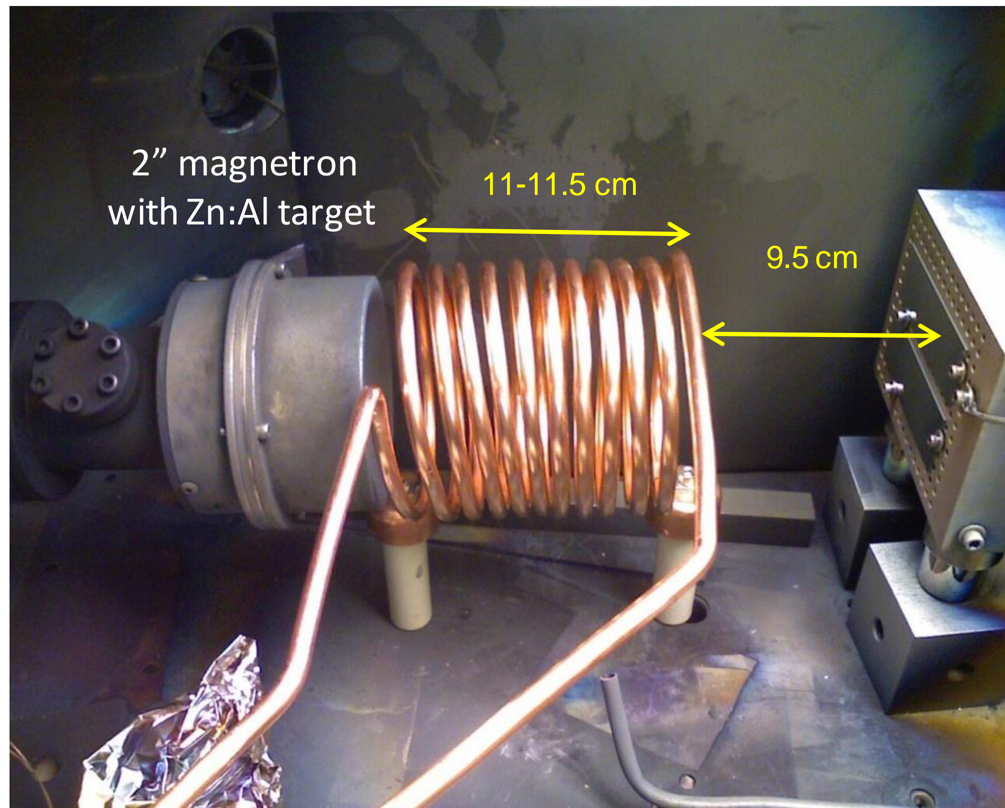

Figure 4-3: The HIPIMS setup with the inclusion of the straight magnetic filter.

4.3. Pulsed cathodic arc deposited films

It has been shown that thickness can affect the electrical properties of films, whereby films with larger grains (normally in thicker films) have lower resistivities [17]. Therefore a series of AZO films with different thicknesses were prepared and their properties compared.

4.3.1 Resistivity and Hall Effect

Table 4-2 summarises the results for the pulsed cathodic arc samples deposited with a variety of thicknesses at approximately 200ºC, as measured by the infrared sensor. Figure 4-2 shows a visual representation of the data in table 4-2. With an increase in thickness, an increase in mobility, an increase carrier density and a decrease in the resistivity is expected [17, 21, 29]. It can be seen that with the pulsed arc films, this trend is followed for thicknesses greater than 100 nm, but not with the thinner films. Completely contradictory to previous results [17], the films

of thickness approximately 25 nm show similar resistivity to the thickest films. It can also be seen that the carrier concentration decreases in the thicker films, where it is expected to increase [17]. However, the expected increase in mobility with increased film thickness was observed. These results show that film thickness is not the only factor which determines how the AZO coatings perform electrically.

Table 4-2: Pulsed arc electrical results. Electrical results were determined from the Hall Effect measurements.

Sample	Thickness (nm)	n_e (cm^{-3})	μ (cm^2/Vs)	ρ (Ω-cm)
a	24	2.40×10^{21}	11.6	2.24×10^{-4}
b	27	2.59×10^{21}	17.8	1.36×10^{-4}
c	260	7.63×10^{20}	33.2	2.46×10^{-4}
d	330	9.50×10^{20}	39.2	1.67×10^{-4}

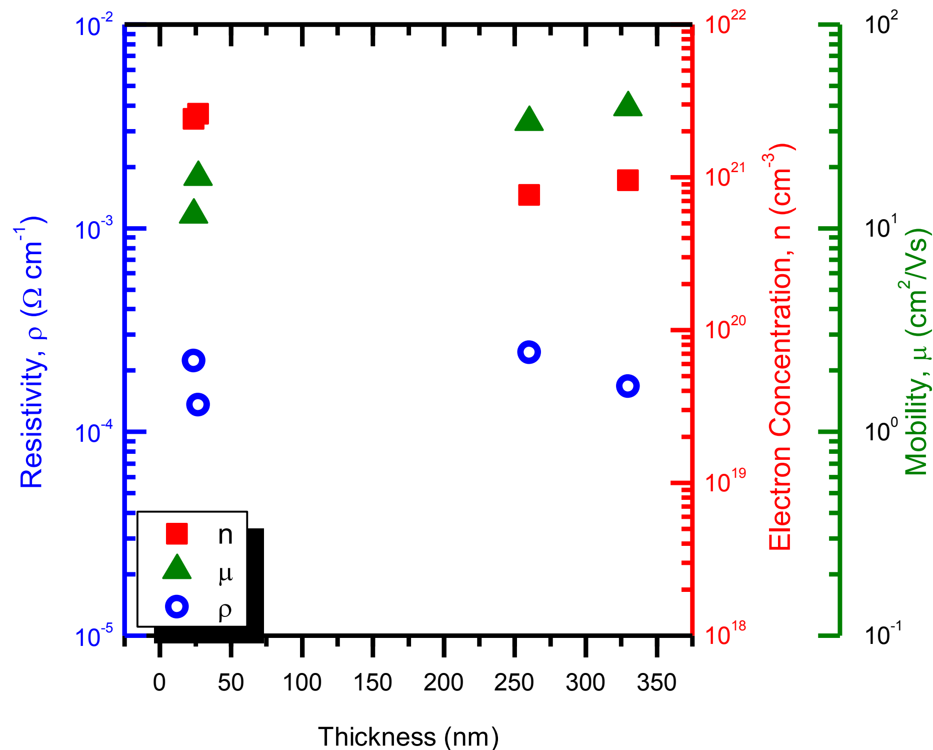

Figure 4-4: Electrical characteristics of the AZO films deposited using the pulsed cathodic arc technique. n is the electron concentration, μ is the mobility and ρ is the resistivity.

4.3.2 Optical transmission

Optical transmission analysis was performed and the results for the pulsed arc sample are shown in figure 4-5 for a representative thin (~25nm, sample (a)) and thick (>250nm, sample (c)) films. It can be seen that with the increase in thickness, there is a dramatic drop in the transmission in the infrared region of the spectra. It should be noted though, that even for the thicker films, represented by sample (c), the transmission in the optical region is very high. This was also noted with visual inspection of the films in which all appeared very transparent.

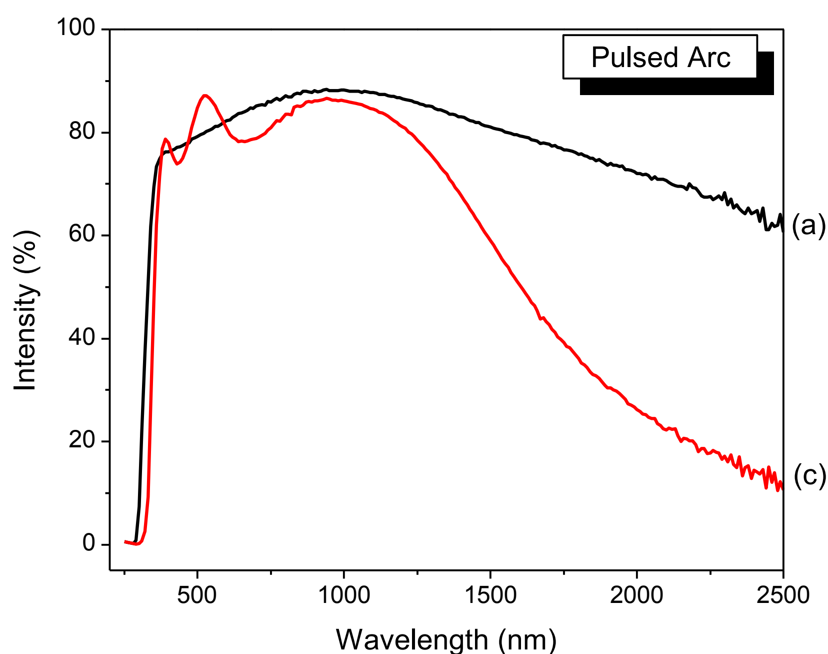

Figure 4-5: Optical transmittance spectra for the pulsed cathodic arc deposited films of increasing thickness. Thicker films exhibited less optical transmission in the infrared.

4.3.3 Composition and microstructure

For this set of experiments XPS was performed using the Thermo Scientific K-Alpha (see section 2.2.3). This allows for simple point analysis, as well as the ability to perform depth profiles and line scans across the surface of the sample.

Figure 4-6 shows the Zn2p, O1s and Al2p binding energy spectra for a representative thin (a) and thick (c) sample deposited using the pulsed arc system. A light sputter clean was performed before each experiment, so it is possible that the surface bonding has been damaged. These spectra are labelled a-d as described in table 4-2. Slight shifting in the spectra in the order of ~0.1 eV can be observed between samples, probably due to charging of the sample during analysis.

The Zn2p spectra are typical of that previously observed from ZnO [30, 31], with the Zn2p3 and Zn2p1 peaks located at 1022.2 eV and 1045.4 eV respectively. Slight broadening of the O1s spectra away from a gaussian shape is observed, indicating that the oxygen atoms within the films are not all bonded the same way. This is either the result of contaminants within the vacuum during analysis, or bonding to aluminium in some way, possibly indicating the presence of Al_2O_3. The Al2p peak has a very weak intensity due to its low concentrations and appears at approximately 74.6 eV, which matches well with the binding energy of Al_2O_3 given by the Scofield's XPS peak position data [32].

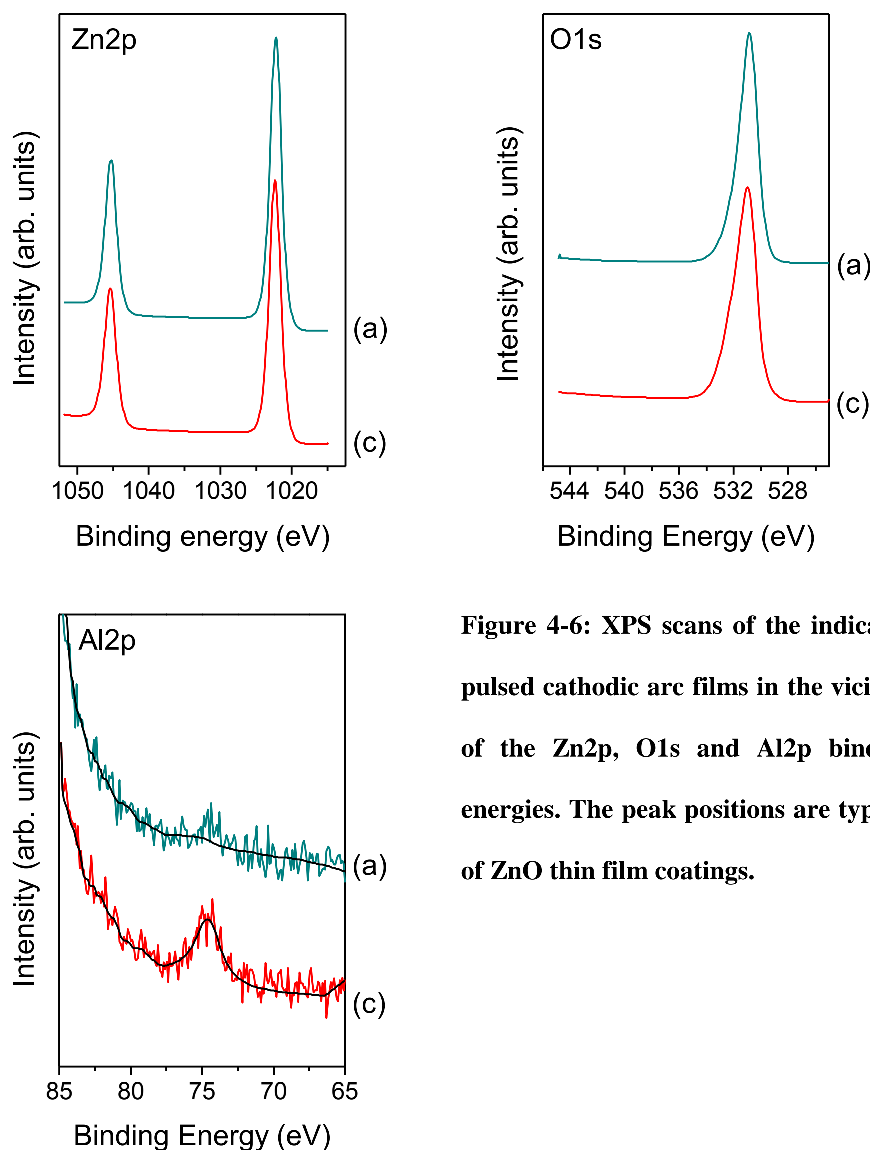

Figure 4-6: XPS scans of the indicated pulsed cathodic arc films in the vicinity of the Zn2p, O1s and Al2p binding energies. The peak positions are typical of ZnO thin film coatings.

Using the normalised peak area and sensitivity factors we determine the atomic percentages of the elements within the coatings. Table 4-3 shows the stoichiometry results for the pulsed cathodic arc films of varying thicknesses. It can be seen with these films that the overall aluminium concentration of the films stays approximately the same as that found within the cathode material. All of the films were found to be oxygen deficient, possibly due to preferential oxygen sputtering during the sputter cleaning with Ar^+ ions. [33]

Table 4-3: Details for the atomic percentages of the pulsed arc deposited AZO films.

Sample	Thickness (nm)	%Zn	%O	%Al
a	24	55.5	41.4	3.1
c	260	52.5	43.8	3.7

Figure 4-7 shows a comparison of the XRD spectra between the pulsed cathodic arc deposited samples of different thickness. The peaks located at approximately 2θ~34.1° and 2θ~72.5° are first and second order (002) planes (labelled peaks '1' and '2' in figure 4-7) of wurtzite ZnO. As well as these main features, evidence for other phases are also present. The strong peak located at 2θ~33° (peak 3) can be indexed to the hexagonal β-Al_2O_3 crystal phase (ICDD card no. 51-0769). This is strong evidence that the aluminium present in the sample is not all acting as dopants in ZnO, but is forming aluminium oxide in the sample. This result coincides well with the result found above in the XPS analysis in which the oxygen appeared to be forming more than one oxide phase. Interestingly enough, the inclusion of aluminium oxide does not appear to have a strong negative effect on the films electrical properties as one might expect from an insulating oxide. The peak located at 2θ~31° can be indexed to (220) planes of the gahnite phase ($ZnAl_2O_4$). The formation of Al_2O_3 and $ZnAl_2O_4$ is usually considered to impact negatively on the conductivity of AZO films and is not usually seen in XRD [8, 34, 35]. However, the electrical properties in these coatings, despite being compromised by unwanted materials, still perform better than other works [34, 35].

Using the Sherrer equation, the average grain size of the wurtzite ZnO crystals in the pulsed arc samples was calculated from the width of the (002) peak and is shown in table 4-4. It can be seen that for the pulsed cathodic arc samples the average grain size tends to be in the 30 nm range. It should also be noted that for the thin film coating (thickness 24 nm), the average grain size was found to be 24 nm, approximately the same thickness of the actual film. This is an interesting result as it suggests that the relative size of the grains within the films plays a stronger role on the electrical properties than the film thickness does.

Table 4-4: XRD of pulsed arc samples showing the film thickness, Bragg scattering angle, FWHM of the XRD peak and the calculated crystal grain size.

Sample	Thickness (nm)	$2\theta_B$ (deg)	FWHM (deg)	D (nm)
a	24	34.54	0.35	24
c	260	34.68	0.26	32

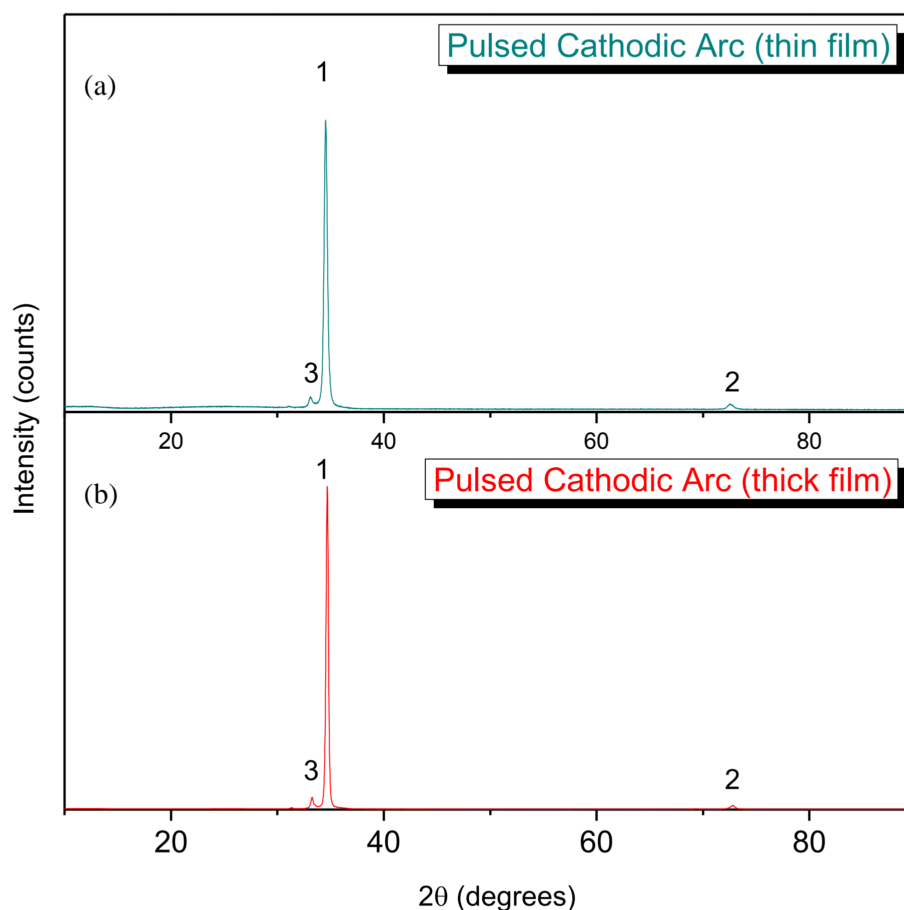

Figure 4-7: XRD of the pulsed cathodic arc samples of the samples with thickness (a) 24 nm and (b) 260 nm.

X-ray absorption spectroscopy was performed at the Australian Synchrotron to investigate the zinc L-edge, oxygen K-edge and aluminium K-edge for each of the samples to better understand the local bonding arrangements in the films. Given that the XPS and XRD results showed little difference in the microstructure of the films, only a single representative sample

(c) was selected for this experiment. Figure 4-8a shows the aluminium K-edge for the AZO coating with a thickness of 260 nm. The peaks located at approximately 1567.4 eV and 1571.5 eV refer to the la_g to e_u transition and the multiple scattering contributions respectively [5]. The peak at 1567.4 eV is characteristic of distorted octahedral coordination (AlO_6, with 6 fold symmetry) of the aluminium atoms with the surrounding oxygen environment [5, 36]. The peak characteristic of tetrahedral coordination (located at approximately 1565.4 eV) is not present within these films [5, 36]. This result supports the XPS and XRD results in which it was found that the aluminium was appearing as aluminium oxide (Al_2O_3) and not as a dopant.

Figure 4-8b shows the XAS in the region of the oxygen K-edge for the pulsed arc deposited coating. The only prominent feature in the spectrum is a broad peak at approximately 538 eV due to transitions of the O1s electrons to the O2p and Zn4sp hybrid orbital. The peaks relating to the O1s to O2p and Zn3d orbitals are present because of the d^{10} configuration of ZnO [37]. Also shown in this figure is the oxygen K-edge calculated for wurtzite ZnO using the FEFF9 code. It can be seen that there is extra broadening of features in the pulsed arc XANES, making the transition peak appear washed out. This is possibly due to the inclusion of oxygen K-edge contributions from Al_2O_3 or other oxidised Zn/Al phases. Figure 4-8c shows the XAS spectrum in the region of the zinc L-edges. The energy positions and shape of the spectra match well with that previously reported for ZnO using XANES [38].

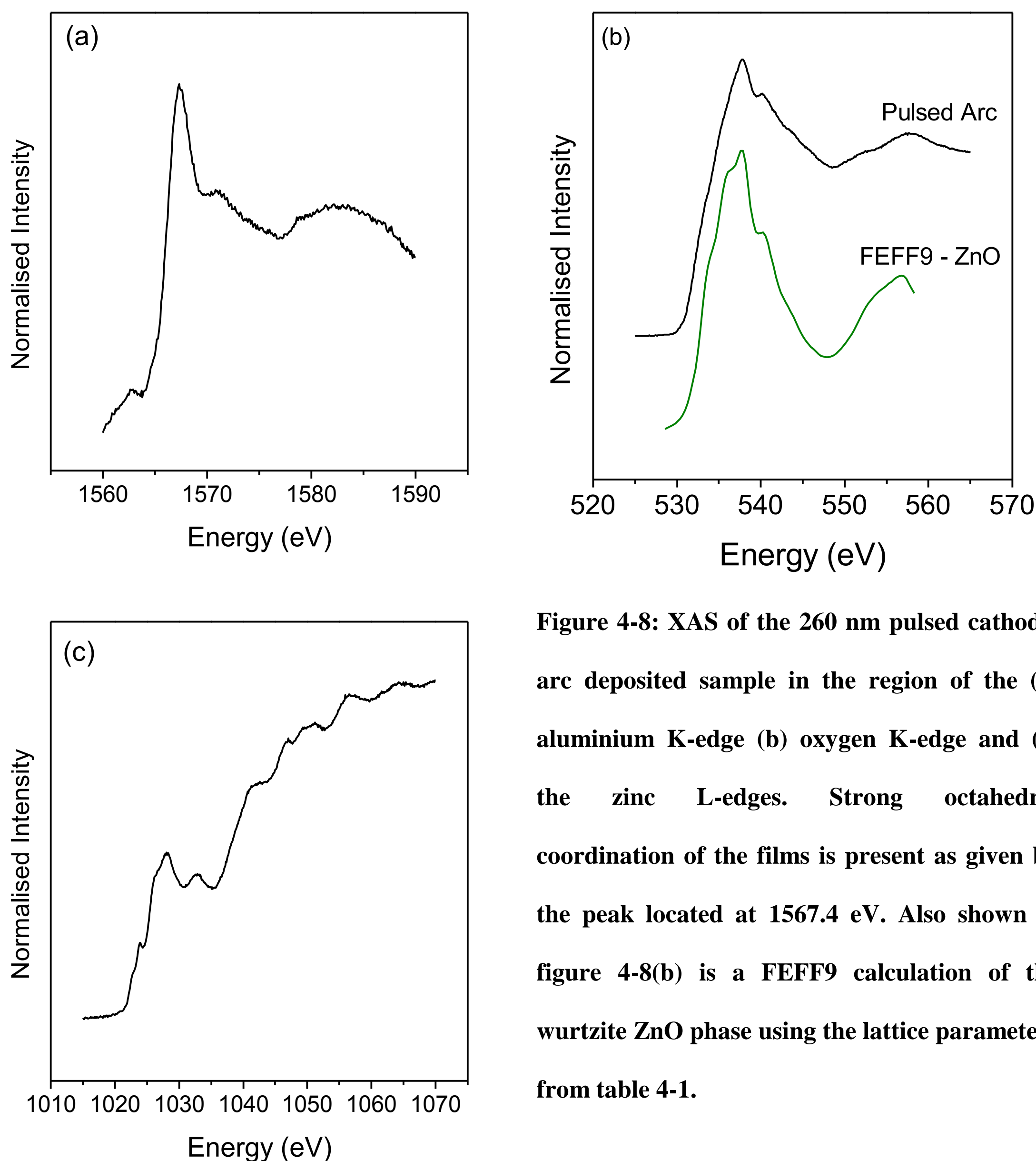

Figure 4-8: XAS of the 260 nm pulsed cathodic arc deposited sample in the region of the (a) aluminium K-edge (b) oxygen K-edge and (c) the zinc L-edges. Strong octahedral coordination of the films is present as given by the peak located at 1567.4 eV. Also shown in figure 4-8(b) is a FEFF9 calculation of the wurtzite ZnO phase using the lattice parameters from table 4-1.

Figure 4-9a shows a bright field cross-sectional image of the AZO sample (c) deposited using pulsed cathodic arc onto a microscope coverslip. Indicated in the figure are the SiO_2 (glass) substrate on the left hand side, the AZO film running down the centre. Note that the surface of the sample has been overthinned, causing a roughing of the surface. The film appears to contain darker regions which maybe grains of crystalline materials. Figure 4-9b shows a high resolution image of one such grain. The fringe separation was found to be approximately 5.6 Å aligned parallel to the growth direction. These correspond to the (002) planes of ZnO.

The indexed diffraction pattern for this area is shown in figure 4-10 (left). The diffraction pattern itself is comprised of a combination of diffraction patterns each from crystal grains with strong c-axis <001> orientation (as seen by the strong intensity of the respective spots) perpendicular to the surface. Each of these grains has a different amount of rotation around the c-axis, so we observe diffraction patterns from different Laue zones simultaneously. Figure 4-10 (right) shows the indexing of the diffraction pattern from 3 different Laue zones ([110] [210] and [310]) and a molecular representation (left) of the orientation of the particular grains as calculated using the JEMS software package [39].

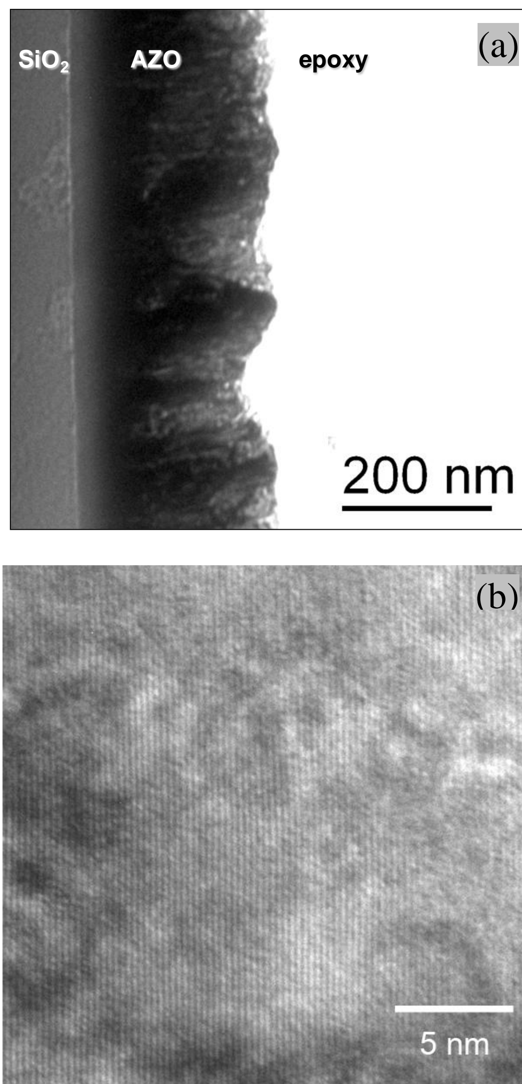

Figure 4-9: TEM image of the pulsed cathodic arc sample. Indicated within the image (a) are the SiO_2 (glass) substrate and the AZO film (dark region). A high resolution image is also shown (b) where the ZnO(002) planes parallel to the surface of the substrate can be seen.

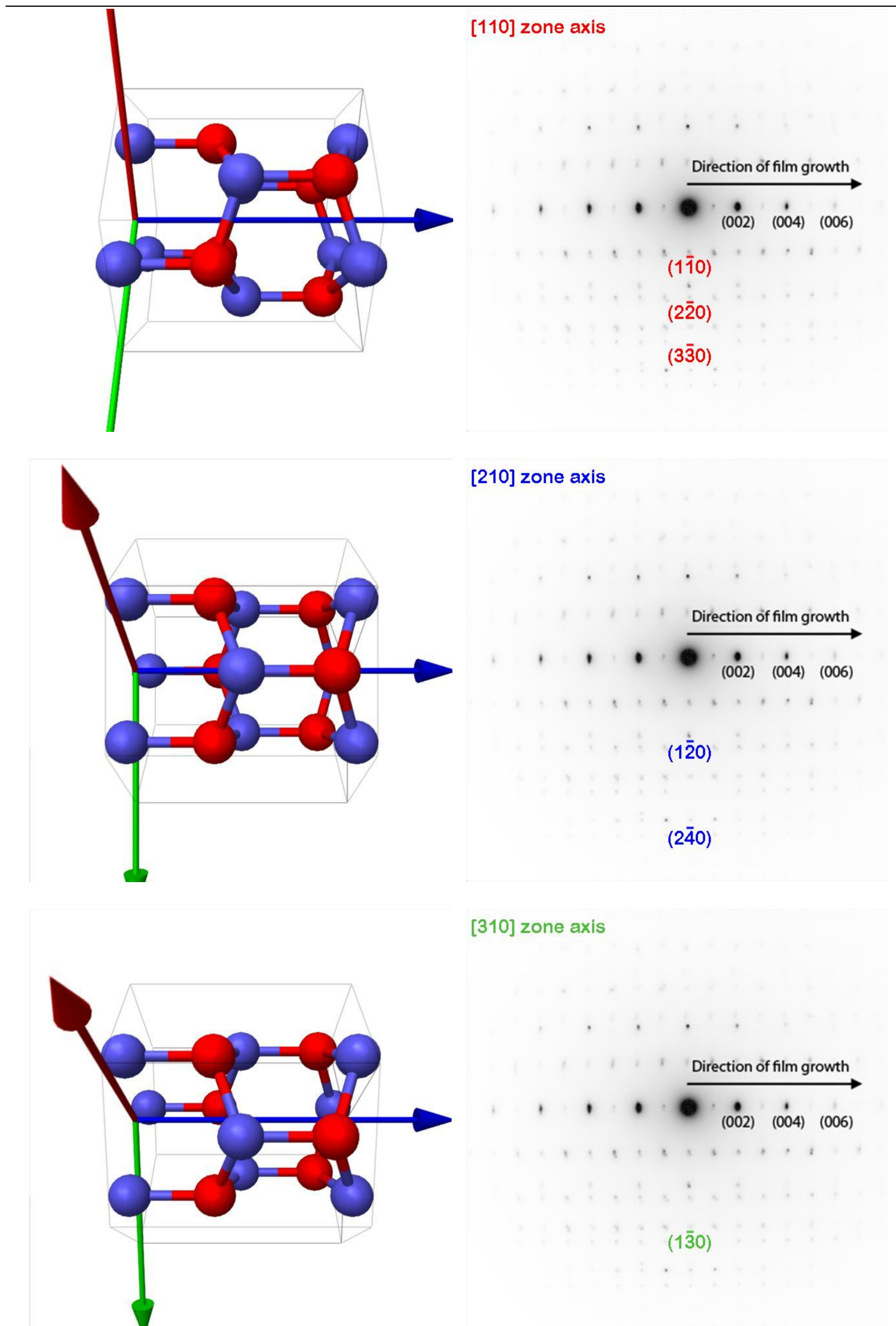

Figure 4-10: Left hand side shows a molecular representation (zinc is blue, oxygen is red) of the ZnO crystals in the lattice looking down the different zone axes. The right hand side images show the diffraction patterns

4.4 Magnetron sputtered films

The results for the experiments carried out on the magnetron sputtered samples are presented in this section, as well as an analysis of the non-uniformity of the films across the face of the substrate since visual inspection revealed that the films were not uniform across the surface.

4.4.1 Resistivity and Hall Effect

Table 4-5 shows the electrical characteristics for the magnetron sputtered samples using both the Hall effect and 4 point probe measurement techniques in approximately the same positions. The position numbers in the table represent positions across the sample as indicated in figure 4-11. The highlighted positions (2 and 4) were the only ones in which sufficient sample area could be utilised for Hall Effect measurements. These particular positions are used later in the chapter for comparisons across the sample for optical transmission measurements, spectroscopy and x-ray diffraction. It can be seen from these results that towards the inside of the sample (position 4) there is a significant decrease in both carrier concentration and mobility, resulting in an increase in the resistivity by 2 orders of magnitude. Given that between positions 2 and 4 the film thickness is similar, this change in electrical properties is an indication that the film microstructure changes across the sample in the shape of the magnetron ring (see 2.1.4). The likely cause for this change in microstructure is O^- bombardment of the film as discussed in section 4.2.4.

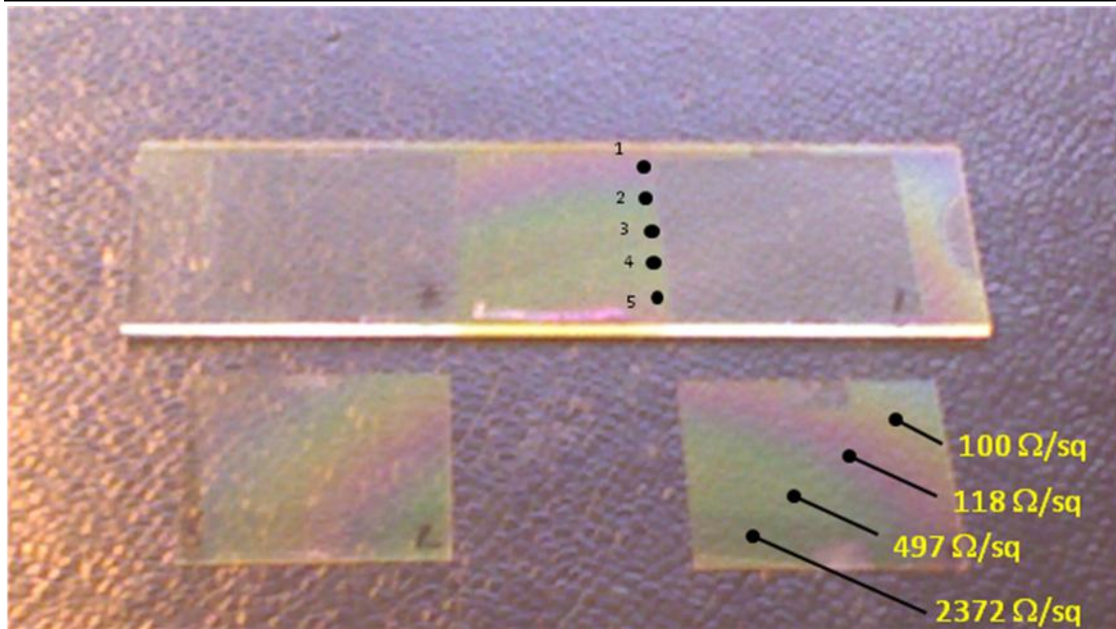

Figure 4-11: The magnetron sputtering sample. AZO films were simultaneously deposited onto glass microscope slide (top) and 2 glass coverslips (bottom). Hall and resistance measurements were taken at various points on the samples.

Table 4-5: Electrical measurements performed on the samples deposited by magnetron sputtering. Highlighted cells refer to locations on the samples that are analysed later with other techniques. NM refers to points where no measurement was possible.

			4 point probe		Hall Effect		
Position	Distance (mm)	Thickness (nm)	Rs (Ω/sq)	ρ (Ω.cm)	n_e (cm^{-3})	μ (cm^2/Vs)	ρ (Ω.cm)
1	0	238	122	2.9×10^{-3}			
2	4.5	318	252	8.0×10^{-3}	1.6×10^{20}	11.1	3.6×10^{-3}
3	10	326	1957	6.4×10^{-2}			
4	13.5	370	22197	8.2×10^{-1}	2.5×10^{19}	0.438	5.6×10^{-1}
5	17.5	366	NM	NM			

4.4.2 Optical transmission

Figure 4-12 shows the transmittance for AZO films grown with magnetron sputtering at positions 2 (outside) and 4 (inside) of the magnetron ring. Greater carrier concentrations found towards the outside of the samples (as evidenced in the electrical data in table 4-5) leads to a shift of the plasma edge in the near infrared towards shorter wavelengths. This results in a

reduction of the film transparency by approximately 10%, giving a film that is semi-transparent in the optical region with a yellowish hue.

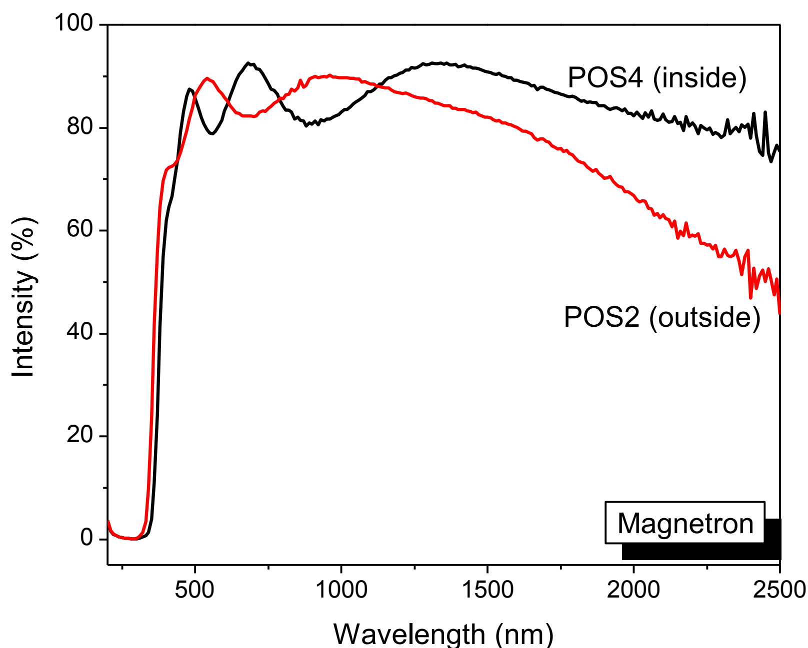

Figure 4-12: Optical transmittance spectra across the surface of the magnetron sample. POS2 (red) refers to the outside of the substrate and POS4 (black) refers to the inside of the substrate

4.4.3 Composition and microstructure

Figure 4-13 shows the XPS spectra for the magnetron sample in the regions of the Zn2p, O1s and Al2p binding energies. For each graph (a) represents the point towards the inside of the samples during deposition and (b) represents the point towards the outside of the samples. It can be seen from the spectra that there is negligible change in the binding energy across the surface of the samples, although care must be taken due to possible damage to the surface bonds during the sputter cleaning process. The negligible change indicates that although there is a change in the macroscopic properties of the films, the bonding on an atomic level remains similar. As with the pulsed cathodic arc samples, both the Zn2p and O1s spectra match well with previous works [30, 31]. For the Al2p spectra, the line enveloping the main signal is shown alongside the raw data. This peak is located at 74.7 eV, a good match with the Scofield XPS data of Al_2O_3 [32]. Unlike the pulsed cathodic arc samples, the oxygen 1s spectra is less broadened, representing fewer oxidation states. Table 4-6 shows the atomic percentage of the

magnetron sample across the surface. It can be seen that despite the change in colouration across the films, the stoichiometry of the magnetron samples remains both constant and very close to that of the cathode material.

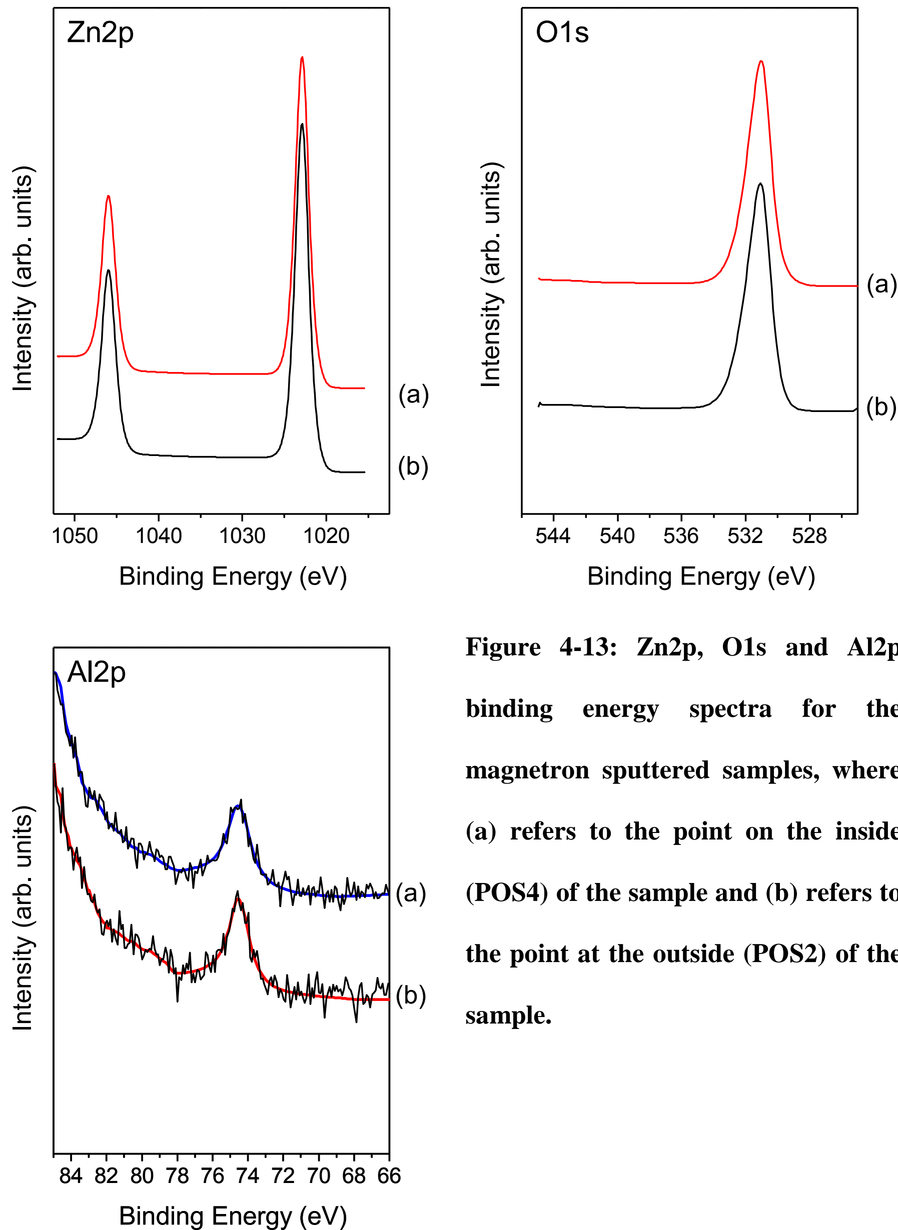

Figure 4-13: Zn2p, O1s and Al2p binding energy spectra for the magnetron sputtered samples, where (a) refers to the point on the inside (POS4) of the sample and (b) refers to the point at the outside (POS2) of the sample.

Table 4-6: Details of the XPS experiment on the magnetron sputtered samples

Spectrum	Position	Thickness (nm)	%Zn	%O	%Al
a	4 (inside)	370	47.1	48.6	4.3
b	2 (outside)	318	47.9	47.9	4.2

Figure 4-14 shows the atomic percentage of aluminium across the surface (along the line from A to B, traversing the radius of the magnetron rings) of the sample using an XPS linescan. Also shown in the line profile is a line of best fit. Low concentrations of aluminium in the films leads to noise in the Al2p spectra and consequently in the atomic percentage profile. It can be seen that there is little change in the atomic percentage across the surface of the film, despite a change in both the optical transmission (figure 4-10) and the resistivity (table 4-4). This suggests that the effect of the O^- bombardment due to the magnetron is not to greatly affect the film's composition, but still affects the physical properties.

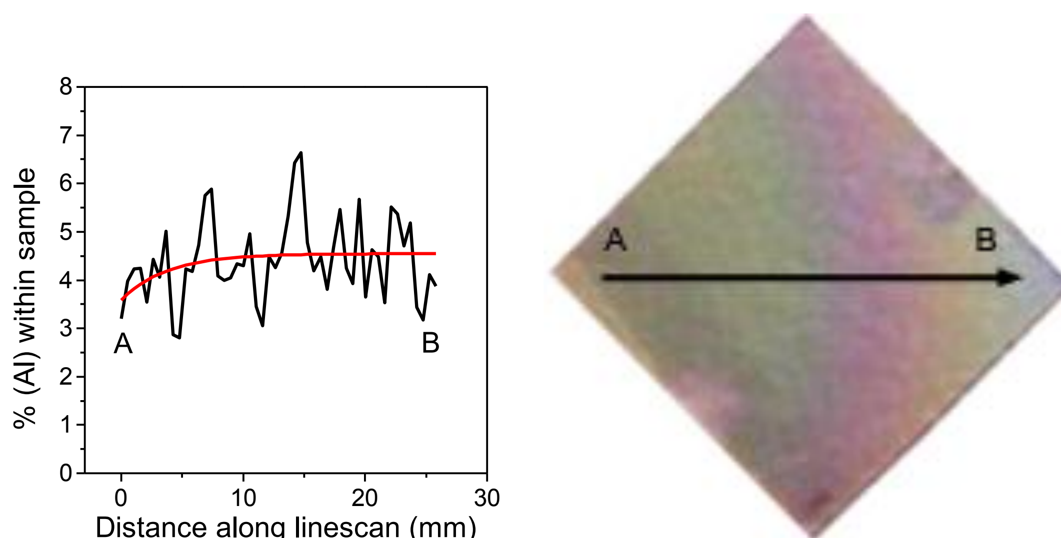

Figure 4-14: Variation in aluminium concentration across the surface of the magnetron deposited AZO film.

Figure 4-15 shows the XRD spectra of the magnetron deposited sample at position 2, located at the outside of the sample and position 4 is located towards the centre of the sample. The peaks located at $2\theta = 34.1°$ and $72.5°$ (labelled '1' and '2' respectively) can be attributed to first and second order diffraction from wurtzite ZnO(002) planes. The strength of these peaks is an indication of good c-axis (vertical growth to substrate) orientation. The peak located at $2\theta = 33.0°$ (peak '3') has been indexed to the β-Al_2O_3 phase (ICDD card no. 51-0769). Unlike the pulsed arc samples, only trace amounts of the gahnite phase (at $2\theta = 31.1°$) are present in the

magnetron sputtered films. There is little difference between the two spectra, indicating that the crystallography across the surface of the sample is similar.

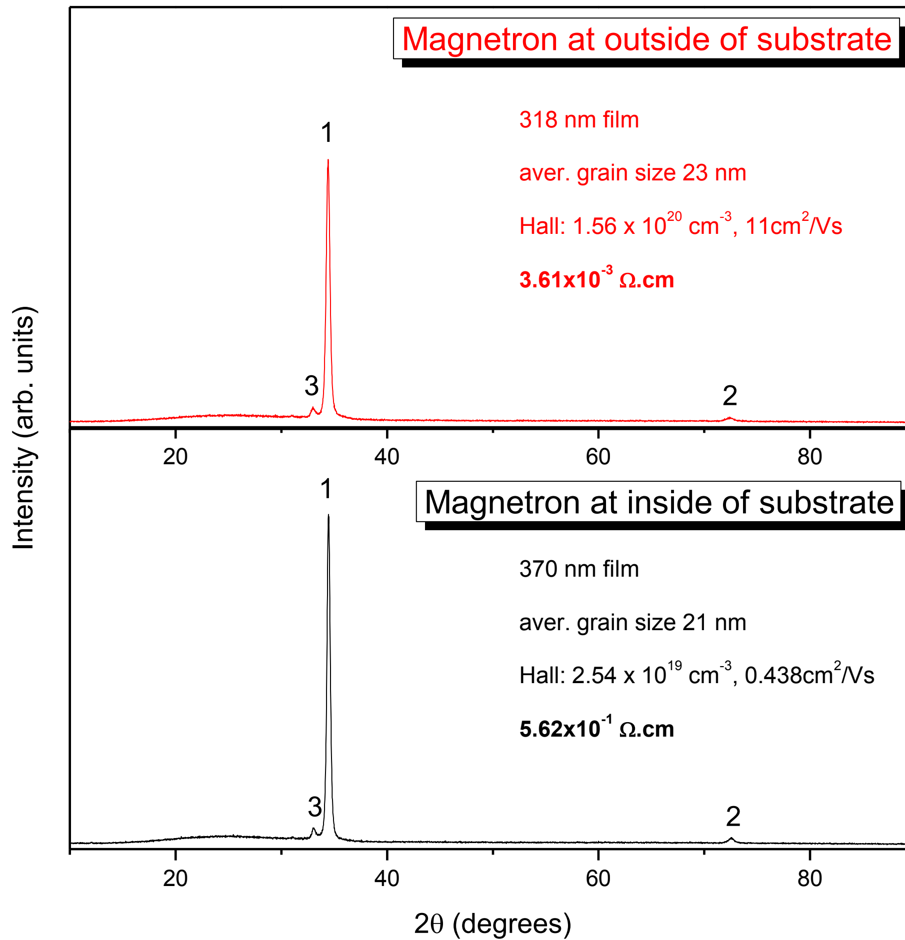

Figure 4-15: XRD spectra of the magnetron sputtered sample at the outside (top) and inside (bottom) of the substrate. These locations refer to positions 2 and 4 from table 4 respectively.

Using Scherrer's equation the average grain size is calculated from the FWHM of the (002) peak to determine the average grain size. Table 4-7 shows the grain size for each of the positions in which it can be seen that across the surface of the film there are slightly smaller grains towards the centre of the film.

Table 4-7: Peak position and grain size analysis of the AZO samples deposited using magnetron sputtering and HIPIMS.

Sample	Thickness (nm)	$2\theta_B$ (deg)	FWHM (deg)	D (nm)
Magnetron (inside)	370	34.44	0.40	21
Magnetron (outside)	318	34.46	0.36	23

Figure 4-16 shows the XAS spectra for the magnetron sputtered samples at the indicated positions compared to that of the pulsed cathodic arc (figure 4-8). Spectra were taken in the region of the aluminium K-edge, oxygen K-edge and zinc L-edges. Figure 4-16a shows the XAS spectra in the region of the aluminium K-edge. It can be seen that the coatings contain octahedrally coordinated Al as indicated by the peak located at 1567.7 eV, with little to no tetrahedral coordination present. Using the peak at 1571.5 eV (multiple scattering contributions) as a reference, it can be seen that the peak relating to octahedral coordinated Al is lower for the region at the inside of the film. This also suggests that the poorer electrical properties presented in table 4-5 may result from the film having less short range order in this region. This reduced order at the centre of the coating may be a result of the *in situ* O-bombardment outlined in section 4.1.4. Compared to the pulsed cathodic arc sample, the octahedral peak for the magnetron sputtered films is significantly less intense. The larger amount of short range order in the pulsed arc sample is probably due to a combination of the 90º magnetic filter and the higher energy plasma. A similar effect was observed in chapter 3 in which more ordered WO_3 films were produced by pulsed cathodic arc compared to magnetron sputtering.

Figure 4-16b shows the XAS spectrum in the region of the oxygen K-edge of the magnetron sputtered sample. The general shape of the spectra is characteristic of the ZnO (d^{10}) configuration with little difference between the positions across the film. However, unlike the pulsed arc sample, there appears to be some structure appearing on the edge at approximately 535 eV. It is possible that the disorder in these films is allowing for the appearance of more unoccupied states. The magnetron sputtered samples show less broadening of the main peak than the pulsed arc sample did, indicating that less oxidised phases are present. Also shown in this figure is the FEFF9 calculation of the ZnO wurtzite phase. It can be seen that a better match is achieved with the magnetron sputtered sample than the pulsed arc sample, indicating that the magnetron sputtered samples have other types of oxidised phases and were primarily wurtzite ZnO. Figure 4-16c shows the XAS in the region of the Zn L-edges, in which the spectra are characteristic of ZnO [38].

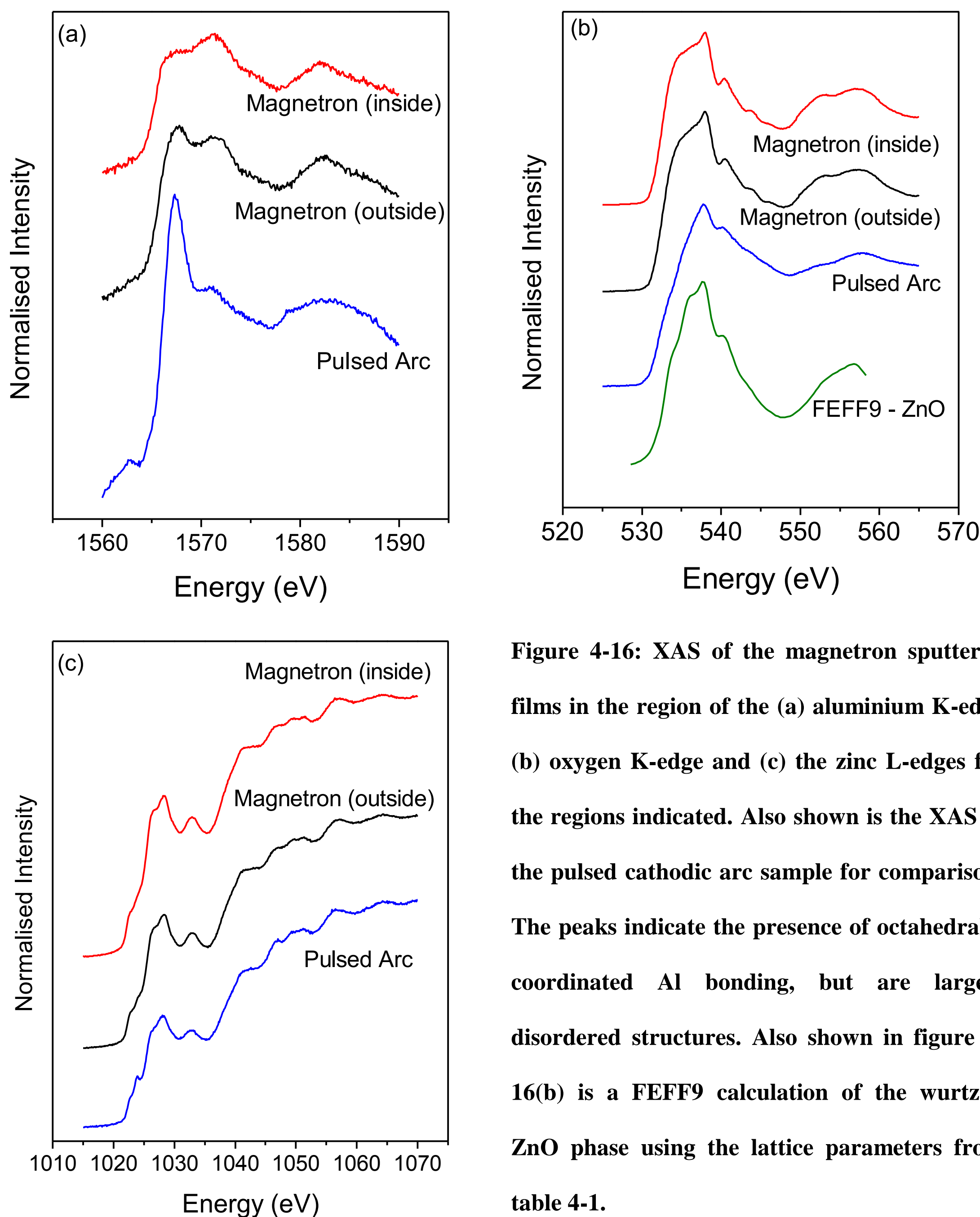

Figure 4-16: XAS of the magnetron sputtered films in the region of the (a) aluminium K-edge (b) oxygen K-edge and (c) the zinc L-edges for the regions indicated. Also shown is the XAS of the pulsed cathodic arc sample for comparison. The peaks indicate the presence of octahedrally coordinated Al bonding, but are largely disordered structures. Also shown in figure 4-16(b) is a FEFF9 calculation of the wurtzite ZnO phase using the lattice parameters from table 4-1.

4.5 HIPIMS

The results for the experiments carried out on the HIPIMS deposited samples are presented in this section. As with the magnetron sputtered samples, visual inspection of the films showed a variation in the film across the surface, suggesting that the samples were not homogenous.

4.5.1 Resistivity and Hall Effect

Table 4-8 shows the electrical characteristics of the sample deposited using the HIPIMS technique. 4 point probe and Hall effect measurements were taken in appoximately the same positions. The 'position' shown in the table refers to locations on the surface of the sample indicated in figure 4-17, where the main points of interest position 1 and position 3 are located at the outside and inside of the sample respectively. From the results a similar trend to that of the magnetron sputtered samples can be seen. At the outside of the sample superior electrical characteristics are seen, with a greater carrier concentration, greater mobility and a lesser resistivity.

Figure 4-18 shows the change in the resistivity across the surface of the sample. It can be seen that there is a dramatic increase in the resitivity towards the centre of the sample (positions 3 and 4). It is possible that large amounts of O^- ion damage, as outlined in section 4.1.4, has occured at the centre of the sample due to oxygen ions being accelerated towards the substrate as a result of the the magnetic fields of the magnetron.

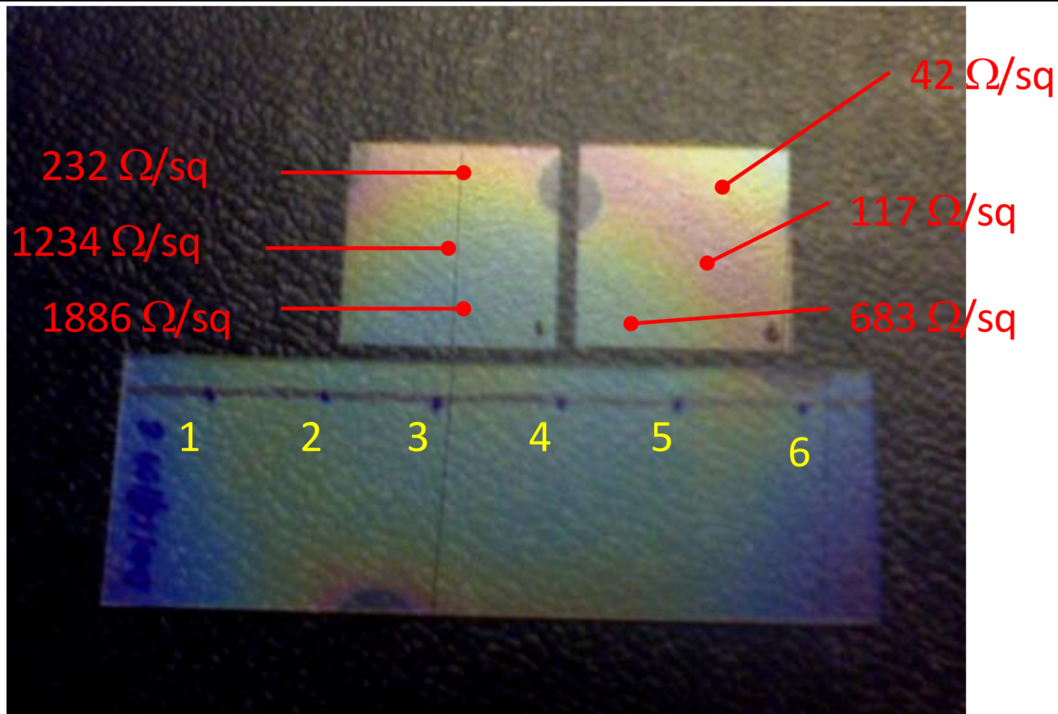

Figure 4-17: The deposited HIPIMS samples. The AZO films were deposited onto a glass microscope slide (bottom) and 2 glass coverslips (top). Points of interest are labelled on the image.

Table 4-8: Electrical characteristics for the HIPIMS sample. The positions refer to the points shown in figure 4-17. Highlighted cells refer to locations on the samples that are analysed later with other techniques

		4 point probe		Hall Effect		
Position	**Thickness (nm)**	**Rs (ohm/sq)**	**ρ (Ω–cm)**	**n_e (cm^{-3})**	**μ (cm^2/Vs)**	**ρ (Ω–cm)**
1	221	96	2.1×10^{-3}	5.10×10^{20}	7.16	1.7×10^{-3}
2	203	381	7.7×10^{-3}			
3	210	2710	5.7×10^{-2}	1.08×10^{20}	1.03	5.6×10^{-2}
4	218	2872	6.3×10^{-2}			
5	219	447	9.8×10^{-3}			
6	220	108	2.4×10^{-3}	6.30×10^{20}	5.9	1.7×10^{-3}

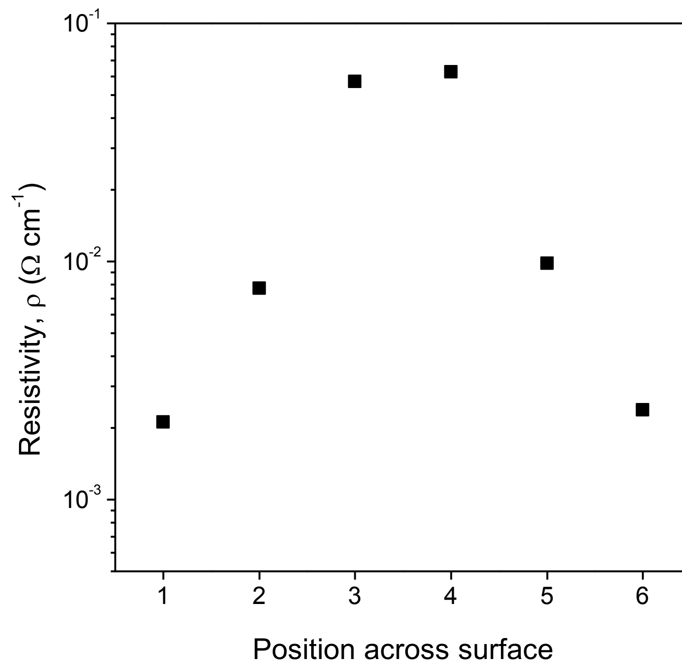

Figure 4-18: Resistivity of the HIPIMS sample across the surface as measured by 4 point probe.

4.5.2 Optical transmission

Figure 4-19 shows the transmittance spectra for the HIPIMS sample at positions 1 and 3, which refer to the outside and inside of the magnetron ring respectively. The overall shifting in the spectra in the visible region (~500 nm) results in a colour change of the films across the surface, as evidenced by the visual inspection.

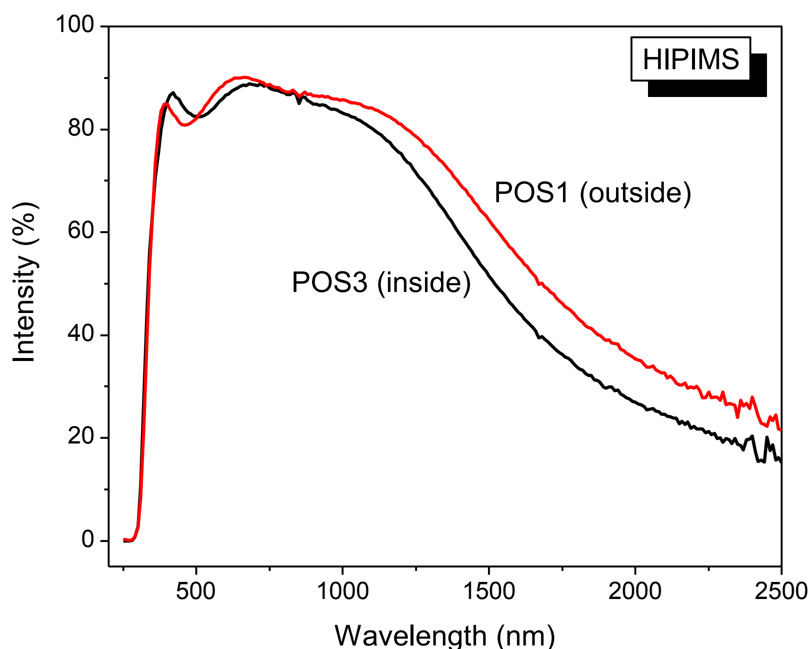

Figure 4-19: Optical transmittance spectra across the surface of the HIPIMS samples. POS1 (red) refers to the outside of the substrate and POS3 (black) refers to the inside of the substrate

4.5.3 Composition and microstructure

Figure 4-20 shows the results from XPS at the (a) inside of the sample and (b) outside of the sample (positions 3 and 1 respectively) in the regions of the Zn2p (left), O1s (centre) and Al2p (right) binding energies. Like the magnetron sample, the Zn2p and O1s peaks resemble that of previous works and are indicative of ZnO [30, 31]. The Al2p peak is located at 74.7 eV, indicative of Al_2O_3 in the film [32]. Table 4-10 shows the atomic percentages of zinc, oxygen and aluminium within the film. It can be seen that there is a noticeable change in the HIPIMS stoichiometry across the samples surface. At the outside of the sample, the atomic percentages resemble that of the magnetron and pulsed cathodic arc samples, with a large zinc concentration present, and an aluminium concentration approximately equal to that of the Zn/Al target material. At the inside of the sample (POS3), there is a decreased zinc content, which has been replaced with both oxygen and aluminium. In this particular area, the aluminium concentration has approximately doubled.

As discussed in 2.1.5, a greater ionisation rate is expected in HIPIMS compared to conventional magnetron sputtering. This means that any O^- ion damage of the sample during deposition will be enhanced for this experiment. The increased ion bombardment may also cause zinc atoms to be preferentially sputtered with respect to the aluminium atoms. This results in an area which is zinc deficient with respect to the rest of the thin film and has inferior electrical properties (table 4-9).

Figure 4-20 shows the change in aluminium atomic percentage of the HIPIMS deposited sample across the sample surface using an XPS linescan. The scan runs across the diagonals of the sample from position A to B so that it runs perpendicular to the coloured rings inherent to the HIPIMS samples. It can be seen that the aluminium percentage rises nearer to the centre of the sample (position B). It is towards the centre of the sample that the resistivity of the films is higher.

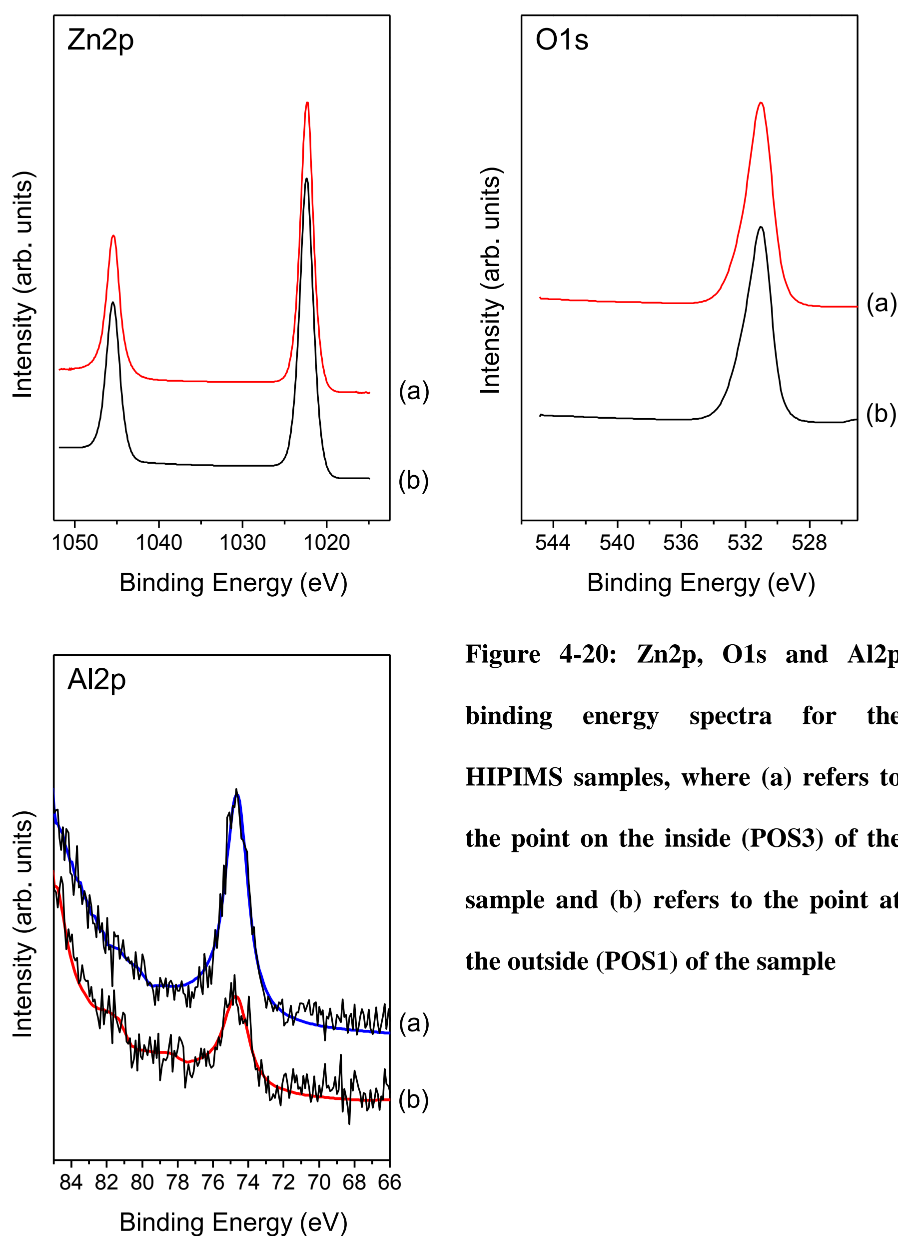

Figure 4-20: Zn2p, O1s and Al2p binding energy spectra for the HIPIMS samples, where (a) refers to the point on the inside (POS3) of the sample and (b) refers to the point at the outside (POS1) of the sample

Table 4-9: Details of the XPS experiment on the static HIPIMS sample. POS3 refers to the inside of the sample, POS1 refers to the outside of the sample

Spectrum	Position	Thickness (nm)	%Zn	%O	%Al
a	3 (inside)	220	41.3	50.8	7.9
b	1 (outside)	220	44.9	50.3	4.9

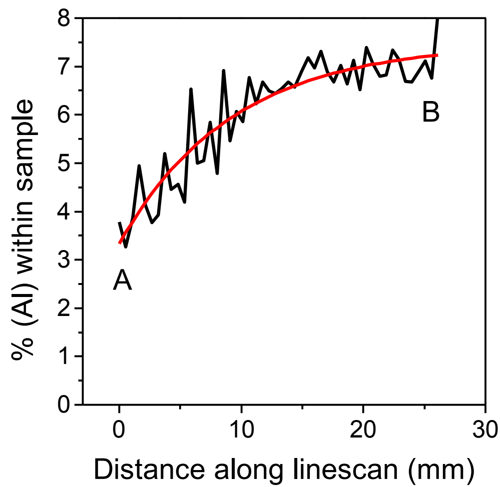

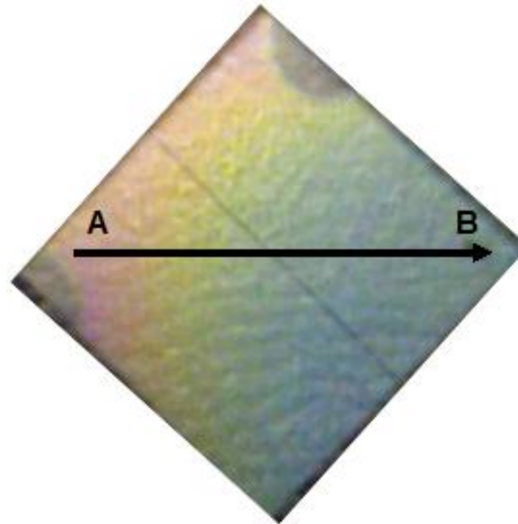

Figure 4-21: XPS line scan of the Al2p peak across the surface of the HIPIMS sample from position A to B.

Figure 4-22 shows the XRD spectra of the HIPIMS sample at two different positions, one in the centre of the sample (position 3 from table 4-8) and one towards the outer edge of the sample (position 1). It can be seen in this case that that both films are disordered with small amounts of ZnO(002) crystal growth. Due to broadening of the peaks, it is not clear whether the β-Al_2O_3 or the gahnite phases are present. Between the two positions on the coating, there is a large variation in the intensity of the ZnO(002) peak, indicating that at the centre of the sample, significant ion damage to the oriented growth has occurred. This result supports the XPS result in which it was found that preferential O^- ion sputtering of the zinc atoms towards the inside of the was occurring.

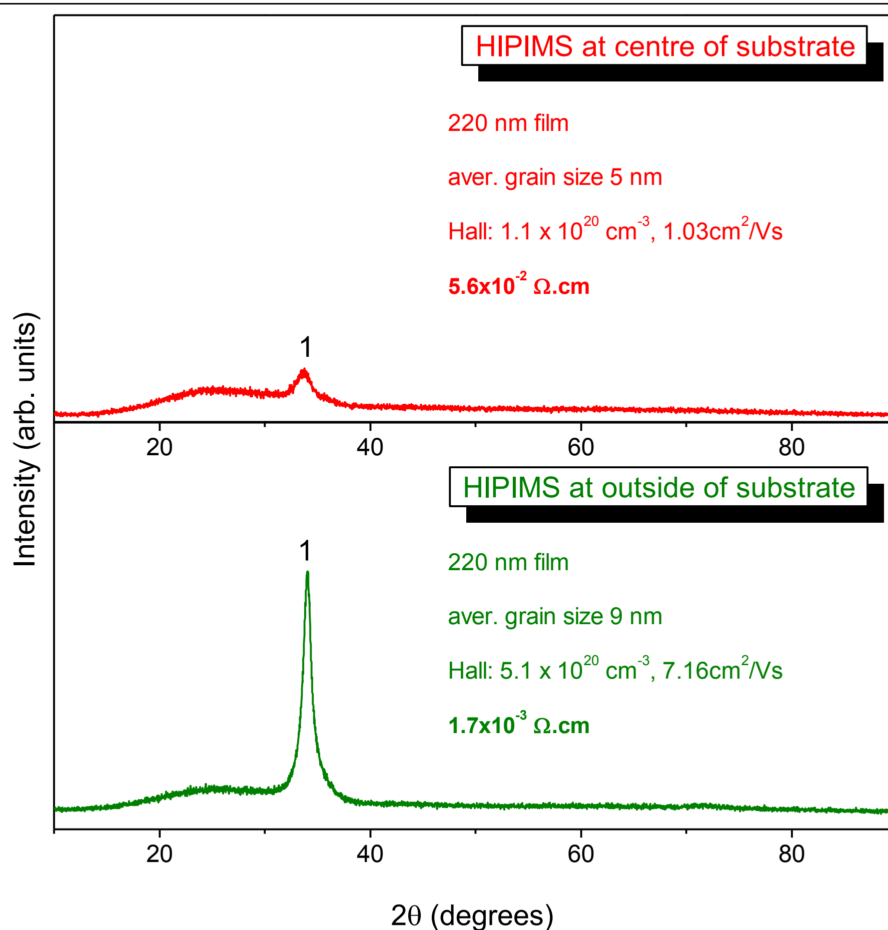

Figure 4-22: Comparison of the HIPIMS XRD. Shown in the figure are the respective grain size and Hall measurements for each of the samples.

Using the Scherrer equation the average grain size was calculated. Table 4-10 shows the Bragg scattering angle and the grain size for the HIPIMS sample at each of the positions. It can be seen that even though the HIPIMS sample is thick, the grain size is significantly reduced compared to the magnetron sputtered sample. Like the magnetron sample, the smaller grains are located towards the inside of the magnetron ring where it is believed that the most O^- ion damage is occurring.

Table 4-10: Peak position and grain size analysis of the AZO samples deposited using magnetron sputtering and HIPIMS.

Sample	Thickness (nm)	$2\theta_B$ (deg)	FWHM (deg)	D (nm)
HIPIMS (inside)	220	33.73	1.55	5
HIPIMS (outside)	220	34.10	0.91	9

Figure 4-23a shows the XAS in the region of the aluminium K-edge for HIPIMS deposited sample at the regions indicated. It can be seen that like the other deposition methods, the peak at 1567.7 eV shows the presence of octahedrally coordinated Al within the sample, with no indication of tetrahedrally coordinated Al present. It can be seen from the relative intensities of the spectra that there is a lot more aluminium present in the HIPIMS sample towards the centre (as evidenced by the XPS results).. The peaks in the HIPIMS (inside) spectra are also less resolved than the other spectra, another indication of the disorder present within the film.

Figure 4-23b shows the oxygen K-edge of the HIPIMS samples. Each of the spectra are characteristic to ZnO. The peak in the HIPIMS (inside) spectra is less well resolved and the filtered HIPIMS is more resolved, illustrating the change in disorder between the films. Also shown is the FEFF9 calculation of the ZnO wurtzite phase. Like the magnetron sputtered samples, a close match is observed.

Figure 4-23c shows the XAS in the region of the zinc L-edges for the HIPIMS samples. These spectra are characteristic of the Zn L-edge from ZnO [38]. Like the oxygen K-edge, the crystallographic disorder of the HIPIMS film towards the inside of the sample is reflected in the XANES with less resolved peaks.

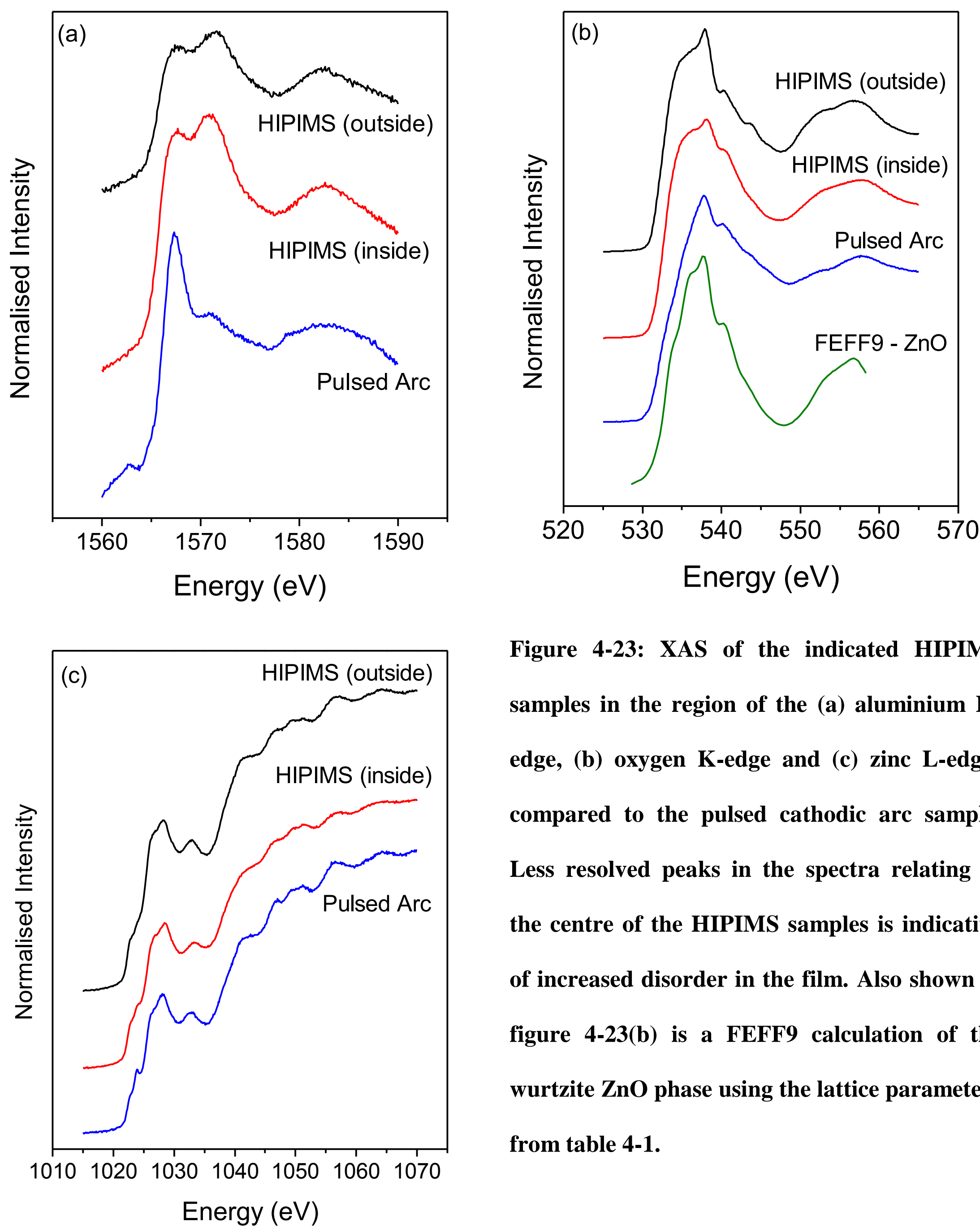

Figure 4-23: XAS of the indicated HIPIMS samples in the region of the (a) aluminium K-edge, (b) oxygen K-edge and (c) zinc L-edges compared to the pulsed cathodic arc sample. Less resolved peaks in the spectra relating to the centre of the HIPIMS samples is indicative of increased disorder in the film. Also shown in figure 4-23(b) is a FEFF9 calculation of the wurtzite ZnO phase using the lattice parameters from table 4-1.

4.6 Filtered HIPIMS

The results for the experiments carried out on the filtered HIPIMS deposited samples are presented in this section. Unlike the magnetron sputtered and HIPIMS samples, visual inspection of the films showed no noticeable variation in the film structure across the surface, suggesting that the samples were homogenous.

4.6.1 Resistivity and Hall Effect

Table 4-11 shows the results of the Hall Effect electrical characterisation experiment for the two films. The immediate effect of the magnetic filter is a higher deposition rate as seen by the increase in film thickness. This suggests that the filter also acts to better focus Zn and Al ions generated at the target towards the substrate. More importantly, there is an increase in carrier concentration (n_e), a dramatic increase in the mobility (μ) and a decrease in the resistivity (ρ) by several orders of magnitude.

Table 4-11: Electrical characteristics for the HIPIMS samples deposited both with and without the inclusion of the straight magnetic filter.

Deposition Method	Thickness (nm)	n_e (cm^{-3})	μ (cm^2/Vs)	ρ (Ωcm^{-1})
HIPIMS	90	5.8×10^{20}	0.553	1.9×10^{-2}
Filtered HIPIMS	180	1.3×10^{21}	6.05	7.9×10^{-4}

4.6.2 Optical transmission

Figure 4-24 shows the transmittance as a function of wavelength for the HIPIMS samples deposited both with and without the magnetic filter. It can be seen that despite being twice as thick, the filtered HIPIMS has a higher transmittance in the optical (400-700 nm) region of the spectrum. This extra thickness of the film has the effect of reducing the transparency in the IR region (as was seen in the pulsed cathodic arc deposited films).

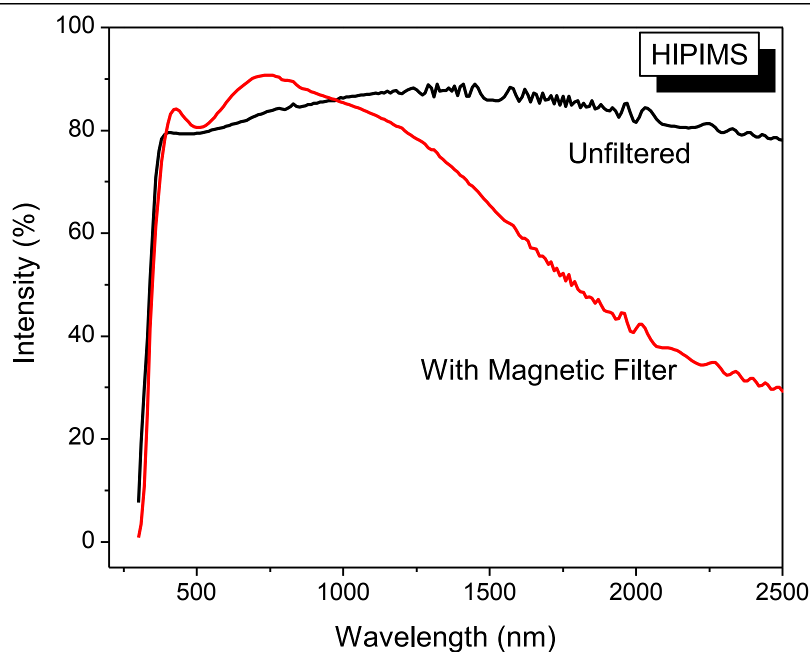

Figure 4-24: Optical transmittance spectra comparison between unfiltered HIPIMS (black) and straight filtered HIPIMS (red)

4.6.3 Composition and microstructure

Figure 4-25 shows the Zn2p, O1s and Al2p binding energy spectra for the HIPIMS sample grown with and without the inclusion of the straight magnetic filter to remove O^- bombardment of the film during growth. The Zn2p and Al2p match well with the spectra for their oxidised states, ZnO and Al_2O_3 respectively [32].

Table 4-12 shows the atomic percentages for each of the zinc, oxygen and aluminium as calculated from the normalised peak area and sensitivity factors. Of particular interest is that the atomic percentages of the filtered sample lies in the midpoint of the 'inner' and 'outer' regions of the film (as was seen in table 4-8). This indicates that the straight filter not only reduces the amount of ion damage to the surface, but also plays a role in how the Al/Zn ions are distributed across the sample surface, as they would also be affected by the magnetron field lines.

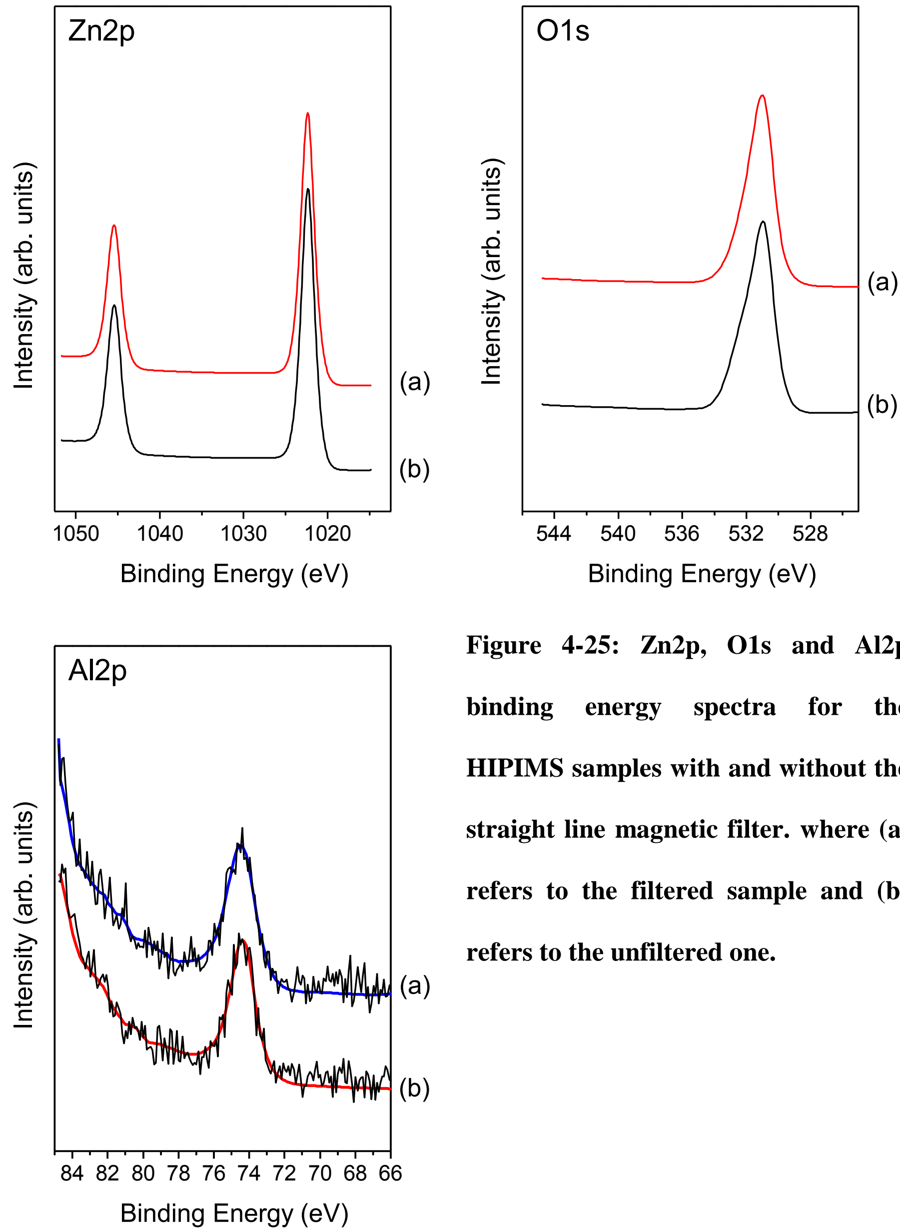

Figure 4-25: Zn2p, O1s and Al2p binding energy spectra for the HIPIMS samples with and without the straight line magnetic filter. where (a) refers to the filtered sample and (b) refers to the unfiltered one.

Table 4-12: Details of the XPS experiment on the static HIPIMS sample. POS3 refers to the inside of the sample, POS1 refers to the outside of the sample

Spectrum	Technique	Thickness (nm)	%Zn	%O	%Al
a	Filtered HIPIMS	180	43.4	50.0	6.6
b	Unfiltered HIPIMS	90	42.9	51.0	6.1

To determine whether any variation existed across the sample of the filtered sample, an XPS line scan was also performed across the surface. Figure 4-22 shows the change in aluminium percentage of the filtered HIPIMS deposited sample across the sample surface using an XPS linescan. The scan runs across the diagonals of the sample from position A to B in the same manner as with the unfiltered HIPIMS which produced figure 4-21. Across the surface of this sample there is no substantial change in the aluminium percentage as with the unfiltered sample, only noise inherent with the low aluminium concentrations. Also plotted in the linescan is a line of best fit, which shows that the average atomic percentage of the aluminium is 4.8%, which is close to that of the cathode material.

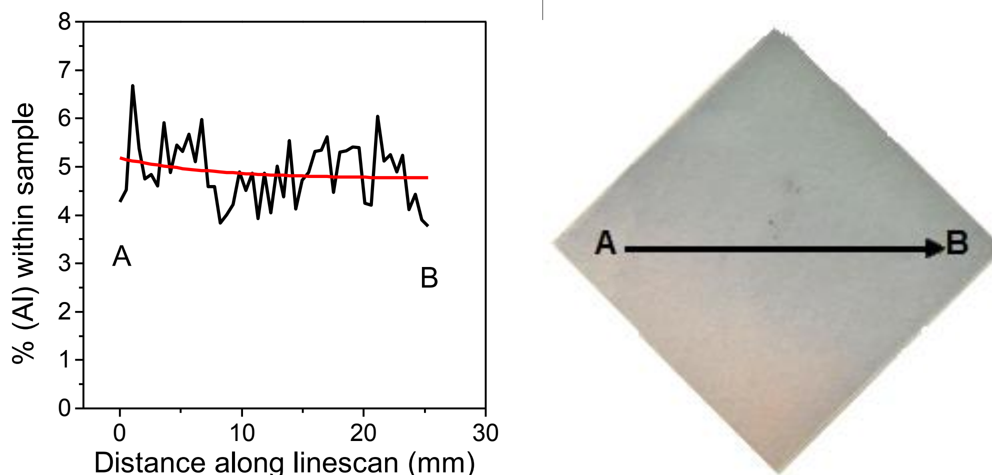

Figure 4-26: XPS line scan of the Al2p peak across the surface of the filtered HIPIMS sample from position A to B.

Figure 4-27 shows the XRD of the HIPIMS samples deposited both with and without the magnetic filter. The peaks in the spectra for the film produced with the filter are more intense and more clearly resolved; indicating that the insertion of the filter gives rise to a greater preferred orientation of the (002) planes (peaks 1 and 2). The sample with the magnetic filter also appears to have additional phases. At $2\theta=33.0^{\circ}$ (peak 3) the hexagonal β-Al_2O_3 peak (ICDD card no. 51-0769) becomes more prominent and trace amounts of the gahnite phase (located at $2\theta=31.1^{\circ}$) are also present. The average grain size was determined using the

Scherrer equation, and the results are shown in table 4-13. It can be seen that by using a straight magnetic filter in the HIPIMS setup, crystallinity is promoted with the growth of larger grains. The XRD of the filtered HIPIMS is similar to that observed from the pulsed cathodic arc sample (figure 4-7), indicating that they have a similar microstructure.

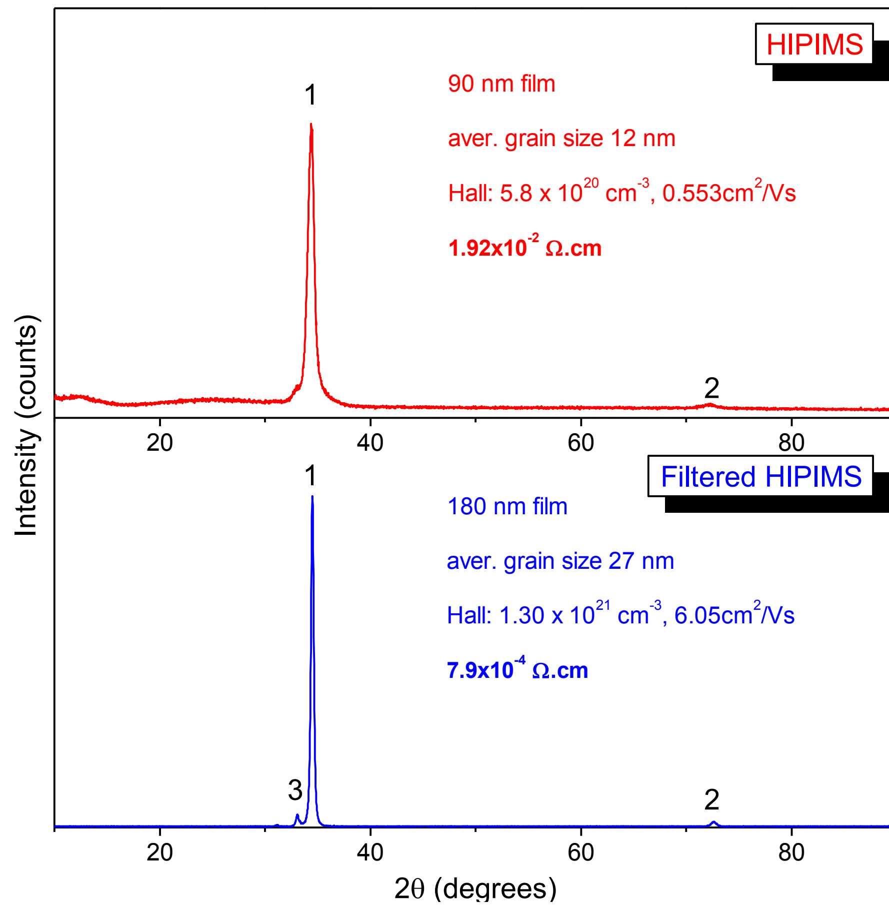

Figure 4-27: XRD comparison between the filtered HIPIMS sample and the HIPIMS sample.

Table 4-13: Peak position and grain size analysis of the AZO samples deposited using magnetron sputtering and HIPIMS.

Sample	Thickness (nm)	$2\theta_B$ (deg)	FWHM (deg)	D (nm)
HIPIMS (filtered)	180	34.50	0.31	27
HIPIMS (unfiltered)	90	34.38	0.68	12

Figure 4-28a shows the XAS in the region of the aluminium K-edge for HIPIMS deposited sample at the regions indicated and the filtered HIPIMS sample. It can be seen that like the other deposition methods, the peak at 1567.7 eV shows the presence of octahedrally coordinated Al within the sample, with no indication of tetrahedrally coordinated Al present. The relative heights of the peaks show that the filtered HIPIMS sample contains more short range order than the unfiltered sample. The inclusion of the filter changes the aluminium K-edge of the HIPIMS spectra in such a way that it begins to approach that of the pulsed arc sample.

Figure 4-28b shows the oxygen K-edge of the HIPIMS samples both with and without the magnetic filter. Each spectrum is characteristic of wurtzite ZnO. The HIPIMS spectrum is less well resolved and the filtered HIPIMS is more resolved, illustrating the change in disorder between the films. Also shown is the FEFF9 calculation of the ZnO wurtzite phase. Like the magnetron sputtered samples, a close match is achieved due to less Zn/Al oxide phases forming.

Figure 4-28c shows the XAS in the region of the zinc L-edges for the HIPIMS samples. These spectra are characteristic of the Zn L-edge from ZnO [38]. Like the oxygen K-edge, the crystallographic disorder of the HIPIMS sample is reflected in the XANES with less resolved peaks.

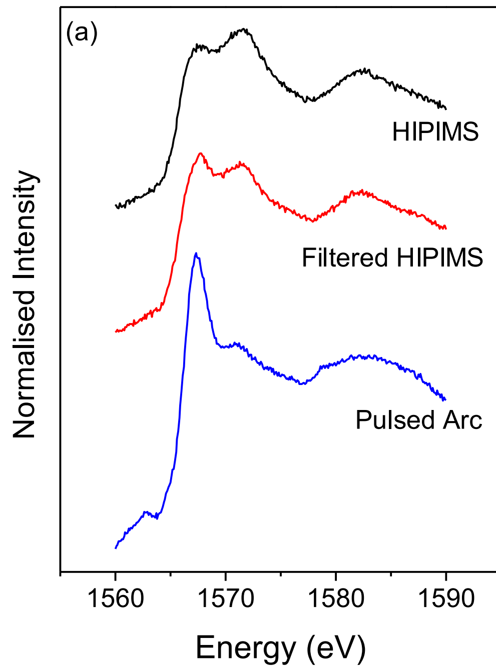

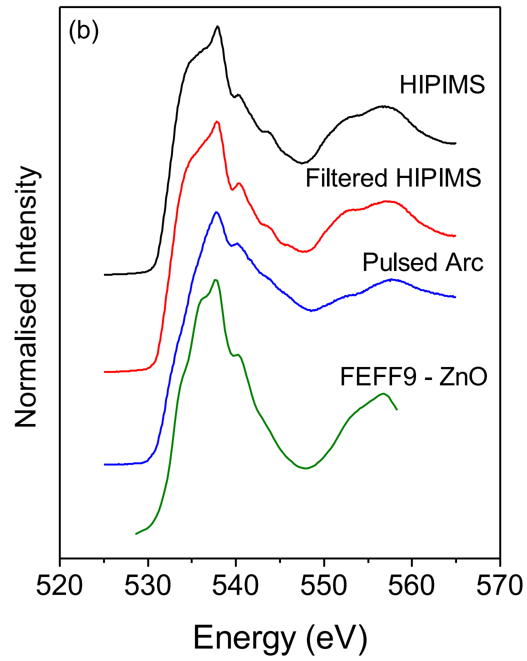

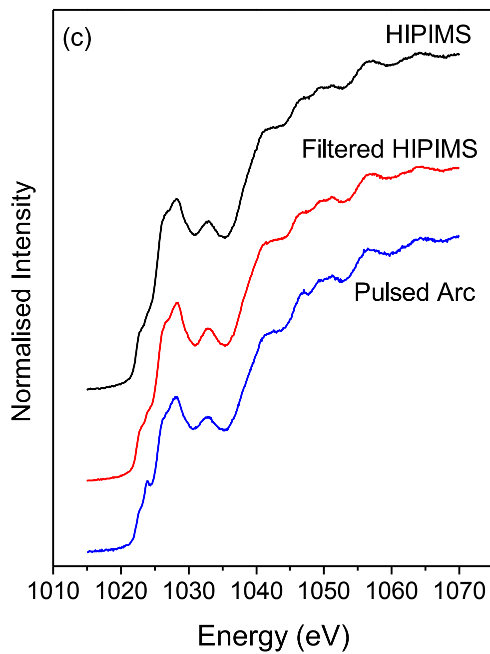

Figure 4-28: XAS of the indicated HIPIMS samples in the region of the (a) aluminium K-edge, (b) oxygen K-edge and (c) zinc L-edges. Less resolved peaks in the spectra relating to the centre of the HIPIMS samples is indicative of increased disorder in the film. Also shown in figure 4-23(b) is a FEFF9 calculation of the wurtzite ZnO phase using the lattice parameters from table 4-1.

4.7 Comparison of techniques

To get a clearer understanding of the difference between the films deposited using these techniques, films of a similar thickness were selected and a comparison for each analysis is made. For the magnetron and HIPIMS coatings, the outer region of the films were selected as they had the best electrical properties.

Table 4-14 shows a comparison of the electrical properties for each of the films. Figure 4-29 shows a graphical representation of the data in this table. Several can be drawn from this data. The first is the comparison between the filtered HIPIMS and the unfiltered of similar thickness. It can be seen that the filtered HIPIMS not only has a lower resistivity (ρ), but also a significantly higher carrier concentration (n_e). As mentioned earlier, it was found that with increasing thickness, a decrease in ρ and an increase in n_e and μ is expected [17, 21, 29]. But with these results, the thinner filtered sample has lower resistivity, indicating that having the straight filter within the HIPIMS setup provides better films electrically, probably due to reduction in O^- ion damage to the growing film.

The second point worth noting is that conventional magnetron has the highest resistivity, approximately double that of the unfiltered HIPIMS sample despite being a much thicker film. This would indicate that using the high power pulses and the highly ionised plasma in HIPIMS results in a superior film.

Finally is that the pulsed cathodic arc sample has a much lower resistivity than all of the other films. The pulsed arc uses a high energy, highly ionised plasma with no macroparticles and few neutral atoms (both due to 90° filter) to grow thin films. This, along with the observation that filtered HIPIMS makes for better films than magnetron sputtering further indicates that an energetic deposition is preferred for making AZO films with low resistivity.

Table 4-14: Comparison of electrical properties for each of the listed deposition methods. Films of similar thickness were chosen so that a fair comparison could be made.

Deposition Method	Thickness (nm)	n_e (cm^{-3})	μ (cm^2/Vs)	ρ (Ωcm^{-1})
Pulsed cathodic arc	260	7.63×10^{20}	33.2	2.46×10^{-4}
Magnetron (POS2)	318	1.56×10^{20}	11.1	3.58×10^{-3}
HIPIMS (POS1)	220	5.10×10^{20}	7.16	1.70×10^{-3}
Filtered HIPIMS	180	1.30×10^{21}	6.05	7.94×10^{-4}

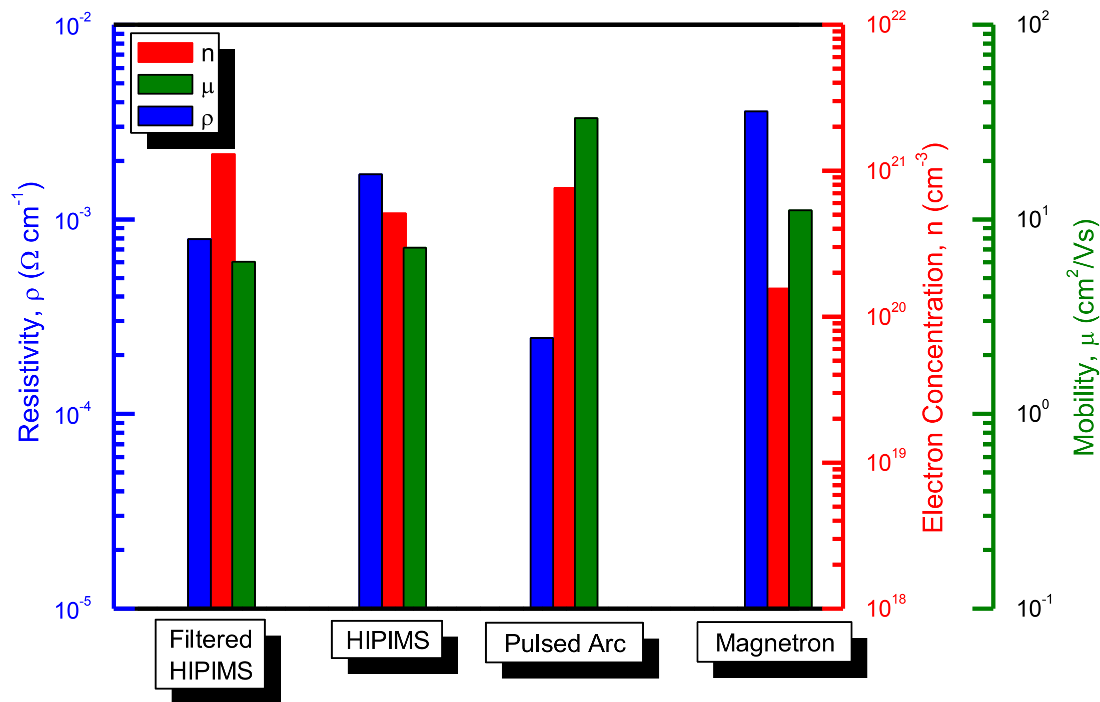

Figure 4-29: Comparison of the electrical properties for the techniques used to deposit the AZO films.

Figure 4-30 shows a comparison of the optical transmission between the (a) magnetron sputtered sample, (b) filtered HIPIMS sample, (c) HIPIMS sample and the (d) pulsed cathodic arc deposited sample of similar thicknesses. At 550 nm, the region of which the eye is most sensitive to light, all samples have a similar transparency. Although the magnetron sample is thicker than the others, it has a higher transmission in both the visible and the infra-red regions of the spectra than all of the other techniques. This is possibly due to film growth being primarily from low energy neutrals (<10 eV) in the conventional magnetron. Like the work

performed by Anders [17], films deposited using an energetic plasma (10-30 eV) have a low resistivity and a low transmittance in the IR region. However, the filtered HIPIMS sample transmits well in the IR region, probably due to it being a thinner film (table 4-14).

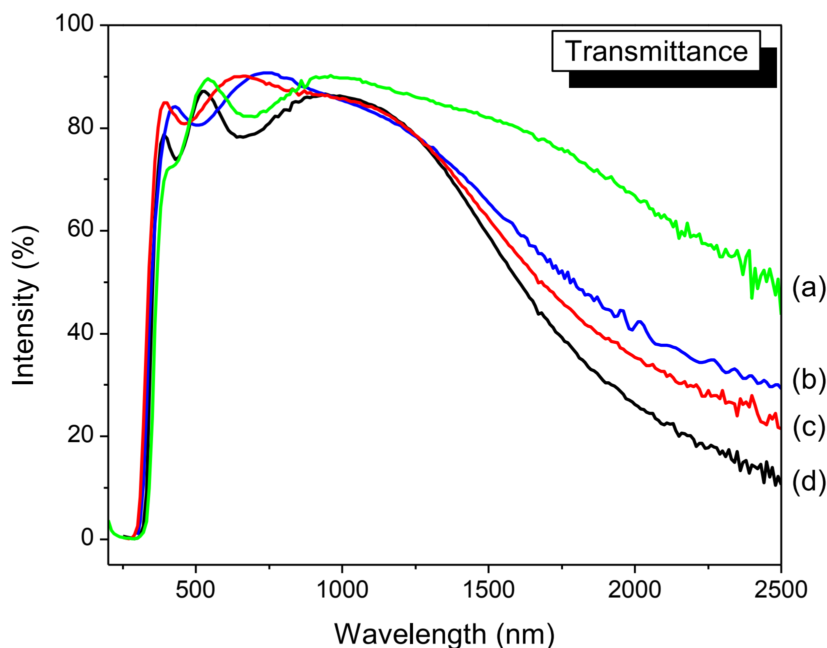

Figure 4-30: Comparison of transmission intensity for AZO films deposited by (a) magnetron sputtering, (b) filtered HIPIMS, (c) HIPIMS and (d) pulsed cathodic arc deposition techniques.

Table 4-14 shows a comparison of the properties of the AZO films collected using XPS and XRD. Shown in the table is a comparison of the atomic percentages found within the film. The two filtered deposition techniques (pulsed cathodic arc and filtered HIPIMS) have a lower atomic percentage of zinc within the films, which is possibly a result of the filtering process.

It can be seen that the HIPIMS sample has significantly smaller grain sizes than the other three deposition methods. This is likely due to the large amount of O^- ion bombardment during the deposition process. The O^- ion damage effect appears to occur less in the magnetron sputtering process in which no significant change in grain size across the surface of the sample was apparent. This is probably due to film growth being primarily from low energy neutrals in the

conventional magnetron. The largest crystals were seen in the filtered HIPIMS and the pulsed cathodic arc depositions. The common element in film deposition between these two techniques is that they both use an energetic plasma directed to the substrate via a magnetic filter. Energetic deposition provides atoms with enough mobility to rearrange into lower energy ordered bonding configurations. A similar phenomenon was observed for WO_3 films in chapter 3 where pulsed cathodic arc deposited films were found to be more crystalline than those deposited by magnetron sputtering.

Table 4-15: Comparison of microstructural properties of the deposited AZO films.

Deposition Method	Thickness (nm)	%Zn	%O	%Al	ZnO(002) 2θ	Grain size (nm)
Pulsed cathodic arc	260	52.5	43.8	3.7	34.7	32
Magnetron (POS2)	310	47.9	47.9	4.2	34.5	23
HIPIMS (POS1)	220	44.9	50.3	4.9	34.1	9
Filtered HIPIMS	180	43.4	50.0	6.6	34.5	27

XAS was used to better understand of the bonding dynamics of the films. The peak located at approximately 1567.4 eV is characteristic of distorted octahedral coordination (AlO_6, with 6 fold symmetry) of the aluminium atoms with the surrounding oxygen environment. This peak appeared in each of the samples, but at varying intensities depending on the deposition method. The pulsed arc deposition coating, where little ion damage has occurred, had the strongest short range order. In contrast to this, the centre of the HIPIMS deposited film which is the sample with the highest amount of ion damage had the lowest short range order. These results show that methods with a higher degree of ion bombardment have reduced octahedral symmetry reflecting decreased order in the films.

4.7 Conclusions

In this chapter, a comparison was made between AZO films prepared using pulsed cathodic arc, magnetron sputtering and HIPIMS. The pulsed cathodic arc films were found to contain mainly the wurtzite ZnO phase with the crystals strongly <001> oriented in the direction perpendicular to the substrate. Also present in the films were a hexagonal aluminium oxide (Al_2O_3) phase and traces of the gahnite phase ($ZnAl_2O_4$, identified using XRD). This indicates that not all of the aluminium was substituting into the zinc atom positions. The pulsed arc samples were found to have good electrical properties, with low resistivities and high carrier concentrations even for quite thin films. The films displayed favourable optical properties, with transmissions of approximately 85% found in the visible region.

On visual inspection of the magnetron sputtered films, there appeared to be variations in the colour across the surface. Even though the microstructure of the films did not appear to change across the surface, the electrical and optical properties changed dramatically. In particular, the area of the film in line with the centre of the magnetron was found to have inferior resistivities, orders of magnitude higher than the outside of the film. These results indicate the presence of O^- ions bombarding the films during reactive deposition which had a major impact on the electrical and optical properties. The increase in power inherent with the HIPIMS process was found to exacerbate the problem of ion bombardment with large variations in the optical and electrical properties found across the surface of films prepared using this technique. Unlike magnetron sputtering, the change in film across the surface was also reflected in the microstructure with x-ray analysis revealing a significant reduction in crystallinity and composition in line with the centre of the magnetron.

The inclusion of a magnetic filter between the magnetron and the sample had the effect of removing the majority of the damaging ions, allowing for a more crystalline film to grow with

enhanced optical and electrical properties. The use of such filters may therefore help overcome one of the major disadvantages of the HIPIMS techniques which has been low deposition rates. The microstructure of the film prepared using the filter was found to be similar to that deposited using the pulsed cathodic arc. These results suggest that the optimal conditions for AZO film growth are with energetic ions which provide mobility to the deposited atoms allowing them to rearrange into more ordered arrangements. The use of the straight filter also had the side benefit of increasing the HIPIMS deposition rate by better directing the Zn and Al ions from the target towards the substrate.

4.8 Bibliography

1. Minami, T., *Present status of transparent conducting oxide thin-film development for Indium-Tin-Oxide (ITO) substitutes.* Thin Solid Films, 2008. **516**(17): p. 5822-5828.
2. Harrison, S.E., *Conductivity and Hall Effect of ZnO at Low Temperatures.* Physical Review, 1954. **93**(1): p. 52.
3. Mohanty, G.P. and L.V. Azaroff, *Electron Density Distributions in ZnO Crystals.* The Journal of Chemical Physics, 1961. **35**(4): p. 1268-1270.
4. Ritchie, I.M. and R.K. Tandon, *Some doping studies on the oxidation of zinc in the temperature range 200-390°C.* Surface Science, 1970. **22**(1): p. 199-215.
5. McKeown, D.A., *Aluminum X-ray absorption near-edge spectra of some oxide minerals: Calculation versus experimental data.* Physics and Chemistry of Minerals, 1989. **16**(7): p. 678-683.
6. Karzel, H., W. Potzel, ouml, M. fferlein, W. Schiessl, M. Steiner, U. Hiller, G.M. Kalvius, D.W. Mitchell, T.P. Das, P. Blaha, K. Schwarz, and M.P. Pasternak, *Lattice dynamics and hyperfine interactions in ZnO and ZnSe at high external pressures.* Physical Review B, 1996. **53**(17): p. 11425.
7. Minami, T., T. Yamamoto, and T. Miyata, *Highly transparent and conductive rare earth-doped ZnO thin films prepared by magnetron sputtering.* Thin Solid Films, 2000. **366**(1-2): p. 63-68.
8. Thu, T.V. and S. Maenosono, *Synthesis of high-quality Al-doped ZnO nanoink.* Journal of Applied Physics, 2010. **107**(1): p. 014308-6.
9. Ashrafi, A.B.M.A., A. Ueta, A. Avramescu, H. Kumano, I. Suemune, Y.-W. Ok, and T.-Y. Seong, *Growth and characterization of hypothetical zinc-blende ZnO films on GaAs(001) substrates with ZnS buffer layers.* Applied Physics Letters, 2000. **76**(5): p. 550-552.
10. Ozgur, U., Y.I. Alivov, C. Liu, A. Teke, M.A. Reshchikov, S. Dogan, V. Avrutin, S.-J. Cho, and H. Morkoc, *A comprehensive review of ZnO materials and devices.* Journal of Applied Physics, 2005. **98**(4): p. 041301.
11. Look, D.C., R.L. Jones, J.R. Sizelove, N.Y. Garces, N.C. Giles, and L.E. Halliburton, *The path to ZnO devices: donor and acceptor dynamics.* physica status solidi (a), 2003. **195**(1): p. 171-177.
12. Park, C.H., S.B. Zhang, and S.-H. Wei, *Origin of p-type doping difficulty in ZnO: The impurity perspective.* Physical Review B, 2002. **66**(7): p. 073202.
13. Tsujino, J., N. Homma, T. Sugawara, I. Shimono, and Y. Abe, *Preparation of Al-doped ZnO thin films by RF thermal plasma evaporation.* Thin Solid Films, 2002. **407**(1-2): p. 86-91.

14. Miyazaki, M., K. Sato, A. Mitsui, and H. Nishimura, *Properties of Ga-doped ZnO films.* Journal of Non-Crystalline Solids, 1997. **218**: p. 323-328.
15. Shinde, S.S. and et al., *Optoelectronic properties of sprayed transparent and conducting indium doped zinc oxide thin films.* Journal of Physics D: Applied Physics, 2008. **41**(10): p. 105109.
16. Rousset, J., E. Saucedo, and D. Lincot, *Extrinsic Doping of Electrodeposited Zinc Oxide Films by Chlorine for Transparent Conductive Oxide Applications.* Chemistry of Materials, 2009. **21**(3): p. 534-540.
17. Anders, A., S.H.N. Lim, K.M. Yu, J. Andersson, J. Rosén, M. McFarland, and J. Brown, *High quality ZnO:Al transparent conducting oxide films synthesized by pulsed filtered cathodic arc deposition.* Thin Solid Films, 2010. **518**(12): p. 3313-3319.
18. Lim, D.G., D.H. Kim, J.K. Kim, O. Kwon, K.J. Yang, K.I. Park, B.S. Kim, S.W. Lee, M.W. Park, and D.J. Kwak, *Improved electrical properties of ZnO:Al transparent conducting oxide films using a substrate bias.* Superlattices and Microstructures, 2006. **39**(1-4): p. 107-114.
19. Lin, S.-S., J.-L. Huang, and P. Sajgalik, *The properties of heavily Al-doped ZnO films before and after annealing in the different atmosphere.* Surface and Coatings Technology, 2004. **185**(2-3): p. 254-263.
20. Lu, J.G., Z.Z. Ye, Y.J. Zeng, L.P. Zhu, L. Wang, J. Yuan, B.H. Zhao, and Q.L. Liang, *Structural, optical, and electrical properties of (Zn,Al)O films over a wide range of compositions.* Journal of Applied Physics, 2006. **100**(7): p. 073714-11.
21. Schuler, T. and M.A. Aegerter, *Optical, electrical and structural properties of sol gel ZnO:Al coatings.* Thin Solid Films, 1999. **351**(1-2): p. 125-131.
22. Murdoch, G.B., S. Hinds, E.H. Sargent, S.W. Tsang, L. Mordoukhovski, and Z.H. Lu, *Aluminum doped zinc oxide for organic photovoltaics.* Applied Physics Letters, 2009. **94**(21): p. 213301-3.
23. Saarenpää, H., T. Niemi, A. Tukiainen, H. Lemmetyinen, and N. Tkachenko, *Aluminum doped zinc oxide films grown by atomic layer deposition for organic photovoltaic devices.* Solar Energy Materials and Solar Cells, 2010. **94**(8): p. 1379-1383.
24. Xu, J., H. Wang, L. Yang, M. Jiang, S. Wei, and T. Zhang, *Low temperature growth of highly crystallized ZnO:Al films by ultrasonic spray pyrolysis from acetylacetone salt.* Materials Science and Engineering: B, 2010. **167**(3): p. 182-186.
25. Mraz, S. and J.M. Schneider, *Energy distribution of O^- ions during reactive magnetron sputtering.* Applied Physics Letters, 2006. **89**(5): p. 051502-3.
26. Bilek, M.M.M., M.M.M. Bilek, R.N. Tarrant, D.R. McKenzie, S.H.N.A.L.S.H.N. Lim, and D.G.A.M.D.G. McCulloch, *Control of stress and microstructure in cathodic arc deposited films.* Plasma Science, IEEE Transactions on, 2003. **31**(5): p. 939-944.
27. Brown, I.G., *Cathodic arc deposition of films.* Annual Review of Materials Science, 1998. **28**(1): p. 243-269.
28. Anders, A., R.A. MacGill, and T.A. McVeigh, *Efficient, compact power supply for repetitively pulsed, ``triggerless'' cathodic arcs.* Review of Scientific Instruments, 1999. **70**(12): p. 4532-4535.
29. Tseng, Y.-K., G.-J. Gao, and S.-C. Chien, *Synthesis of c-axis preferred orientation ZnO:Al transparent conductive thin films using a novel solvent method.* Thin Solid Films, 2010. **518**(22): p. 6259-6263.
30. Hullavarad, S., N. Hullavarad, D. Look, and B. Claflin, *Persistent Photoconductivity Studies in Nanostructured ZnO UV Sensors.* Nanoscale Research Letters, 2009. **4**(12): p. 1421-1427.
31. Mar, L.G., P.Y. Timbrell, and R.N. Lamb, *An XPS study of zinc oxide thin film growth on copper using zinc acetate as a precursor.* Thin Solid Films, 1993. **223**(2): p. 341-347.
32. Scofield, J.H., *Hartree-Slater subshell photoionization cross-sections at 1254 and 1487 eV.* Journal of Electron Spectroscopy and Related Phenomena, 1976. **8**(2): p. 129-137.

33. Labidi, A., C. Jacolin, M. Bendahan, A. Abdelghani, J. Guérin, K. Aguir, and M. Maaref, *Impedance spectroscopy on WO_3 gas sensor.* Sensors and Actuators B: Chemical, 2005. **106**(2): p. 713-718.
34. Dasgupta, N.P., S. Neubert, W. Lee, O. Trejo, J.-R. Lee, and F.B. Prinz, *Atomic Layer Deposition of Al-doped ZnO Films: Effect of Grain Orientation on Conductivity.* Chemistry of Materials, 2010. **22**(16): p. 4769-4775.
35. Fang, G. and et al., *Magnetron sputtered AZO thin films on commercial ITO glass for application of a very low resistance transparent electrode.* Journal of Physics D: Applied Physics, 2002. **35**(23): p. 3096.
36. Ildefonse, P., D. Cabaret, P. Sainctavit, G. Calas, A.M. Flank, and P. Lagarde, *Aluminium X-ray absorption Near Edge Structure in model compounds and Earth's surface minerals.* Physics and Chemistry of Minerals, 1998. **25**(2): p. 112-121.
37. Chen, J.G., *NEXAFS investigations of transition metal oxides, nitrides, carbides, sulfides and other interstitial compounds.* Surface Science Reports, 1997. **30**(1-3): p. 1-152.
38. Mizoguchi, T., I. Tanaka, S. Yoshioka, M. Kunisu, T. Yamamoto, and W.Y. Ching, *First-principles calculations of ELNES and XANES of selected wide-gap materials: Dependence on crystal structure and orientation.* Physical Review B, 2004. **70**(4): p. 045103.
39. Stadelmann, P., *JEMS Java Electron Microscopy Software*, Available from: http://cimewww.epfl.ch/people/stadelmann/jemsWebSite/jems.html.

Chapter 5

The microstructure and electrical properties of hafnium oxide prepared using filtered cathodic vacuum arc

In this chapter hafnium oxide (HfO_2) films were deposited with a range of substrate biases and substrate temperatures using a filtered cathodic vacuum arc (FCVA) deposition system. The microstructure, electronic structure and electrical breakdown of the films were characterised. Diffraction and the near edge structure (NES) measurements of the oxygen K-edge were used to determine the phase present. The goal was to determine the optimal growth conditions to produce HfO_2 films with the best electrical breakdown characteristics.

5.1 Introduction

5.1.1 Hafnium oxide as a dielectric

The drive to decrease feature sizes in microelectronics has led to the gate oxide thickness in silicon devices approaching its fundamental limit [1, 2]. Silicon dioxide (SiO_2) has been used as the gate material in transistors for decades and is constantly being made thinner to improve performance by increasing the gate capacitance [3, 4]. However with decreasing SiO_2 size, undesirable leakage current due to tunnelling through the device is increased, compromising device performance by increasing power consumption and reducing reliability. Replacing SiO_2 with a material with a higher dielectric constant (for example HfO_2, ZrO_2 or TiO_2) has potential to increase the gate capacitance with decreased thickness and significantly reduced leakage currents [2].

Hafnium oxide (HfO_2) is a particularly promising replacement for SiO_2 due to its high dielectric constant, wide bandgap and low leakage characteristics [5, 6]. Figure 5-1 shows a schematic of HfO_2 acting as a gate dielectric between the gate which has a potential applied to it and a field effect transistor substrate (silicon in this case). When a large enough potential is supplied between the gate (HfO_2) and body (Si) terminals, a 'channel', also known as an inversion layer, forms between the dielectric material and the body. This channel provides a current path between source and the drain electrodes which can be switched on/off using the potential applied to the gate. The 'source' is the aptly named source of the charge carriers which pass through the channel and exit via the 'drain'. These regions can either be p-type or n-type, but must be the opposite type to the body region (silicon can be doped to choose a particular type). In the case of a p-type MOS, the source is a 'p+' region and contains electron holes, in the case of an n-type MOS the source is an 'n+' region and supplies electrons for the channel.

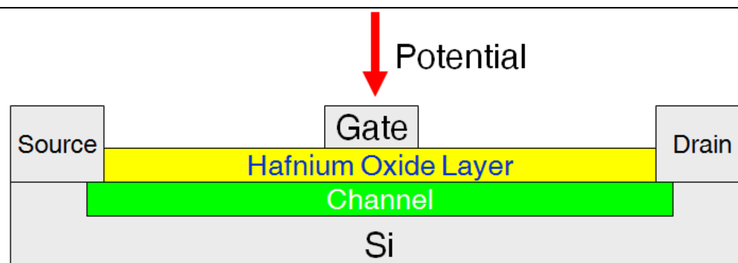

Figure 5-1: Schematic of HfO_2 acting as a gate dielectric in a field effect transistor device

5.1.2 Crystal structure of HfO_2

Experimentally, the monoclinic phase has been found to be the naturally occurring stable phase of HfO_2 [7-10]. However, three other HfO_2 phases have been indentified [9, 11-13] as shown in figure 5-2. With increasing temperature, the symmetry of the crystals increase and the axes become orthogonal. The first phase transformation leads to a tetragonal structure with space group $P4_2/nmc$. Finally a phase transformation to the cubic structure (spacegroup Fm3m) occurs at the highest temperatures. Both the tetragonal and cubic phases have been observed in thin films [11, 12]. However it can be difficult to distinguish the cubic phase from the tetragonal phase due to the similarity of their lattice parameters (see table 5-1).

Using first principles density functional theory, Zhao et al [14] also found that at low temperatures HfO_2 prefers to form a monoclinic structure with space group $P2_1/c$. Phase transformations to the tetragonal and cubic phases were shown to occur with increased temperatures. The lattice parameters for each these calculated phases are shown in table 5-1. An orthorhombic phase of HfO_2 has also been found in calculations in which unit cells were subjected to pressures of 4-10 GPa [13].

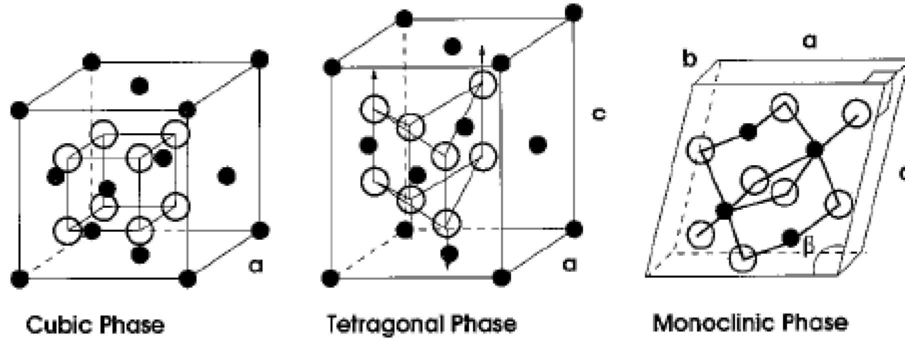

Figure 5-2: The three ambient pressure phases of HfO_2 adapted from Zhao et. al [14].

Table 5-1: Lattice parameters of the ambient pressure phases calculated using GGA by Zhao et. al [14] as well as their formation temperature. Also shown is the high pressure phase calculated by Lowther et al.

Symmetry	Space Group	Lattice Parameters	Bulk Formation
Orthorhombic	Pbca	a=9.54 Å b=5.17 Å c=4.94 Å	4-10 GPa [13]
Cubic	Fm3m	a=5.248 Å	2600 ºC [9, 14]
Tetragonal	$P4_2/nmc$	a=5.299 Å c=5.373 Å	1720 ºC [9, 14]
Monoclinic	$P2_1/c$	a=5.291 Å b=5.405 Å c=5.366 Å β= 97.92°	Room temperature [9, 14]

5.1.3 Hafnium oxide films

It is commonly accepted that a polycrystalline microstructure provides worse breakdown performance than an amorphous microstructure due to the possibility of leakage paths along crystal grain boundaries [15-18]. Hergenrother et al [19] have shown that polycrystalline films prepared using ALD have extremely low leakage current densities when used in MOS field effect transistors. It has also been shown that hafnium oxide films with increased crystallinity

have higher dielectric constants [15]. It is therefore important to understand, for a particular synthesis technique, the relationship between the deposition conditions on the microstructure and the breakdown characteristics of the HfO_2 thin films.

Ho et al [20] found that polycrystalline films prepared by atomic layer deposition (ALD) with large uniform grain size may be preferable. It is suggested that this will help minimise the variations in the effective electric field experienced by carriers in the underlying channel. XRD was performed to determine the phase of the crystals deposited using ALD and to determine the average crystal size. It is found that with increasing deposition temperature that the intensity of the monoclinic peaks increases, while the peaks of other unknown phases disappear. It was noted that more work was necessary to determine whether the other phases are tetragonal or orthorhombic. This study could potentially have used a combination of *ab initio* calculations and a study of the near edge structure to differentiate between the phases.

Techniques which can produce dense flat HfO_2 films with fine grain structure are desirable. With these properties in mind, ALD [21], pulsed laser deposition (PLD) [22, 23], chemical vapour deposition (CVD) [24] and electron beam evaporation [25] have all been employed to produce HfO_2 films.

In the work by Ratzke et al [22] PLD was used to deposit HfO_2 films. PLD produces a similar energetic plasma to cathodic arc, by using a laser to produce an explosive emission of ions and neutrals from the surface of the cathode material. Ratzke found that during deposition, what appeared to be large macroparticle 'splashes' were forming on the surface of the sample. The diameter of the splashes appeared to be dependent on the wavelength of the laser with average size of 0.6 μm, 0.7 μm and 1.0 μm for wavelengths of 355 nm, 532 nm and 1064 nm respectively. A similar study was later performed by Filipescu [26] who also deposited hafnium oxide films using PLD. A more thorough investigation was performed with both the

microstructure and the electrical breakdown studied. The HfO_2 films displayed low leakage currents, had an amorphous microstructure and was both smooth and uniform.

Despite all the work preformed to date, it still remains a challenge to produce low leakage hafnium oxide coatings on silicon without interfacial layers, particularly SiO_2, which tend to form at the metal-oxide/silicon interface [5, 27]. Little work has been done on the synthesis of HfO_2 films by FCVA despite the fact that the technique has been shown to produce dense flat films with easily controllable thickness [28, 29].

In this chapter, HfO_2 thin films are deposited using an FCVA. It has already been shown that varying the temperature or substrate bias during deposition can alter the microstructure and physical properties of films prepared by FCVA deposition [28, 29]. Given that changes in crystallinity may alter the leakage current through the films, the effect of substrate temperature and bias are investigated. The microstructure and electronic structure of the films are studied to investigate which films give the best electrical breakdown (leakage) characteristics.

5.2 Experimental techniques

All hafnium oxide films were deposited onto p-type <100> silicon substrates ($\rho < 10$ Ωcm) which were cleaned using acetone and ethanol prior to insertion into the system. Details of the FCVA system used for the depositions can be found in section 2.1.2. A 99.9 % purity, 70 mm diameter hafnium metal cathode source was operated with an arc current of 140 A. Oxygen gas was bled directly into the chamber and the flow rate was controlled using a mass flow controller (MFC). A second MFC was used to control the flow of argon gas into the cathode chamber in order to stabilise the plasma and reduce oxidation of the cathode [30]. The system was pumped to a base pressure of less than 1×10^{-5} Torr before each deposition. A constant flow of argon gas (5 ml/min) and oxygen gas (20 ml/min) was utilised during the 2 minute long deposition, each with partial pressures of 0.21 mTorr and 0.75 mTorr respectively. This gas mix

was found to reliably produce stoichiometric films . The plasma was initiated and run onto the shutter for 2 minutes to remove any surface contaminants from the cathode. Depositions were then performed in 2 minute intervals (2-minutes on, 2 minutes off) to reduce cathode heating.

For each deposition, both a thick and thin coating was produced. The thicker coatings (~100 nm) were used for cross-sectional TEM analysis, while the thin coatings (20-40 nm) were used for electrical measurements. A pen mark (<1 mm^2 in area) was placed into the corner of the substrate before deposition, and was later wiped off so that step height analysis using a profilometer could be performed on the samples to determine the film thickness. The deposition rate was determined to be 15 nm/min. Two sets of films were produced. The first set (section 5.3) was deposited at room temperature and different substrate biases which, as discussed in section 2.1.2, changes the energy of the depositing plasma. The second set of samples (section 5.4) were deposited at floating bias and at various substrate temperatures using a heating stage (discussed in section 2.1.2) .

5.3 The effect of substrate bias on hafnium oxide films synthesised using FCVA

In this section the results for the hafnium oxide films synthesised with increasing substrate bias during deposition is presented. Substrates at floating potential, -100 V and -500 V were used during deposition and the resulting film microstructure and electrical breakdowns were determined.

5.3.1 X-ray photoelectron spectroscopy (XPS)

XPS was performed on the films using a Thermo Scientific K-Alpha spectrometer with an Al anode x-ray source (see section 2.2.3). An HfO_2 powder standard (Sigma-Aldrich, monoclinic HfO_2, product: 51310) was used to calibrate the sensitivity factors prior to the measurements. A 400μm spot size was used with a pass energy of 50 eV in the regions of the hafnium 4f and

oxygen 1s binding energy spectra. Figures 5-3 and 5-4 show the Hf4f and O1s XPS spectra for the indicated substrate biases. The Hf4f spectra are made up of a doublet, comprised of the 4f7 and 4f5 peaks at 17.2 eV and 18.6 eV respectively, typical of a single HfO_2 species [31]. Small changes in these peak positions are attributed to sample charging during the XPS experiment. The O1s spectra is made up of a combination of two peaks. The first is located at approximately 530 eV and is representative of the oxygen bonded to hafnium in the form of HfO_2 [32, 33]. The second peak is located at 532 eV and is due to surface oxygen/carbon remaining on the surface after the sputter clean [34]. Table 5-2 shows the atomic percentages of the films calculated using the normalised peak area and the film thicknesses. Each of the films is close to stoichiometric HfO_2.

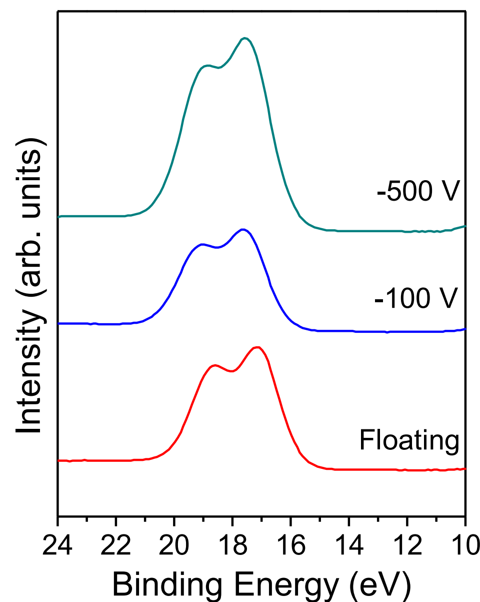

Figure 5-3: XPS spectra of the HfO_2 films with the indicated substrate biases in the region of the hafnium 4f binding energy peaks.

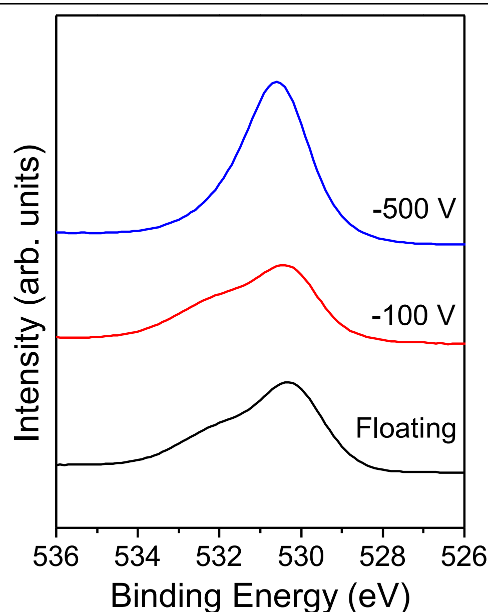

Figure 5-4: XPS spectra of the HfO_2 films with the indicated substrate bias's in the region of the oxygen 1s binding energy peak.

Table 5-2: Atomic percentage of the HfO_2 films with increasing substrate bias during deposition determined using XPS. Each of the deposited films was found to be close to stoichiometric HfO_2.

Substrate Bias	Thickness (nm)	At% (Hf)	At% (O)
Floating	120	34±1	66±1
-100 V	60	33±1	67±1
-500 V	90	34±1	66±1

5.3.2 Film topography

During deposition it was noted that with the -100 V and -500 V samples, electrical arcing appeared across the sample, indicating that charging effects were occurring due to an insulating surface. Inspection of the sample surfaces using an SEM illustrated that the films deposited using a floating potential (Figure 5-5a) and -100 V (Figure 5-5b) were extremely flat and uniform. Atomic force microscopy (AFM) was performed to determine the roughness of the films over a 500 × 500 μm^2 area and to determine typical defect density and size (figure 5-6). All of the films deposited at floating bias and -100 V exhibited a RMS

roughness of less than 2 % of the total deposited film thickness. Defects with a large range of feature sizes appeared in the sample deposited with -500 V bias. Craters up to approximately 100 μm in diameter were observed in the SEM images (Figure 5-5c).

At higher resolutions small pin-holes of the order of 10 nm in diameter were revealed (Figure 5-6c). The craters can be attributed to charging/discharging of the substrate during film deposition, the effects of which (electrical arcing across the sample surface) were observed during deposition through a window. Energy dispersive spectroscopy revealed that the craters in the films were composed mostly of the silicon substrate. It is believed that with high negative substrate bias, the electric field across the film increases during deposition until local breakdown occurs causing damage to the film and underlying silicon. The pin-holes probably arise either from smaller breakdown events or densification of the film during growth and were only found in the film deposited at -500 V substrate bias.

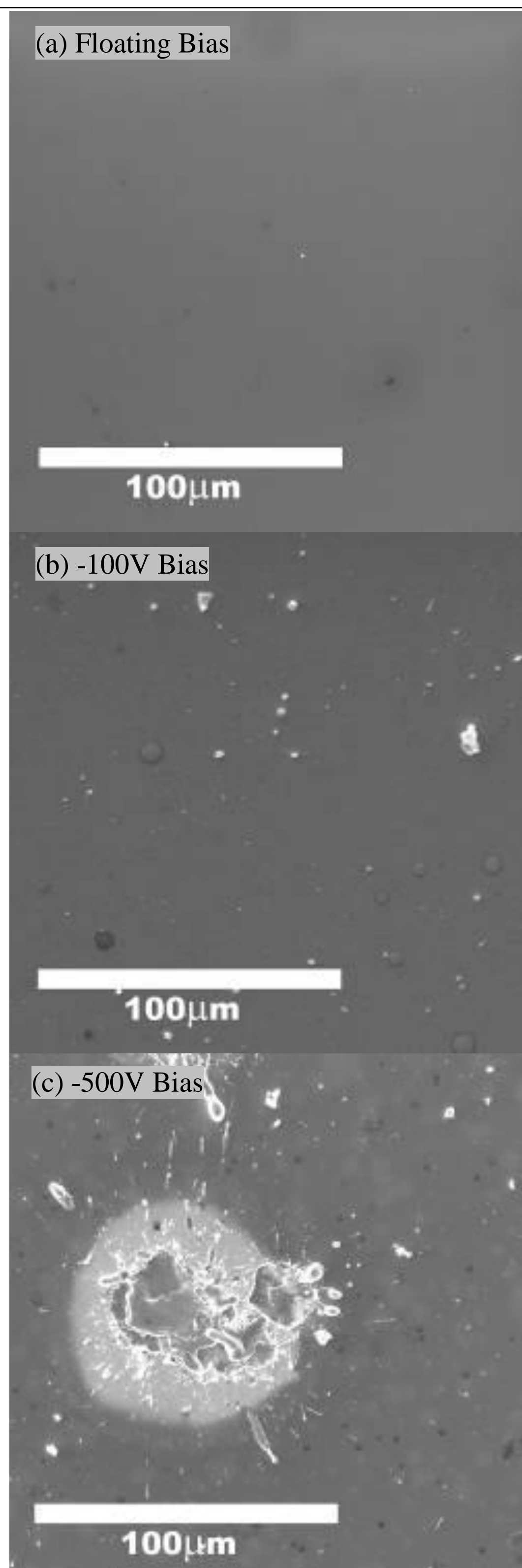

Figure 5-5: SEM images of the HfO_2 bias series with a (a) floating potential, (b) -100 V bias and a (c) -500 V bias.

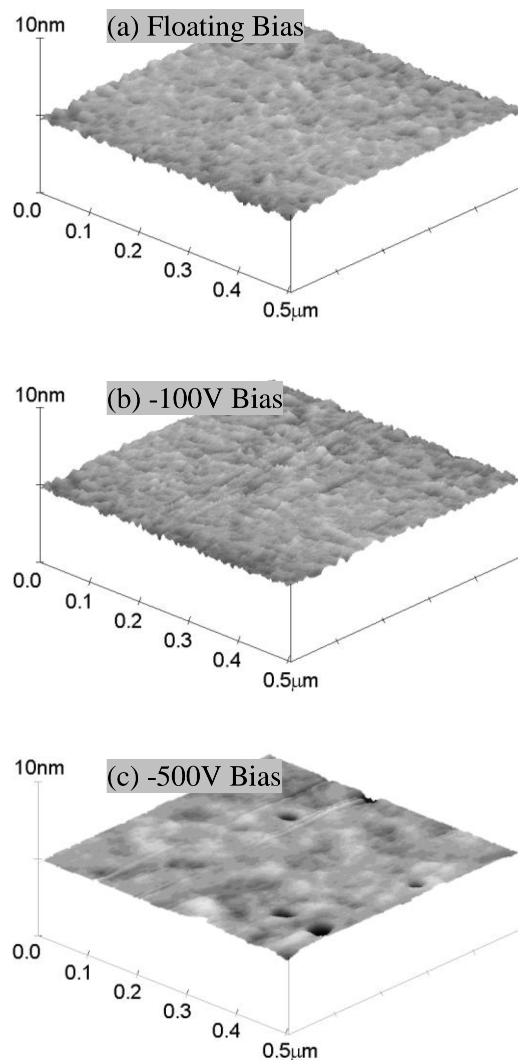

Figure 5-6: AFM images of the bias series of HfO_2 films deposited using FCVA deposited with a (a) floating potential, (b) -100 V bias and a (c) -500 V bias.

5.3.3 Transmission electron microscopy (TEM)

TEM was performed using a JEOL2010 TEM operating at 200kV. Diffraction patterns were collected by first orienting the sample with the electron beam using the silicon substrate <100> pattern as a guide to when the sample is perpendicular to the electron beam. Imaging was performed digitally using a Gatan imaging filter (GIF) and the selected area diffraction patterns were taken on electron sensitive film. Figure 5-7 shows bright field cross sectional TEM (X-TEM) images of films deposited at (a) floating potential, (b) −100 V and (c) −500 V. The silicon substrate appears on the right in each image. Note that the entire film thickness is not

present in the images due to slight overthinning during sample preparation. Also present, particularly near the sample edge, are small (<5 nm) pore-like features caused by the ion-beam thinning process.

The films deposited with floating potential (Fig. 5-7a) and with −100 V bias (Fig. 5-7b) appear isotropic with no evidence for crystallites with lengths greater than 1 nm. The accompanying selected area electron diffraction (SAED) patterns (shown as insets) confirm that the films are highly disordered and fine grained. The two main diffraction rings occur at approximately d = 2.7 Å and d = 1.6 Å (indicated in Fig. 5-6a). The broad rings make it difficult to index these patterns, however, they are consistent with the (011) reflection and a combination of the (120) and (211) reflections of monoclinic $P2_1/c$ HfO_2.

The film deposited with −500 V bias (Fig. 5-7c) shows three distinct layers. The layer closest to the substrate again appears largely amorphous but large crystallites are seen within the matrix. This layer terminates at a thickness of approximately 25 nm with a lighter boundary approximately 2 nm in width. Above this boundary, the structure appears amorphous and similar to that observed in the films deposited with floating potential and −100 V bias. It is believed that during the deposition the surface potential of the silicon substrate was initially equal to the substrate bias voltage, and film growth proceeded with average ion energies of approximately 500 eV. This increased ion energy caused increased mobility resulting in growth of the crystallites seen in the amorphous matrix [35]. As discussed above, the deposition was paused after 2 min in order to reduce cathode heating and the location of the light boundary layer corresponds with the film depth at which the pause occurred. Upon recommencing the deposition, the surface potential appears to have been reduced, as the amorphous structure created using low substrate bias is once again observed in the film.

An interfacial layer of SiO_2 is formed between the silicon substrate and the HfO_2 film. The thickness of the SiO_2 layer was found to be approximately 2, 3.5 and 5 nm for the floating

sample, −100 V bias sample and −500 V biased sample, respectively. This thickness variation in the native oxide can be attributed to oxygen bombardment during the initial stages of film growth, with implantation depths that increase with the applied substrate bias.

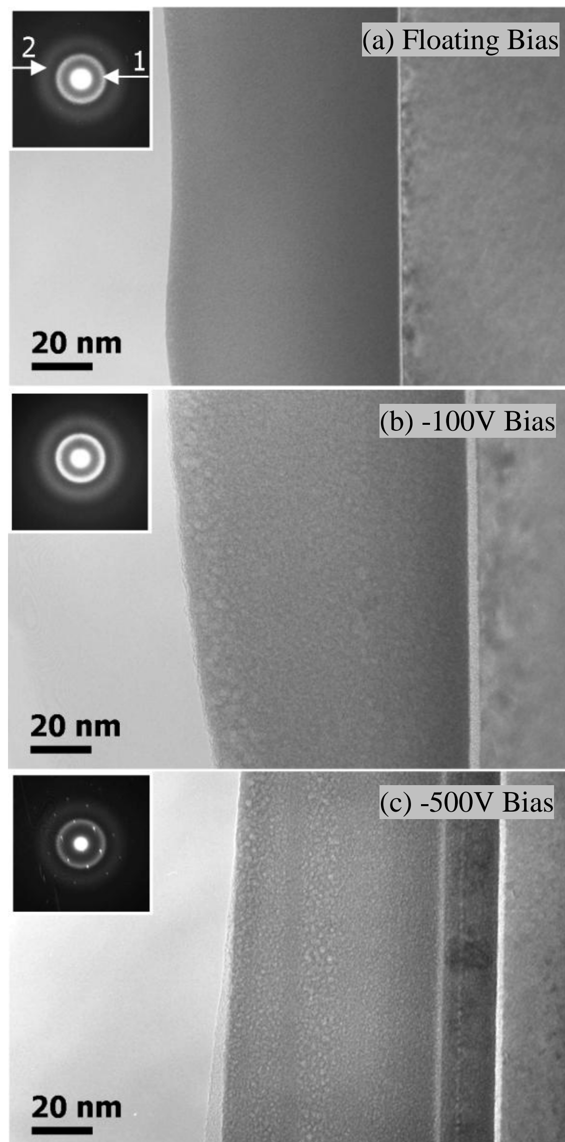

Figure 5-7: Bright field cross-sectional TEM images of the (a) sample deposited at floating potential, (b) −100 V bias sample and the (c) −500 V bias sample. Note that the diffraction pattern in (c) contains diffraction spots from the [011] zone axis of the Si substrate. The two main diffraction rings indicated in (a) occur at d = 2.7 Å and d = 1.6 Å and can be indexed to the (011) and a combination of the (120) and (211) reflections of monoclinic $P2_1/c$ HfO_2.

5.3.4 Electron energy loss spectroscopy (EELS)

EELS was performed on the HfO_2 films using the GIF spectrometer in the TEM with an entrance aperture of 2 mm. The FWHM of the zero loss peak was measured to be approximately 2 eV. The region in the vicinity of the oxygen k-edge was scanned and the background removed.

In 2004, an in depth study by McComb et al [1] was performed on a range of hafnium oxide related crystalline standards using EELS. Of specific interest was the near edge structure comparison between experimentally collected monoclinic HfO_2 and the same structure calculated using the FEFF8 code. A very close match of peak position and relative heights between experiment and calculation was found. In a similar way, the oxygen k-edge of the HfO_2 films deposited in this study at floating and -500 V potentials were compared to a FEFF8 calculation of the monoclinic structure (figure 5-8). Broadening was added to the calculation to account for instrumental and lifetime broadening in the EELS experiment. It can be seen that the main peak in the floating potential sample is less resolved than that in the biased sample, indicating that more disorder is present within the film. The peak positions and relative heights compare well with that found in previous results [1, 36], but the main peaks are not as well resolved. This could either be a result of increased disorder in the films or instrumental broadening.

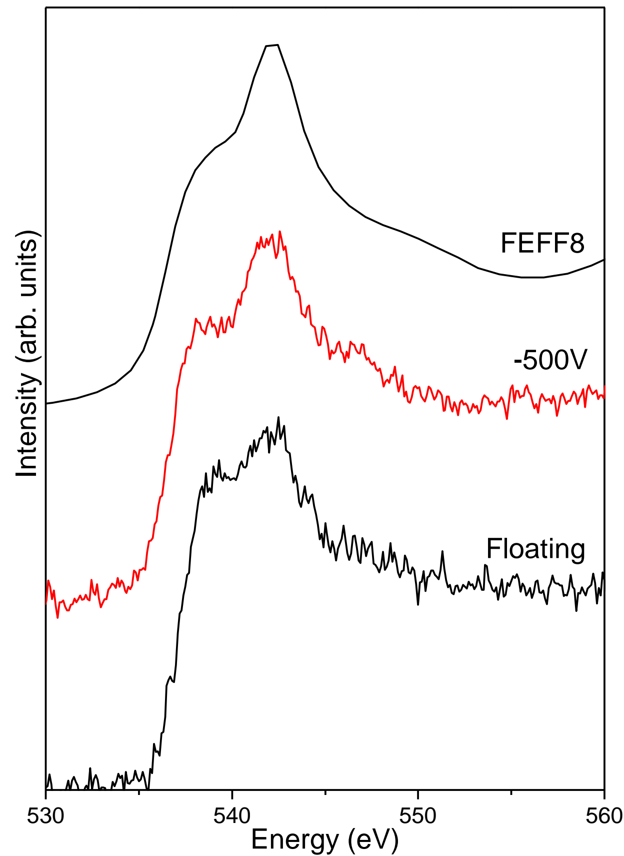

Figure 5-8: EELS spectra of the HfO_2 films deposited at different substrate bias's compared to that of a broadened monoclinic structure as calculated using the FEFF8 *ab initio* code.

5.3.5 Electrical breakdown

The *E(J)* (leakage) characteristics of the films were obtained using a programmable voltage ramping source and PC-interfaced digital multimeter. Silver contacts of approximate area $0.01mm^2$ were placed onto the sample and dual Al ohmics were formed onto the Si substrate prior to deposition.

Figure 5-9 shows the breakdown characteristics of the HfO_2 film deposited with a floating potential on the substrate. Breakdown characteristics on the -100 V and -500 V biased samples were unable to be performed due to short circuits occurring at all of the silver contacts most likely due to the defects in the thin films seen in section 5.3.2. The electrical breakdown for the floating film (defined to be the electric field at which the leakage current density exceeded 1

μAcm^{-2}) occurred at 8×10^5 V/cm, which compares well with the breakdown results given in other reports [37, 38] of between 1×10^5 and 2×10^6 V/cm.

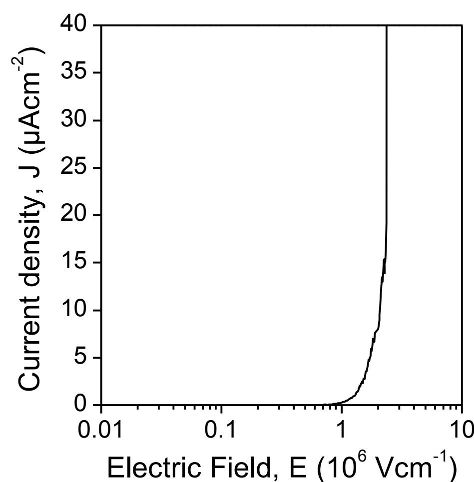

Figure 5-9: E-J characteristics of the HfO_2 film deposited at floating potential. Films deposited with a greater substrate bias sustained film damage and the breakdown characteristics couldn't be determined.

5.4 The effect of substrate temperature on hafnium oxide films synthesised using FCVA

In this section the results for the HfO_2 films synthesised with increasing substrate temperatures during cathodic arc deposition is presented. Floating substrate potential was used since in the last section higher bias was found to be problematic. Temperatures ranging from room temperature (~21 ℃) up to 800 ℃ were applied to the substrate with a floating potential. This substrate potential was selected as it gave the best breakdown results in the previous section.

5.4.1 X-ray photoelectron spectroscopy (XPS)

Figure 5-10 shows XPS spectra in the vicinity of the hafnium 4f peaks for the HfO_x films at the indicated temperatures. Ar ion sputtering was performed before each experiment to remove possible contaminants, as such it is possible that the surface bonds have been damaged and care must be taken interpreting the XPS results. However, the doublet comprised of the 4f7 and 4f5

peaks at 16.9 eV and 18.4 eV respectively, is typical of that previously observed from HfO_2 [31]. The variation in peak position can be attributed to sample charging effects during analysis. These peaks become better resolved with increasing temperature, possibly due to an increase in crystallographic order within the films. The oxygen 1s peak, shown in figure 5-11, was found to be similar for all samples. Table 5-3 shows the atomic percentages of hafnium and oxygen calculated from the XPS spectra. Within experimental error, all of the films are close to stoichiometric HfO_2.

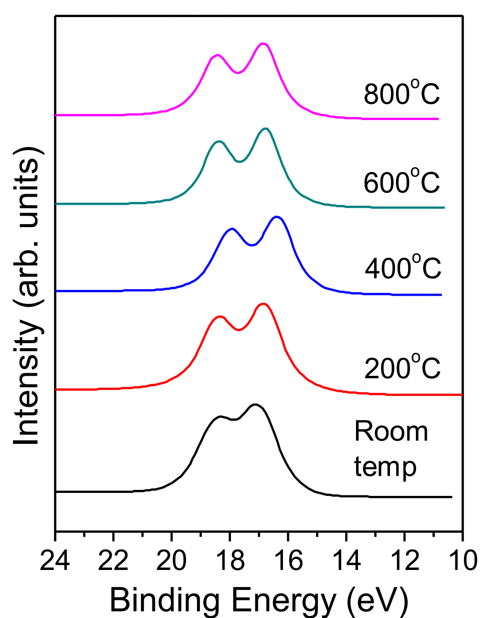

Figure 5-10: XPS spectra of the Hafnium 4f peak for the HfO_x films deposited at the temperatures indicated.

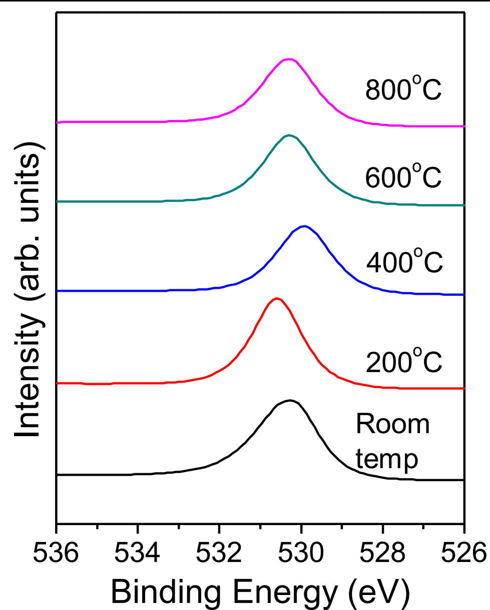

Figure 5-11: XPS spectra in the region of the oxygen 1s binding energy peak of the hafnium oxide films deposited at the temperatures indicated

Table 5-3: Calculated atomic percentages within the HfO_2 films rounded to the nearest percent.

Deposition Temperature	**Thickness (nm)**	**At% (Hf)**	**At% (O)**
Room Temp 1	40	35±1	65±1
Room Temp 2	100	35±1	65±1
100 °C	30	35±1	65±1
200 °C	30	35±1	65±1
300 °C	30	33±1	67±1
400 °C	60	34±1	66±1
500 °C	60	34±1	66±1
600 °C	50	34±1	66±1
700 °C	60	34±1	66±1
800 °C	50	34±1	66±1

5.4.2 X-ray diffraction (XRD)

Figure 5-12 shows the XRD spectra for the indicated HfO_2 films. At room temperature, no discernable peaks were observed, indicating a disordered microstructure. With increasing substrate temperature, distinct peaks appear and become more pronounced. This indicates that there is an increase in crystallinity within the films at higher deposition temperatures. An increase in crystallinity can be explained by increased mobility of the deposited atoms, allowing them to rearrange into lower energy configurations. Most notable is a transition at approximately 400 ºC in which a strong peak appears at approximately 2θ=28.3º. Each peak has been labelled and can be indexed to either the monoclinic or tetragonal phase of HfO_2 using lattice parameters from Zhao et al [14] (see table 5-4). The most prolific peak '1' corresponds to monoclinic $(\bar{1}11)$ HfO_2. The presence of the monoclinic phase is in agreement with that found previously by other authors in HfO_2 films prepared using a variety of deposition methods [7, 20, 37, 39, 40]. Evidence for the tetragonal phase of HfO_2 was also found, particularly in the films prepared at temperatures above 500 ºC. The peaks that can only be attributed to the tetragonal phase (8 and 9) are less intense in the 800 ºC film compared to those exhibited by the 600 °C film. This suggests that although both films contain the tetragonal phase, they have different microstructures caused by differences in crystalline order and/or preferred orientation. In the bulk, the monoclinic to tetragonal phase transition is expected to occur at temperatures of approximately 1700 ºC for low pressures [9]. However, in thin film deposition, phases which are normally thermodynamically unstable can be formed. For example, traces of the tetragonal phase have been observed within low temperature hafnium oxide thin films prepared using atomic layer deposition [41, 42].

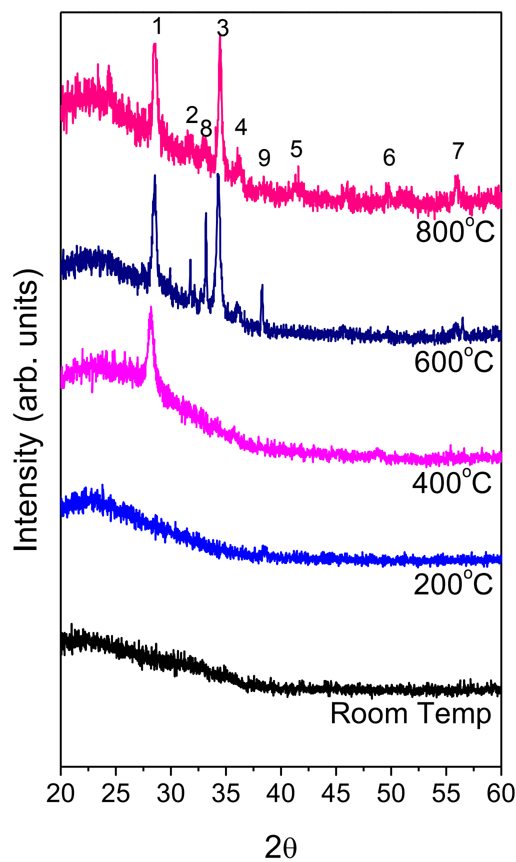

Figure 5-12: XRD patterns of the hafnium oxide films deposited with the indicated deposition temperatures. The labelled peaks have been indexed either to the monoclinic or tetragonal phases of HfO_2 as shown in table 5-4.

Table 5-4: Details of the indexing of the XRD spectra shown in figure 2. All peaks could be indexed either to the monoclinic or tetragonal phases of HfO_2 using previously published lattice parameters [14]. Note that multiple phases are shown for peaks '3' and '6' due to ambiguity in the peak positions between the two phases.

Peak Label	Peak position	Monoclinic	Tetragonal
1	28.4°	$(\bar{1}11)$	
2	31.8	(111)	
3	34.4	(200)	(002)
4	36.2	(002)	
5	41.5	$(\bar{1}21)$	
6	49.9	(220)	(202)
7	56.0	$(\bar{3}11)$	
8	33.0		(200)
9	38.3		(102)

5.4.3 Transmission electron microscopy (TEM)

Figures 5-13 and 5-14 show the X-TEM images and SAED patterns for the hafnium oxide samples prepared at (a) room temperature, (b) 400 ºC and (c) 800 ºC. The images show the film running through the centre (dark region), the silicon substrate on the right and the epoxy glue used for sample preparation on the left side. At room temperature (figure 5-13a) the microstructure appears disordered, in agreement with the XRD results for this sample. A disordered microstructure was confirmed from selected area diffraction patterns taken from this film which exhibit a ring pattern (figure 5-14a). This ring pattern has been indexed to the monoclinic phase of HfO_2.

With an increase in substrate temperature to 400 ºC, large crystals can be seen in the film as indicated by the presence of lattice and Moirè fringes (figure 5-13b). The diffraction pattern (figure 5-14b) confirms an increase in crystallinity showing a spot pattern which has been

indexed to the monoclinic phase. The image and diffraction pattern (figures 5-13c and 5-14c) shows that the film deposited at 800 ºC also contains a high degree of crystal order. The diffraction pattern has been indexed to the monoclinic phase, however many of the spots could not be unambiguously indexed, suggesting the presence of multiple phases present within the film.

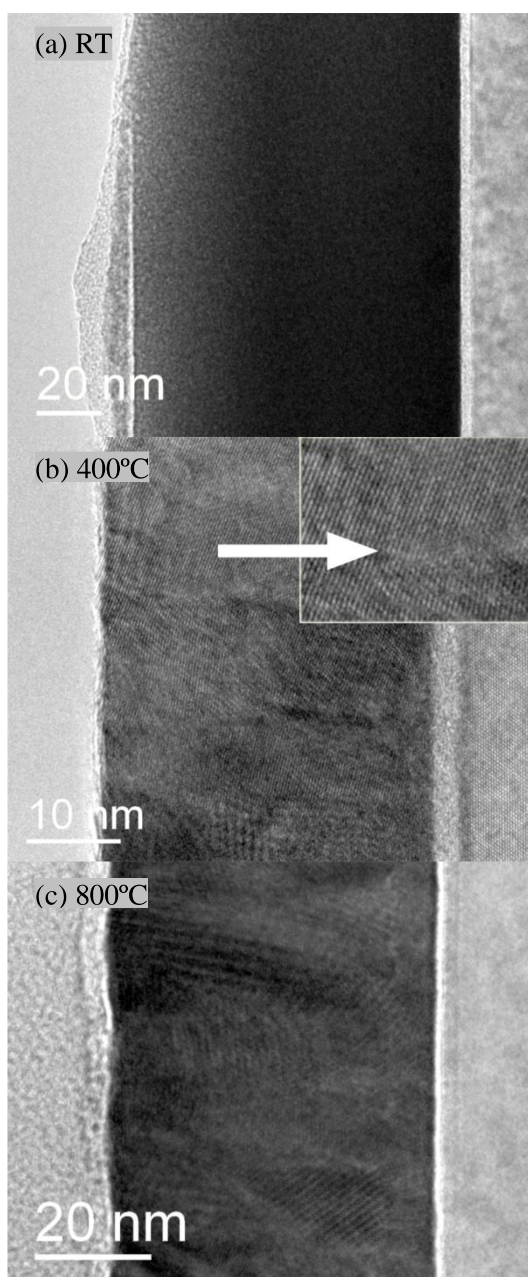

Figure 5-13: X-TEM images of the HfO_2 films prepared with substrate temperatures of (a) room temperature, (b) 400 ºC and (c) 800 ºC. The HfO_2 film is the dark region running down the centre of each image, the silicon substrate is on the right hand side and the epoxy bonding agent is on the left hand side.

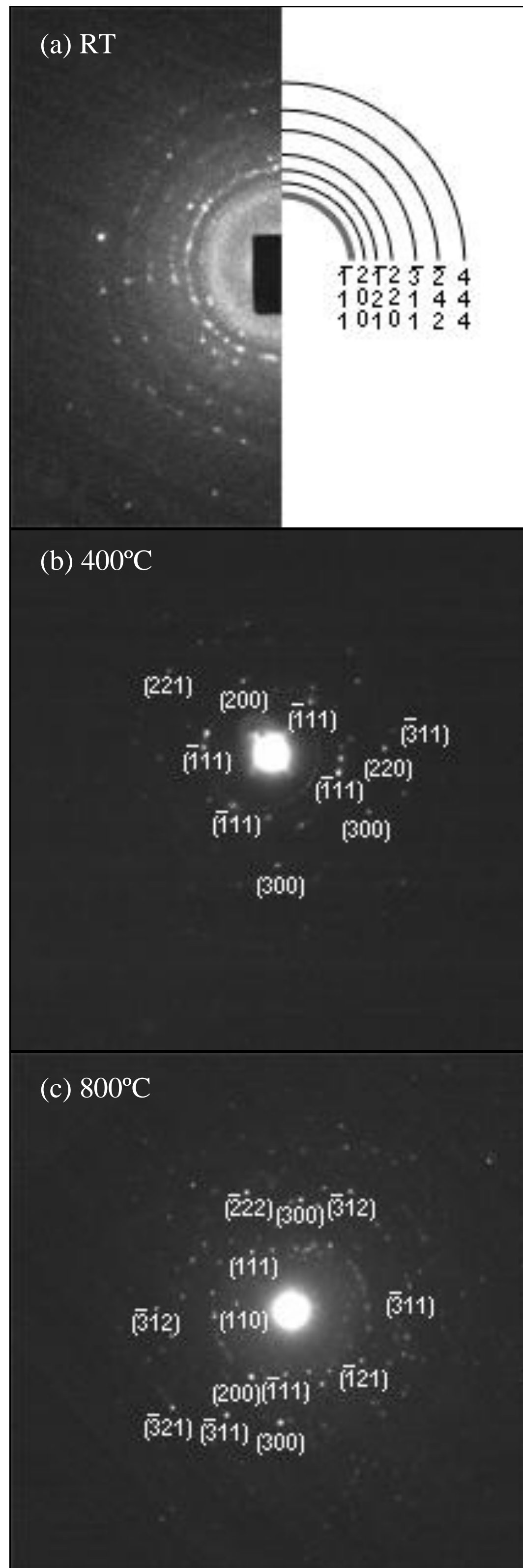

Figure 5-14: SAED patterns of the film areas shown in figure 5-13, deposited with substrate temperatures of (a) room temperature, (b) 400 ºC and (c) 800 ºC. The patterns have been indexed to the monoclinic phase of HfO_2.

5.4.4 X-ray absorption spectroscopy (XAS)

Figure 5-15 shows the XAS oxygen K-edge of the HfO_2 samples with the indicated temperatures compared to the monoclinic powder standard. Each oxygen K-edge for contains a similar near edge structure consisting of three main peaks, typical of d^0 transition metal oxides [43]. The main peaks, located at 533.8 eV, 537.4 eV and 541.5 eV, correspond to transitions to oxygen p components hybridised with hafnium d-e_g, d-t_{2g} and sp mixed components respectively [43, 44]. Each of these peaks is labelled in the room temperature spectra in figure 5-15. As the substrate temperature increases, the near edge structure becomes similar to the monoclinic powder with a splitting of the first and third peaks and the appearance of a forth peak located at approximately 550.2 eV. The splitting of the d-e_g band was predicted using molecular orbital calculations of the monoclinic phase [36]. The absence of the splitting in this peak at low deposition temperatures is attributed to more crystallographic disorder in the films which broadens features in the density of states.

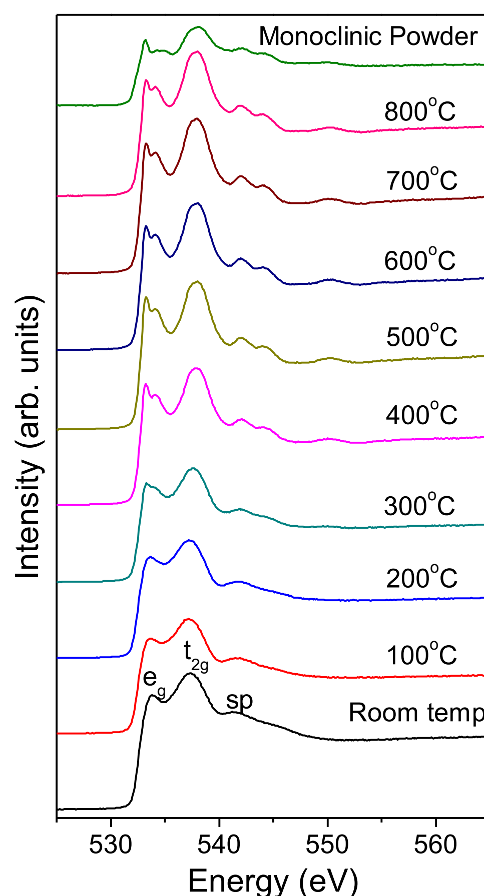

Figure 5-15: XAS in the vicinity of the oxygen K-edge of the HfO_2 films deposited with the indicated temperatures compared to a monoclinic powder standard.

McComb [1] and Mizoguchi [36] both investigated the oxygen K-edge for HfO_2 samples and found that the *ab initio* calculations reproduced the peaks with correct position and relative heights. However the experimentally determined near edge structures were not well resolved, resulting in the doublet peaks which were predicted in the calculations to not be observed. The XAS results presented in this section show a well resolved d-e_g transition peak, so a better comparison is made. Figure 5-16 shows the oxygen K-edge of the three phases of HfO_2 calculated using FEFF9, compared with the film deposited at 800ºC and the monoclinic powder standard. The FEFF9 calculations show that the two phases with the most symmetry (cubic and tetragonal) exhibit shaper features. The monoclinic calculation matches the film the best, in agreement with the XRD and TEM results which both found that the monoclinic phase was present. Given that there was evidence from XRD that the tetragonal phase is also present

within the films deposited at higher temperatures, a linear combination of phases (60% monoclinic, 40% tetragonal) is also plotted in figure 5-16. It can be seen that this combined spectra is a better fit, particularly the d-t_{2g} peak.

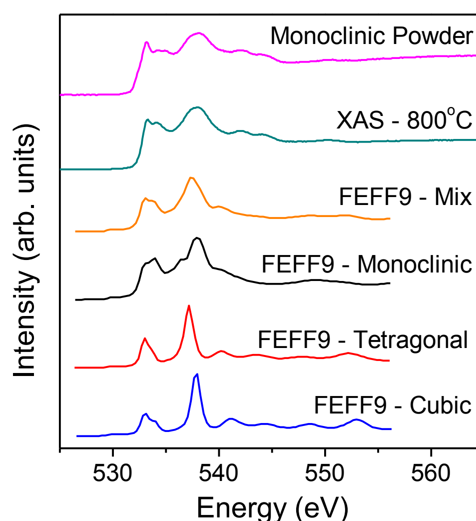

Figure 5-16: Comparison of the oxygen K-edge for the FEFF9 calculations of 3 phases of HfO_2 compared to the 800°C HfO_2 sample and monoclinic powder standard. The spectra 'FEFF9 – Mix' refers to a 3:2 linear combination of the monoclinic phase and the tetragonal phase.

5.4.5 Electrical breakdown

Figure 5-17 shows the electrical breakdown characteristics, E(J) for selected HfO_2 films. Table 5-5 lists the breakdown field for each of the samples. With the notable exception of the film deposited at 800 °C, there is a correlation between growth temperature and the breakdown characteristics of the films. As the substrate temperature increases and the crystallinity improves, the breakdown characteristics tend to degrade. These results support the proposition that disordered films provide the best breakdown characteristics in HfO_2 films [15-18]. The weaker breakdown characteristic exhibited by the film deposited at 600 °C compared to that exhibited by the film deposited at 800 °C can be attributed to the differences in microstructure apparent in the XRD results. The electrical breakdown for the film deposited at room temperature (defined to be the electric field at which the leakage current density exceeded 1

μAcm^{-2}) occurred at 8×10^5 V/cm, which compares well with the breakdown results given in other reports [37, 38] of between 1×10^5 and 2×10^6 V/cm.

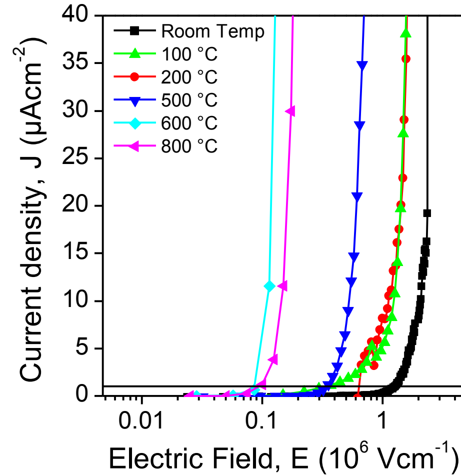

Figure 5-17: E-J characteristics measured from HfO_2 films deposited using a FCVA with the indicated substrate temperatures.

Table 5-5: The microstructures of the films determined using XRD and the electric field at which the leakage current density exceeded 1 μAcm^{-2}.

Deposition Temperature	Thickness (nm)	Microstructure	Breakdown (V/cm)
Room Temp 1	40	Disordered, Monoclinic	8×10^5
Room Temp 2	100	Disordered, Monoclinic	
100 ºC	30	Disordered, Monoclinic	4×10^5
200 ºC	30	Disordered, Monoclinic	6×10^5
300 ºC	30	Disordered, Monoclinic	-
400 ºC	60	Polycrystalline, Monoclinic	-
500 ºC	60	Polycrystalline, Monoclinic	3×10^5
600 ºC	50	Polycrystalline, Monoclinic/Tetragonal	9×10^4
700 ºC	60	Polycrystalline, Monoclinic/Tetragonal	-
800 ºC	50	Polycrystalline, Monoclinic/Tetragonal	1×10^5

5.6 Conclusions

In this chapter, the microstructure and breakdown characteristic of hafnium oxide films prepared using FCVA were investigated as a function of (1) substrate bias and (2) substrate temperature. It was found that with increasing bias on the substrate during deposition that the coatings electrically discharged, causing significant damage to the structure of the films leaving pin holes and large defects. Films deposited at floating potential were found to exhibit good breakdown performance comparable to other work, showing that the FCVA method is capable of producing high quality hafnium oxide films.

With increasing substrate temperature, there is an increase in mobility of the deposited atoms which promotes crystallisation. Diffraction analysis of the films showed that the dominant phase present was monoclinic HfO_2, although there was evidence for the presence of the high temperature tetragonal phase at higher substrate temperatures. It was found that the electrical breakdown of the films was dependent on the substrate temperature and hence crystallinity in the films. Increased crystallinity resulted in a lowering of the electrical breakdown, supporting the proposition that disordered films are preferable for gate dielectric applications.

5.7 Bibliography

1. McComb, D.W., A.J. Craven, D.A. Hamilton, and M. MacKenzie, *Probing local coordination environments in high-k materials for gate stack applications.* Applied Physics Letters, 2004. **84**(22): p. 4523-4525.
2. Wilk, G.D., R.M. Wallace, and J.M. Anthony, *High-κ gate dielectrics: Current status and materials properties considerations.* Journal of Applied Physics, 2001. **89**(10): p. 5243-5275.
3. Chau, R., J. Brask, S. Datta, G. Dewey, M. Doczy, B. Doyle, J. Kavalieros, B. Jin, M. Metz, A. Majumdar, and M. Radosavljevic, *Application of high-κ gate dielectrics and metal gate electrodes to enable silicon and non-silicon logic nanotechnology.* Microelectronic Engineering, 2005. **80**: p. 1-6.
4. Chau, R., S. Datta, M. Doczy, J. Kavalieros, and M. Metz, *Gate Dielectric Scaling for High-Performance CMOS: from SiO_2 to High-κ*, in *Extended Abstracts of International Workshop on Gate Insulator (IWGI)*. November 2003, pp. 124-126: Tokyo, Japan.
5. Foran, B., J. Barnett, P.S. Lysaght, M.P. Agustin, and S. Stemmer, *Characterization of advanced gate stacks for Si CMOS by electron energy-loss spectroscopy in scanning*

transmission electron microscopy. Journal of Electron Spectroscopy and Related Phenomena, 2005. **143**(2-3): p. 149-158.

6. Ohta, H. and H. Hosono, *Transparent oxide optoelectronics.* Materials Today, 2004. **7**(6): p. 42-51.
7. Haines, J., J.M. Leger, S. Hull, J.P. Petitet, A.S. Pereira, C.A. Perottoni, and J.A.H. Da Jornada, *ChemInform Abstract: Characterization of the Cotunnite-Type Phases of Zirconia and Hafnia by Neutron Diffraction and Raman Spectroscopy.* ChemInform, 1997. **28**(42): p. no-no.
8. Cheynet, M.C., S. Pokrant, F.D. Tichelaar, and J.-L. Rouviere, *Crystal structure and band gap determination of HfO[sub 2] thin films.* Journal of Applied Physics, 2007. **101**(5): p. 054101-8.
9. Wang, J., H.P. Li, and R. Stevens, *Hafnia and hafnia-toughened ceramics.* Journal of Materials Science, 1992. **27**(20): p. 5397-5430.
10. He, J.Q., A. Teren, C.L. Jia, P. Ehrhart, K. Urban, R. Waser, and R.H. Wang, *Microstructure and interfaces of HfO2 thin films grown on silicon substrates.* Journal of Crystal Growth, 2004. **262**(1-4): p. 295-303.
11. Niinistö, J., M. Mäntymäki, K. Kukli, L. Costelle, E. Puukilainen, M. Ritala, and M. Leskelä, *Growth and phase stabilization of HfO2 thin films by ALD using novel precursors.* Journal of Crystal Growth, 2010. **312**(2): p. 245-249.
12. Ushakov, S.V., A. Navrotsky, Y. Yang, S. Stemmer, K. Kukli, M. Ritala, M.A. Leskelä, P. Fejes, A. Demkov, C. Wang, B.Y. Nguyen, D. Triyoso, and P. Tobin, *Crystallization in hafnia- and zirconia-based systems.* physica status solidi (b), 2004. **241**(10): p. 2268-2278.
13. Lowther, J.E., J.K. Dewhurst, J.M. Leger, and J. Haines, *Relative stability of ZrO_2 and HfO_2 structural phases.* Physical Review B, 1999. **60**(21): p. 14485.
14. Zhao, X. and D. Vanderbilt, *First-principles study of structural, vibrational, and lattice dielectric properties of hafnium oxide.* Physical Review B, 2002. **65**(23): p. 233106.
15. Forsgren, K., A. Harsta, J. Aarik, A. Aidla, J. Westlinder, and J. Olsson, *Deposition of HfO_2 Thin Films in HfI_4-Based Processes.* Journal of The Electrochemical Society, 2002. **149**(10): p. F139-F144.
16. Rangarajan, V., H. Bhandari, and T.M. Klein, *Comparison of hafnium silicate thin films on silicon (1 0 0) deposited using thermal and plasma enhanced metal organic chemical vapor deposition.* Thin Solid Films, 2002. **419**(1-2): p. 1-4.
17. Moon Sig, J., C. Byung Jin, Y. Chia Ching, D. Siu Hung Chan, W. Sung Jin, S. Mathew, L. Kanta Bera, N. Balasubramanian, and K. Dim-Lee, *Formation of hafnium-aluminum-oxide gate dielectric using single cocktail liquid source in MOCVD process.* Electron Devices, IEEE Transactions on, 2003. **50**(10): p. 2088-2094.
18. Choi, C.H., S.J. Rhee, T.S. Jeon, N. Lu, J.H. Sim, R. Clark, M. Niwa, and D.L. Kwong. *Thermally stable CVD HfO_xN_y advanced gate dielectrics with poly-Si gate electrode*. in *Electron Devices Meeting, 2002. IEDM '02. Digest. International*. 2002.
19. Hergenrother, J.M., G.D. Wilk, T. Nigam, F.P. Klemens, D. Monroe, P.J. Silverman, T.W. Sorsch, B. Busch, M.L. Green, M.R. Baker, T. Boone, M.K. Bude, N.A. Ciampa, E.J. Ferry, A.T. Fiory, S.J. Hillenius, D.C. Jacobson, R.W. Johnson, P. Kalavade, R. Keller, C.A. King, A. Kornblit, H.W. Krautter, J.T.C. Lee, W.M. Mansfield, J.F. Miner, M.D. Morris, S.H. Oh, J.M. Rosamilia, B.J. Sapjeta, K. Short, K. Steiner, D.A. Muller, P.M. Voyles, J.L. Grazul, E. Shero, M.E. Givens, C. Pomarede, M. Mazanec, and C. Werkhoven. *50 nm vertical replacement-gate (VRG) nMOSFETs with ALD HfO_2 and Al_2O_3 gate dielectrics*. in *Electron Devices Meeting, 2001. IEDM Technical Digest. International*. 2001.
20. Ho, M.Y., H. Gong, G.D. Wilk, B.W. Busch, M.L. Green, P.M. Voyles, D.A. Muller, M. Bude, W.H. Lin, A. See, M.E. Loomans, S.K. Lahiri, and P.I. Raisanen, *Morphology and crystallization kinetics in HfO_2 thin films grown by atomic layer deposition.* Journal of Applied Physics, 2003. **93**(3): p. 1477-1481.

21. Nguyen, N.V., V.D. Albert, C.-H. Deane, and M.F. Martin, *Sub-bandgap defect states in polycrystalline hafnium oxide and their suppression by admixture of silicon.* Applied Physics Letters, 2005. **87**(19): p. 192903.
22. Ratzke, M., D. Wolfframm, M. Kappa, S. Kouteva-Arguirova, and J. Reif, *Pulsed laser deposition of HfO_2 and Pr_xO_y high-k films on Si(100).* Applied Surface Science, 2005. **247**(1-4): p. 128-133.
23. Yu. Yu, L., A. Zenkevich, E.P. Gusev, and M. Gribelyuk, *In situ investigation of growth and thermal stability of ultrathin Si layers on the HfO[sub 2]/Si (100) high-kappa dielectric system.* Applied Physics Letters, 2005. **86**(19): p. 191904.
24. Balog, M., *Chemical vapor deposition and characterization of HfO2 films from organo-hafnium compounds.* Thin Solid Films, 1977. **41**(3): p. 247-259.
25. Al-Kuhaili, M.F., *Optical properties of hafnium oxide thin films and their application in energy-efficient windows.* Optical Materials, 2004. **27**(3): p. 383-387.
26. Filipescu, M., N. Scarisoreanu, V. Craciun, B. Mitu, A. Purice, A. Moldovan, V. Ion, O. Toma, and M. Dinescu, *High-k dielectric oxides obtained by PLD as solution for gates dielectric in MOS devices.* Applied Surface Science, 2007. **253**(19): p. 8184-8191.
27. Grüger, H., C. Kunath, E. Kurth, S. Sorge, W. Pufe, and T. Pechstein, *High quality r.f. sputtered metal oxides (Ta_2O_5, HfO_2) and their properties after annealing.* Thin Solid Films, 2004. **447-448**: p. 509-515.
28. Tay, B.K., Z.W. Zhao, and D.H.C. Chua, *Review of metal oxide films deposited by filtered cathodic vacuum arc technique.* Materials Science and Engineering: R: Reports, 2006. **52**(1-3): p. 1-48.
29. Lau, D.W.M., D.G. McCulloch, M.B. Taylor, J.G. Partridge, D.R. McKenzie, N.A. Marks, E.H.T. Teo, and B.K. Tay, *Abrupt Stress Induced Transformation in Amorphous Carbon Films with a Highly Conductive Transition Phase.* Physical Review Letters, 2008. **100**(17): p. 176101.
30. Biluš Abaffy, N., J.G. Partridge, J. du Plessis, and D.G. McCulloch, *Optically absorbing trilayer films fabricated using a Filtered Cathodic Vacuum Arc.* Physica Status Solidi (a), 2008. **205**(6): p. 1439-1442.
31. Smirnova, T., V. Kaichev, L. Yakovkina, V. Kosyakov, S. Beloshapkin, F. Kuznetsov, M. Lebedev, and V. Gritsenko, *Composition and structure of hafnia films on silicon.* Inorganic Materials, 2008. **44**(9): p. 965-970.
32. Tan, S., *Control of Interface Traps in HfO₂ Gate Dielectric on Silicon.* Journal of Electronic Materials, 2010. **39**(11): p. 2435-2440.
33. Hullavarad, S., D. Pugel, E. Jones, R. Vispute, and T. Venkatesan, *Low Leakage Current Transport and High Breakdown Strength of Pulsed Laser Deposited HfO₂/SiC Metal-Insulator-Semiconductor Device Structures.* Journal of Electronic Materials, 2007. **36**(6): p. 648-653.
34. Watts, J.F. and J. Wolstenholme, *An Introduction to Surface Analysis by XPS and AES*. 2003: Wiley.
35. Gan, B.K., M.M.M. Bilek, D.R. McKenzie, Y. Shi, D.A. Tompsett, M.B. Taylor, and D.G. McCulloch, *Stress relief and texture formation in aluminium nitride by plasma immersion ion implantation.* Journal of Physics: Condensed Matter, 2004. **10**: p. 1751.
36. Mizoguchi, T. and et al., *First-principles calculation of oxygen K-electron energy loss near edge structure of HfO_2.* Journal of Physics: Condensed Matter, 2009. **21**(10): p. 104212.
37. Dueñas, S., H. Castán, H. García, A. Gómez, L. Bailón, M. Toledano-Luque, I. Mártil, and G. González-Díaz, *Electrical properties of high-pressure reactive sputtered thin hafnium oxide high-k gate dielectrics.* Semiconductor Science and Technology, 2007(12): p. 1344.
38. Yang, T.S., K.-S. An, E.-J. Lee, W. Cho, H.S. Jang, S.K. Park, Y.K. Lee, T.-M. Chung, C.G. Kim, S. Kim, J.-H. Hwang, C. Lee, N.-S. Lee, and Y. Kim, *Chemical Vapor Deposition of HfO_2 Thin Films Using the Novel Single Precursor Hafnium 3-Methyl-3-pentoxide, $Hf(mp)_4$.* Chemistry of Materials, 2005. **17**(26): p. 6713-6718.

39. Scarel, G., S. Spiga, C. Wiemer, G. Tallarida, S. Ferrari, and M. Fanciulli, *Trends of structural and electrical properties in atomic layer deposited HfO2 films.* Materials Science and Engineering B, 2004. **109**(1-3): p. 11-16.

40. Ni, J., Z.-c. Li, and Z.-j. Zhang, *Influence of deposition temperature on the structure and optical properties of HfO_2 thin films.* Frontiers of Materials Science in China, 2008. **2**(4): p. 381-385.

41. Aarik, J., A. Aidla, A.A. Kiisler, T. Uustare, and V. Sammelselg, *Influence of substrate temperature on atomic layer growth and properties of HfO_2 thin films.* Thin Solid Films, 1999. **340**(1-2): p. 110-116.

42. Nguyen, N.V., A.V. Davydov, D. Chandler-Horowitz, and M.M. Frank, *Sub-bandgap defect states in polycrystalline hafnium oxide and their suppression by admixture of silicon.* Applied Physics Letters, 2005. **87**(19): p. 192903-3.

43. Chen, J.G., *NEXAFS investigations of transition metal oxides, nitrides, carbides, sulfides and other interstitial compounds.* Surface Science Reports, 1997. **30**(1-3): p. 1-152.

44. Soriano, L., M. Abbate, J.C. Fuggle, M.A. Jiménez, J.M. Sanz, C. Mythen, and H.A. Padmore, *The O 1s x-ray absorption spectra of transition-metal oxides: The TiO_2-ZrO_2-HfO_2 and V_2O_5-Nb_2O_5-Ta_2O_5 series.* Solid State Communications, 1993. **87**(8): p. 699-703.

Chapter 6

Conclusions and future work

Metal oxide thin films play an important role in many industries and have been extensively studied for decades. From the discovery of tungsten bronzes to the use of hafnium silicates in microprocessors in modern computing, these materials are not only of major interest to the scientific community but also in industry for the betterment of modern living. However, with a vast array of materials and means of thin film coating deposition available, the growth mechanics of a particular deposition method and the effect on the properties of the films is not well understood. It may be expected that thin film coatings with similar properties will be attained independent of deposition method. However, seemingly small differences often play a role in changing the microstructure which result in surprisingly large variations in the physical properties of the films.

This thesis investigates the microstructure and physical properties of several important metal oxide coatings. Several deposition techniques were employed and the effect of changing the deposition conditions investigated.

In chapter 3, tungsten oxide (WO_3) films were synthesised using both pulsed cathodic arc and pulsed magnetron sputtering deposition techniques. The effect of deposition method on the microstructure of the films was investigated using electron microscopy and spectroscopic techniques. *Ab initio* calculations were performed to study the change in the near edge structure

for different microstructures and this was used to fingerprint the phases of the deposited films. From these results, the major findings were:

1. **Dependence on deposition method of the microstructure of WO_3 films.** It was found that the energetic deposition from the pulsed arc resulted in a highly ordered tetragonal microstructure. In contrast to this with magnetron sputtering, deposition by low energy neutrals, a highly disordered film was deposited. These results demonstrate how different deposition techniques can lead to films with completely different microstructures.

2. **Using *ab initio* calculations to fingerprint the microstructure of WO_3 films.** It was shown using the *ab initio* codes that the near edge structure of known phases of WO_3 could be calculated. This calculated near edge structure can be used as a fingerprint to match with experimental results to help identify the phase present.

In chapter 4 the physical properties and microstructure of aluminium zinc oxide films (AZO) films were investigated. AZO films were deposited using pulsed cathodic arc, pulsed magnetron sputtering, high power impulse magnetron sputtering (HIPIMS) and a novel variant of HIPIMS which incorporated a straight magnetic filter. The major findings for this chapter are presented below:

1. **Relationship between microstructure and the physical properties of AZO films.** It was found that depending on microstructure of the deposited AZO films, different optical and electrical properties could be observed. Each of the coatings appeared as wurtite ZnO with different amounts of crystallographic order depending on the deposition method. It was found that much of the aluminium appeared within the AZO films not as substitutional Al in Zn sites, but instead in the form of octahedrally arranged β-Al_2O_3. Coatings with a disordered microstructure exhibited inferior electrical properties as opposed to those which contained wurtzite ZnO grains oriented with their c-axis perpendicular to the substrate which performed best.

2. **Negative ion damage and its effect on the structure and properties of AZO films.** It was shown that the presence of O- ions during reactive deposition of AZO coatings in magnetron sputtering related techniques had a negative influence on film properties. Depending on the position on the substrate in relation to the magnetron field lines, different amounts of ion damage was observed. This ion damage effect was exacerbated in the HIPIMS technique which uses much higher power, thus accelerating the damaging ions with a greater energy. As a result of this ion damage, the electrical and optical properties of the films were compromised. It was shown that using a magnetic filter during deposition acts to protect the AZO films from the negative ion impacts and also enhances deposition rates.

Filtered cathodic vacuum arc (FCVA) was shown to be a good method for depositing dense, flat hafnium oxide (HfO_2) films. In chapter 5 the effect of increased deposition temperature and substrate bias on the microstructure and electrical breakdown of FCVA deposited HfO_2 films was investigated. The major findings for this chapter are presented below:

1. **The relationship between crystallinity and electrical breakdown of HfO_2 films.** The temperature dependence on the crystallinity was explored and it was found that phases which are usually thermodynamically unstable can be achieved with thin film coatings. It was shown that the amount of crystallinity of the HfO_2 films has a direct effect on the electrical breakdown, whereby disordered films deposited at room temperature were found to have the best breakdown characteristics compared to the crystallised films deposited at higher temperatures.

From the work completed and the findings in this thesis, there is still much in this field to be explored. Some suggestions for future research include:

1. Perform transmission electron microscopy on the AZO films prepared by magnetron sputtering, HIPIMS and filtered HIPIMS.
2. Further work on the effect of negative ion damage on the structure of the films. It will be possible to apply this knowledge to other materials which will be useful to other research groups and industry to make thin film coatings with superior performance.
3. Perform *C(V)* measurements on HfO_2 films deposited by cathodic arc to analyse how the differences in crystallinity affect the dielectric constant for this films.
4. Deposit HfO_2 films of thickness in the order of 10-20 nm using a filtered cathodic arc to determine the effect on crystallinity and electrical properties of miniaturisation of the films. The work in the AZO chapter revealed that it is possible to grow films where the crystal grains take up the entirety of the thickness of the films. If this were applied to HfO_2 films, it might be possible to grow films where the relative size of the crystals to the film thickness is large, thereby reducing the grain boundaries and possible leakage paths.